



저작자표시-비영리 2.0 대한민국

이용자는 아래의 조건을 따르는 경우에 한하여 자유롭게

- 이 저작물을 복제, 배포, 전송, 전시, 공연 및 방송할 수 있습니다.
- 이차적 저작물을 작성할 수 있습니다.

다음과 같은 조건을 따라야 합니다:



저작자표시. 귀하는 원저작자를 표시하여야 합니다.



비영리. 귀하는 이 저작물을 영리 목적으로 이용할 수 없습니다.

- 귀하는, 이 저작물의 재이용이나 배포의 경우, 이 저작물에 적용된 이용허락조건을 명확하게 나타내어야 합니다.
- 저작권자로부터 별도의 허가를 받으면 이러한 조건들은 적용되지 않습니다.

저작권법에 따른 이용자의 권리는 위의 내용에 의하여 영향을 받지 않습니다.

이것은 [이용허락규약\(Legal Code\)](#)을 이해하기 쉽게 요약한 것입니다.

[Disclaimer](#)

공학박사학위논문

풍력터빈에서 발생하는 광대역 소음의
생성과 전파 및 저감에 대한 연구

Generation, Propagation, and Reduction of Aerodynamic
Broadband Noise from Wind Turbines

2014 년 8 월

서울대학교 대학원

기계항공공학부

이 승 훈

풍력터빈에서 발생하는 광대역 소음의 생성과 전파 및 저감에 대한 연구

Generation, Propagation, and Reduction of
Aerodynamic Broadband Noise from Wind Turbines

지도교수 이 수 갑

이 논문을 공학박사 학위논문으로 제출함

2014 년 8 월

서울대학교 대학원

기계항공공학부

이 승 훈

이승훈의 공학박사 학위논문을 인준함

2014 년 8 월

위원장 : 申 尙 竣 

부위원장 : 李 樹 甲 

위원 : 金 奎 弘 

위원 : 崔 祐 榮 

위원 : 홍 지 영 

Generation, Propagation, and Reduction of Aerodynamic Broadband Noise from Wind Turbines

Seunghoon Lee

Department of Mechanical and Aerospace Engineering

Seoul National University

Abstract

Aerodynamic broadband noise generated from horizontal axis wind turbines is investigated in this research. First, a numerical method to predict wind turbine aerodynamic noise is proposed by using an analytic trailing edge noise model and a wall-pressure spectral model for flow with adverse pressure gradient. Reynolds-averaged Navier-Stokes simulation and XFOIL code are used to obtain the wall-point pressure spectra at blade sections. This method is fast and reliable numerical model which is applicable for use in industrial applications. For the validation of the numerical method, noise measurement is also carried out for a 10kW wind turbine, and a comparison is made between the predicted results and the measured data. Using the proposed method, the aerodynamic noise from a 3MW wind turbine is predicted at various inflow wind speeds and distances. Moreover, time domain simulation for the wind turbine aerodynamic noise is performed to examine the main cause of the amplitude modulation of wind turbine noise, as well as to compare the acoustical characteristics depending on the

observer locations. Analytic trailing edge noise and turbulence ingestion noise models are used to determine the unsteady pressure on the blade surface. The far-field acoustic pressure due to the unsteady pressure is calculated using the acoustic analogy theory. By using a strip theory approach, the two-dimensional noise model is applied to rotating wind turbine blades. The numerical results indicate that, although the operating and atmospheric conditions are identical, the acoustical characteristics of wind turbine noise can be quite different with respect to the distance and direction from the wind turbine. Using these prediction results, it is investigated why the amplitude modulation of wind turbine noise is heard even at long distances from a wind turbine. Furthermore, to reduce trailing edge noise from a 10kW wind turbine, the airfoil shape and the planform of the wind turbine blade are modified using optimization techniques based on genetic algorithms. The optimized airfoil is first determined based on a section of the rotor blade, and then the optimized blade is designed with this airfoil. A wind tunnel experiment is also performed to validate the design optimization. In addition, wind turbine blades with serrated trailing edge are also examined for the noise reduction. To examine the effect of serrated trailing edge on the trailing edge noise reduction, a field experiment is carried out based on a 10kW wind turbine.

Keywords: Wind turbine noise, Noise reduction, Trailing edge noise, Turbulence ingestion noise, Design optimization, Noise measurement

Student ID: 2009-30903

Contents

Abstract	i
List of Figures	vii
List of Tables	xii
List of Audio Clips	xiii
Nomenclature	xiv
1 Introduction	1
1.1 Wind turbine aerodynamic noise	1
1.2 Current issues	4
1.3 Research objective	7
2 A prediction model for wind turbine noise	9
2.1 Overview of wind turbine prediction models	9
2.2 Numerical method	12
2.2.1 Trailing edge noise model	12
2.2.2 Turbulence ingestion noise model	16
2.2.3 Trailing edge bluntness noise model	17
2.2.4 Wall-pressure spectral model	18
2.3 Model validation	19

2.3.1	Wall-point pressure spectrum with RANS simulation and XFOIL	19
2.3.2	Trailing edge noise	30
2.3.3	Wind turbine aerodynamic noise	33
2.3.3.1	Noise measurement	33
2.3.3.2	Results	36
2.4	Results	39
2.4.1	Wind turbine model	39
2.4.2	Aerodynamic analysis	41
2.4.3	Noise prediction	43
2.5	Discussion	48
3	Time domain simulation of wind turbine noise	50
3.1	Introduction	50
3.1.1	Amplitude modulation of wind turbine noise	50
3.1.2	Literature review	53
3.1.3	Research objective	55
3.2	Numerical method	57
3.2.1	Trailing edge noise model	57
3.2.2	Turbulence ingestion noise model	59
3.2.3	Acoustic formulation	61
3.2.4	Validation	63
3.2.4.1	Trailing edge noise	63
3.2.4.2	Turbulence ingestion noise	66
3.2.5	Calculation case	69

3.2.5.1	Rotor noise prediction	69
3.2.5.2	Calculation cases	71
3.3	Results	73
3.3.1	Case I—Uniform inflow	73
3.3.1.1	IEC 61400-11 reference position	73
3.3.1.2	Noise characteristics with respect to distance and direction	75
3.3.1.3	Noise source distribution	78
3.3.1.4	Noise index for the amplitude modulation of wind turbine noise	81
3.3.2	Case II—Stationary in motion	84
3.3.3	Case III—Vertical wind shear	86
3.3.4	Case IV—Turbulence ingestion	90
3.4	Discussion	95
4	Wind turbine noise reduction techniques	100
4.1	Introduction	100
4.2	Design optimization of airfoil and blade planform	102
4.2.1	Airfoil design optimization	102
4.2.1.1	Airfoil optimization procedure	102
4.2.1.2	Airfoil optimization result	106
4.2.2	Blade design optimization	109
4.2.2.1	Blade optimization procedure	109
4.2.2.2	Blade optimization result	111
4.2.3	Experimental results and discussion	113
4.3	Serrated trailing edge blade	117

4.3.1	Experimental setup	117
4.3.2	Results and discussion	121
5	Conclusions	127
	References	129
	국문 초록	138

List of Figure

Fig. 1.1 Schematic of the noise mechanism of (a) turbulence ingestion noise, (b) turbulent-boundary-layer trailing edge noise (c) trailing edge bluntness noise	2
Fig. 1.2. Accuracy or reliability vs. computational cost for the prediction model of wind turbine aerodynamic noise	4
Fig. 2.1. Schematic of the trailing edge noise model problem	13
Fig. 2.2. Computational mesh: (a) entire domain (b) zoom on airfoil vicinity	20
Fig. 2.3. Comparison of chordwise pressure distribution between the results of the two simulations and experiments	21
Fig. 2.4. Comparison of skin friction coefficient between the results of the two simulations and an experiment	21
Fig. 2.5. The RANS simulation results for (a) pressure, (b) tangential velocity, and (c) shear stress along the upper side of NACA0012 airfoil	23
Fig. 2.6. Comparison of boundary layer thickness, displacement thickness, and momentum thickness between the results of the two simulations and experiments	24
Fig. 2.7. Chordwise distributions of the inner and outer boundary layer variables obtained from RANS simulation and XFOIL: (a) boundary layer edge velocity, (b) pressure at the wall, (c) skin friction coefficient, (d) boundary layer thickness, (e) boundary layer displacement thickness, (f) boundary layer momentum thickness, (g) wall shear stress, (h) maximum shear stress, (i) ratio of timescales of pressure, (j) Reynolds number based on U_e and θ , (k) Clauser's parameter, (l) wake strength parameter	26
Fig. 2.8. Comparison of velocity profile at $x/C=0.991$ in the boundary layer between RANS simulation and XFOIL	27
Fig. 2.9. Comparison of wall-point pressure frequency spectrum between the results of the two simulations and experiments by Brooks and Hodgson	28
Fig. 2.10. Measured and predicted far-field acoustic spectra of trailing edge noise	30
Fig. 2.11. Measured and predicted 1/3 octave band spectra of trailing edge noise for inflow velocities of (a) 71.3m/s and (b) 39.6m/s	32
Fig. 2.12. Photograph of a 10kW small wind turbine model	34
Fig. 2.13. Noise measurement with a handheld sound pressure level meter and a microphone	35
Fig. 2.14. Schematics of wind turbine measurement and post-processing procedure	35
Fig. 2.15. (a) Measured power and (b) rotational speed with respect to wind speed	36

Fig. 2.16. 1/3 octave band spectra of the measured data and the numerical predictions at wind speeds of (a) 4m/s, (b) 5m/s, (c) 6m/s, and (d) 7m/s	38
Fig. 2.17. Blade planform for a 3MW wind turbine model	40
Fig. 2.18. Operating schedule of 3MW wind turbine: pitch angle and rotational speed	40
Fig. 2.19. Calculated aerodynamic shaft power with respect to wind speed	41
Fig. 2.20. Calculated sectional relative inflow velocity at three wind speeds	42
Fig. 2.21. Calculated sectional effective angle of attack at three wind speeds	42
Fig. 2.22. Predicted sectional power spectral density with RANS simulation	44
Fig. 2.23. (a) Predicted 1/3 octave band spectrum and (b) A-weighted 1/3 octave band spectrum of trailing edge noise and turbulence ingestion noise with RANS simulation	44
Fig. 2.24. Comparison of 1/3 octave band spectrum between RANS simulation and XFOIL45	45
Fig. 2.25. (a) Overall sound pressure level (b) A-weighted sound pressure level of wind turbine noise with respect to wind speed	45
Fig. 2.26. (a) Overall sound pressure level (b) A-weighted sound pressure level with respect to distance from the wind turbine in the downwind direction at a wind speed of 14m/s.	47
Fig. 3.1. The amplitude modulation of wind turbine noise observed by van den Berg	51
Fig. 3.2. Possible cause of the amplitude modulation of wind turbine noise at long distances	54
Fig. 3.3. Schematic of the turbulence ingestion noise model problem	59
Fig. 3.4. Predicted time domain signal of trailing edge noise	64
Fig. 3.5. Comparison of 1/3 octave band spectrum between experimental data and numerical prediction in the frequency and time domain	64
Fig. 3.6. Streamwise trailing edge noise directivity in the mid-span plane for frequencies of (a) $f = 100\text{Hz}$, (b) $f = 500\text{Hz}$, (c) $f = 1000\text{Hz}$, and (d) $f = 5000\text{Hz}$	65
Fig. 3.7. Comparison of 1/3 octave band spectrum between experimental data and numerical prediction in the frequency and time domain	67
Fig. 3.8. Streamwise turbulence ingestion noise directivity in the mid-span plane for frequencies of (a) $f = 100\text{Hz}$, (b) $f = 500\text{Hz}$, (c) $f = 1000\text{Hz}$, and (d) $f = 5000\text{Hz}$	68
Fig. 3.9. Rectangular surface grids for modeling of the wind turbine blade	69
Fig. 3.10. Atmospheric-absorption attenuation coefficients when air temperature, relative humidity, and air pressure are 15°C , 60%, and one standard atmosphere, respectively	70
Fig. 3.11. Predicted acoustic pressure at the IEC 61400-11 reference position	74
Fig. 3.12. Comparison of 1/3 octave band spectra between original Amiet's model and time domain simulation. Upper and lower bars represent the maximum and the minimum sound pressure levels of L_{FAST} in each frequency spectrum. It should be noted that the maximum	

and minimum sound pressure levels in each frequency spectrum do not occur at the same time. 74

Fig. 3.13. (a) The sound pressure level and (b) the modulation depth of the predicted acoustic signals. The azimuth angle, Ψ is defined as the angle between the rotor axis and the line connecting the wind turbine to the observer. The wind is blowing from the $\Psi = 180^\circ$ direction. The modulation depth is defined as the difference between L_{AFmax} and L_{AFmin} 76

Fig. 3.14. 1/3 octave band frequency spectra of the sound pressure level and the modulation depth predicted at distances of (a) $R = 135.8m$ and (b) $R = 1000m$ 78

Fig. 3.15. Level difference between the calculated source distribution and the average sound pressure level of the rotor disk. The source distributions are calculated at three distances in five directions. For each source distribution, the average level of the total segment for the overall time is subtracted from the sound pressure level distribution on the rotor disk. This makes it possible to compare source distributions whose overall sound levels are different. 80

Fig. 3.16. Correlation between four noise metrics and noise annoyance using linear regression analysis: (a) L_{Aeq} , (b) loudness, (c) fluctuation strength, and (d) L_{AFmax} 82

Fig. 3.17. Comparison of the L_{Aeq} , L_{AFmax} , and modulation depth in terms of the distance and direction from the wind turbine 83

Fig. 3.18. Comparison of (a) The sound pressure level and (b) the modulation depth of the predicted acoustic signals between Case I and Case II. 85

Fig. 3.19. (a) Wind speed with respect to height from the ground and (b) the variation of sectional effective angle of attack at $r/R = 0.90$ 87

Fig. 3.20. The comparison of the maximum A-weighted sound pressure level in three inflow wind conditions at two distances from the wind turbine. 87

Fig. 3.21. Calculated source distributions on the rotor disk at $R = 1000m$: (a) Unstable, $\Psi = -60^\circ$; (b) Unstable, $\Psi = 0^\circ$; (c) Unstable, $\Psi = 60^\circ$; (d) Stable, $\Psi = -60^\circ$; (e) Stable, $\Psi = 0^\circ$; (f) Stable, $\Psi = 60^\circ$ 88

Fig. 3.22. Comparison of 1/3 octave band frequency spectra between frequency domain modeling and time domain modeling 90

Fig. 3.23. The A-weighted sound pressure level of the trailing edge noise and turbulence ingestion noise at two distances from the wind turbine 91

Fig. 3.24. The modulation depth of the trailing edge noise and turbulence ingestion noise at two distances from the wind turbine 92

Fig. 3.25. The maximum A-weighted sound pressure level of the trailing edge noise and turbulence ingestion noise at two distances from the wind turbine 92

Fig. 3.26. Calculated source distributions on the rotor disk at $R = 1000m$: (a) Trailing edge noise, $\Psi = -60^\circ$; (b) Trailing edge noise, $\Psi = 0^\circ$; (c) Trailing edge noise, $\Psi = 60^\circ$; (d)

Turbulence ingestion noise, $\Psi = -60^\circ$; (e) Turbulence ingestion noise, $\Psi = 0^\circ$; (f)	
Turbulence ingestion noise, $\Psi = 60^\circ$	94
Fig. 3.27. Angles from (a) the x_1 -axis and (b) x_2 -axis of the outermost segment of the blade to an observer at $R = 90\text{m}$ with respect to the rotor azimuth; (c) $1/(1 - M_r)$ of the outermost segment of the blade to an observer at $R = 90\text{m}$ with respect to the rotor azimuth: $\Psi = 0^\circ$ (—), $\Psi = 30^\circ$ (— — —), $\Psi = 60^\circ$ (— — —), and $\Psi = 90^\circ$ (— — —)	97
Fig. 3.28. Angles from (a) the x_1 -axis and (b) x_2 -axis of the outermost segment of the blade to an observer at $R = 1000\text{m}$ with respect to rotor azimuth; (c) $1/(1 - M_r)$ of the outermost segment of the blade to an observer at $R = 1000\text{m}$ with respect to the rotor azimuth: $\Psi = 0^\circ$ (—), $\Psi = 30^\circ$ (— — —), $\Psi = 60^\circ$ (— — —), and $\Psi = 90^\circ$ (— — —)	97
Fig. 4.1. Airfoil shape modification functions	102
Fig. 4.2. Geometries of the baseline and the optimized airfoils	107
Fig. 4.3. Overall sound pressure levels of the airfoil self-noise for the baseline and optimized airfoil. The airfoil self-noise is the sum of trailing edge noise and trailing edge bluntness noise.	108
Fig. 4.4. Chord and twist distributions for the baseline and optimized blades	112
Fig. 4.5. Predicted overall sound pressure levels for the baseline and optimized wind turbines. The airfoil self-noise is the sum of the trailing edge noise and the trailing edge bluntness noise	112
Fig. 4.6. Configuration for the wind turbine rotor test stand in the anechoic wind tunnel ..	114
Fig. 4.7. Comparison of power coefficients between the experimental data and prediction results	114
Fig. 4.8. Measured overall sound pressure levels for the baseline and optimized wind turbines	115
Fig. 4.9. Measured 1/3 octave band spectra for the baseline and optimized wind turbines ..	115
Fig. 4.10. Geometry of serrated trailing edge	117
Fig. 4.11. Serrated trailing edge design: (a) $\lambda/h = 0.5$ and (b) $\lambda/h = 1.0$	119
Fig. 4.12. Photographs of serrated trailing edges (a) $\lambda/h = 0.5$, (b) $\lambda/h = 1.0$, and (c) rectangular plate	119
Fig. 4.13. Photograph of (a) attachment of serrated trailing edge and (b) serrated trailing edge blade	120
Fig. 4.14. Measured power for the baseline blade (black), the serrated blade of $\lambda/h = 0.5$ (blue), the serrated blade of $\lambda/h = 1.0$ (red), and the rectangular trailing edge blade (green)	122

Fig. 4.15. Measured A-weighted sound pressure level for the baseline blade (black), the serrated blade of $\lambda/h=0.5$ (blue), the serrated blade of $\lambda/h=1.0$ (red), and the rectangular trailing edge blade (green) 122

Fig. 4.16. 1/3 octave band spectra with respect to wind turbine rotational speed: the baseline blade (black), the serrated blades of $\lambda/h=0.5$ (blue), $\lambda/h=1.0$ (red), and the rectangular trailing edge blade (green) 123

Fig. 4.17. (a) A-weighted sound pressure level of high-pass filtered sound and (b) zoom on overlap region: the baseline blade (black), the serrated blades of $\lambda/h=0.5$ (blue), $\lambda/h=1.0$ (red), and the rectangular trailing edge blade (green) 125

List of Tables

Table 2.1. Specification of the wind turbine model	39
Table 3.1. Four calculation cases for the time domain simulation	72
Table 4.1. Normalized boundary layer displacement thickness, the ratio between the trailing edge height and boundary layer displacement thickness, peak frequency, and the minimum trailing edge height at wind speeds from 4m/s to 7m/s.	124

List of Audio Clips

- Aud. 3.1.** This audio is an acoustic signal, which is predicted at the reference positions according to IEC 61400-11. The calculations are performed for a duration of one rotation. This is a file of type “wav”. 73
- Aud. 3.2.** This audio is the sum of 13 acoustic signals, which are predicted at a distance of $R = 135.8\text{m}$ with an azimuth angle ranging from $\Psi = 0^\circ$ to $\Psi = 180^\circ$ at intervals of 15° . Each signal repeats three times, and there is an interval of one second between different signals. This is a file of type “wav”. 77
- Aud. 3.3.** This audio is the sum of 13 acoustic signals, which are predicted at a distance of $R = 1000\text{m}$ with an azimuth angle ranging from $\Psi = 0^\circ$ to $\Psi = 180^\circ$ at intervals of 15° . Each signal repeats three times, and there is an interval of one second between different signals. This is a file of type “wav”. 77
- Aud. 3.4.** This audio is the sum of 6 acoustic signals, which are predicted at a distance of $R = 1000\text{m}$. The signals are presented as the following order: unstable, $\Psi = -60^\circ$; stable, $\Psi = -60^\circ$; unstable, $\Psi = 0^\circ$; stable, $\Psi = 0^\circ$; unstable, $\Psi = 60^\circ$; stable, $\Psi = 60^\circ$. Each signal repeats three times, and there is an interval of one second between different signals. This is a file of type “wav”. 89

Nomenclature

Latin letters

C	chord length
C_f	skin friction coefficient
c_0	ambient speed of sound
d	span
D	drag
\bar{D}	directivity function
f	sound frequency
\mathbf{g}	geometry function
h	height from the ground
h_s	serration height
h_e	trailing edge bluntness height
H	hub height
\hat{k}	normalized wavenumber
k	acoustic wavenumber
k_c	streamwise convective wavenumber
K_{lc}	low-frequency correction factor
L	lift
l_2	spanwise correlation length

l_T	atmospheric turbulence length scale
M	Mach number
\mathbf{n}	unit normal vector from surfaces
N	number of frequency
\mathbf{p}	surface pressure vector
P	power
p'	acoustic pressure
p_0	amplitude of pressure wavenumber component due to turbulent boundary layer
p_{ij}	local gage surface pressure
r	radiation distance
$\hat{\mathbf{r}}$	unit radiation vector
R	distance from a wind turbine to an observer
R_r	rotor radius
R_T	ratio of the outer layer to inner layer timescale
R_θ	Reynolds number based on U_e and θ
Re	Reynolds number
r/R	non-dimensional radial distance from a hub
S_0	normalized wall point pressure spectrum
SPL	sound pressure level
S_{pp}	far-field sound pressure level

S_{qq}	wall point pressure frequency spectrum
St	Strouhal number
S_{ww}	power spectral density of pressure wavenumber component
t	time
T	period
t_{\max}	Maximum airfoil thickness
T_{ij}	Lighthill stress tensor
U	inflow velocity
U_c	convective velocity
U_e	boundary layer edge velocity
v_n	normal velocity
\bar{w}	turbulence intensity
\tilde{w}	amplitude of pressure wavenumber component due to turbulence ingestion
\mathbf{x}	observer location
\mathbf{X}	shape function coefficients
\mathbf{y}	source location
y^+	dimensionless wall distance
\mathbf{Y}	shape functions
z	ground roughness

Greek letters

α	wind shear coefficient
β	$\sqrt{1 - M^2}$
β_c	Clauser's parameter
δ^*	boundary layer displacement thickness
δ_{99}	boundary layer thickness
Δ	Zagarola and Smits's parameter
Δf	frequency bandwidth
Δp_a	pressure jump due to atmospheric turbulence
Δp_i	incident pressure jump
Δp_s	scattered pressure jump
Δp_t	total pressure jump
ΔT	time step
ε	exponential convergence factor parameter
ζ	$\sqrt{\mu^2 - k_2^2 / \beta^2}$
θ	boundary layer momentum thickness
λ	acoustic wavelength
λ_s	serration wavelength
λ/h	ratio of the width to the amplitude of serration
μ	$M\omega / \beta^2 U$

ν	solid angle between beveled surfaces near trailing edge
ξ	rotor azimuth angle
Π	wake strength parameter
ρ_0	ambient density
σ	solidity
σ'	$\sqrt{x_1^2 + \beta^2(x_2^2 + x_3^2)}$
τ	twist
τ_{\max}	maximum shear stress
τ_{wall}	wall shear stress
ϕ_1	angle from x_1 -axis to observer
ϕ_2	angle from x_2 -axis to observer
Φ_{qq}	wall-pressure wavenumber-frequency spectrum
ψ	random variables distributed on $[0, 2\pi]$
Ψ	azimuth angle between a wind turbine to an observer
ω	angular frequency
$\tilde{\omega}$	$\omega\delta^*/U_e$

Subscripts

1, 2, 3	indices for streamwise, spanwise, and wall-normal directions
h	high frequency noise

l	low frequency noise
r	component in a radiation direction
n	n^{th} frequency component
avg	average
BPF	blade passing frequency
TEBN	trailing edge bluntness noise
TEN	trailing edge noise
TIN	turbulence ingestion noise

Special functions

\square^2	$(1/c_0^2) \partial^2 / \partial t^2 - \nabla^2$
$E[]$	Fresnel integral
H	Heaviside function
\mathcal{L}	effective lift
δ	delta function

Chapter 1

Introduction

1.1 Wind turbine aerodynamic noise

Wind energy is one of the fastest growing renewable energy resources. However, although wind turbines transform wind energy into electric energy without producing any waste, wind turbines make noise due to the rotational motion of the wind turbine blades. Because this noise can exert a negative influence on people near wind turbines, it is important to evaluate and reduce the noise generated from wind turbines for the expansion of wind energy.

The aerodynamic noise generated from wind turbine blades, which is the dominant noise source of a typical modern wind turbine, is divided into two noise sources: turbulence ingestion noise and airfoil self-noise [1]. The turbulence ingestion noise is generated due to an interaction between atmospheric turbulence and the wind turbine blades, while the airfoil self-noise is generated without the existence of any atmospheric turbulence. The airfoil self-noise is composed of turbulent-boundary-layer trailing edge noise, laminar-boundary-layer vortex shedding noise, separation noise, and trailing edge bluntness noise [2]. Because wind turbines operate at high Reynolds number, the boundary layers on the blades are typically turbulent at the trailing edge. This leads to the generation of turbulent-boundary-layer trailing edge noise. Moreover, trailing edge bluntness noise is sometimes produced by the blades unless the blades

have sharp trailing edges. Hence, among these self-noise sources, the turbulent-boundary-layer trailing edge noise and the trailing edge bluntness noise can be a noise source in a typical operating condition of wind turbines.

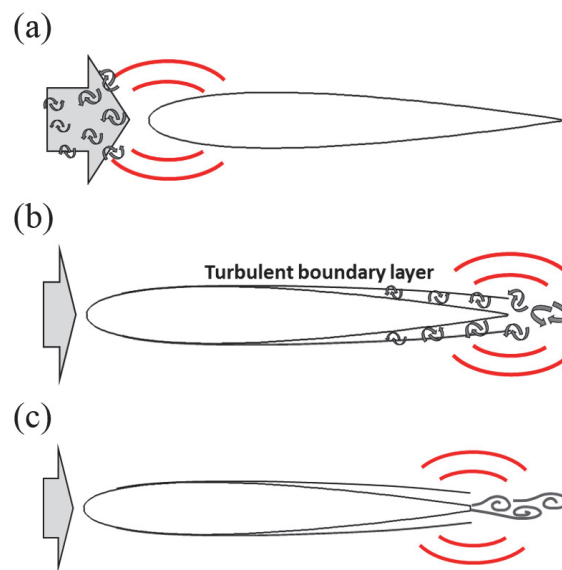


Fig. 1.1 Schematic of the noise mechanism of (a) turbulence ingestion noise, (b) turbulent-boundary-layer trailing edge noise (c) trailing edge bluntness noise

For a modern upwind wind turbine, thickness and loading noise are not a major noise source. Thickness noise is generated when the fluid in the flow field is displaced by the moving blades, and loading noise occurs because the accelerating force generated by the blades is applied to the fluid [3]. This discrete frequency noise is one of the main noise sources of rotating machinery, such as helicopter rotors, turbo-machinery, and fans. However, for a modern upwind wind turbine, the discrete frequency noise is inaudible in most situations, as the rotational speed of a wind turbine is very low.

The wind turbine aerodynamic noise has two acoustical characteristics. From a frequency domain viewpoint, the wind turbine noise is broadband sound [1]. Because both atmospheric turbulence and turbulence eddies in the turbulent-boundary-layer have a broadband spectrum in the wavenumber domain, the corresponding noise exhibits a broadband spectrum. Another important characteristic is that this broadband wind turbine noise is amplitude modulated sound. Wind turbines produce sound with levels that fluctuate periodically at the blade passing frequency. This amplitude modulated sound is heard because the rotational speed of wind turbines extremely low compared to other rotating machinery; this sound, which is called the amplitude modulation of wind turbine noise, is a special characteristic of wind turbine aerodynamic noise. Thus, to assess the wind turbine aerodynamic noise, its amplitude modulated character as well as a broadband spectrum needs to be well examined.

1.2 Current issues

Accurate prediction of wind turbine aerodynamic noise is a very difficult computational problem. To predict wind turbine noise precisely, turbulent flow over and in the vicinity of blade surfaces needs to be simulated because the wind turbine noise is mainly generated due to the interaction between turbulence and the blades. Theoretically, this flow field can be solved by compressible direct numerical simulation or compressible large eddy simulation. Once the time-dependent flow field is solved, the acoustic pressure at an arbitrary point can be predicted by using the acoustic analogy such as Ffowcs Williams and Hawkings equation [4, 5]. However, because the blade length of large wind turbines is enormously large compared to the characteristic length of turbulent eddies, the computational cost for these simulations is too expensive to achieve. These numerical methods are not a possible way to predict wind turbine aerodynamic noise.

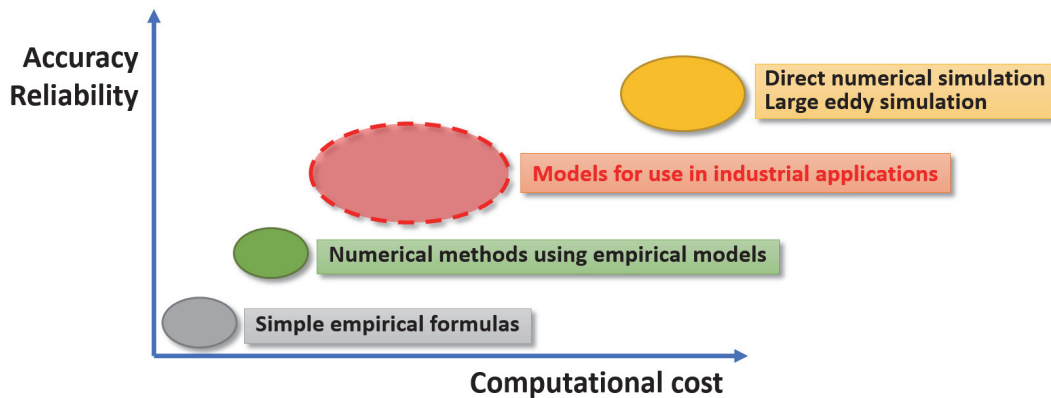


Fig. 1.2. Accuracy or reliability vs. computational cost for the prediction model of wind turbine aerodynamic noise

For this reason, several simple empirical models have been widely used to estimate the sound pressure level of wind turbine aerodynamic noise [1]. Simple prediction formulas estimate the overall sound pressure level with wind turbine parameters such as a power output, rotor diameter, and rotor tip speed. More complicated models in this category can also estimate the sound pressure level in the frequency domain with consideration of the details of the blade geometry, wind turbine operating condition, and atmospheric condition [6]. However, although these simple empirical models provide a reasonable estimate of the sound pressure level in a short computational time, the models are too simple to be applied in the design process of wind turbine blades. Thus, for use in industrial applications a more accurate and reliable numerical model is necessary to predict wind turbine aerodynamic noise.

In particular, developing prediction model for the trailing edge noise is more important than that for the turbulence ingestion noise. Because the intensity of atmospheric turbulence ingested into the rotor disk is difficult to measure and because it always varies with time, it is difficult to precisely predict the sound pressure level of the turbulence ingestion noise even though prediction model for the turbulence ingestion noise is accurate. On the other hand, trailing edge noise can be predicted more accurately irrespective of atmospheric conditions. Consequently, previous studies have been mainly focused on the development of the prediction model for the trailing edge noise.

Another issue with wind turbine aerodynamic noise is the amplitude modulation of wind turbine noise. In the vicinity of a wind turbine, swishing sound is easily heard due to the rotational motion of wind turbine blades. As an observer becomes more distant from the wind turbine, this swishing sound is difficult to perceive. However, several studies have reported that sometimes a periodic thumping sound is perceived even at long distances from wind

turbines [7-10]. Some of them claimed that this thumping sound had a more impulsive characteristic compared to the swishing sound. Although several possible mechanisms were proposed to explain the cause of the thumping sound, the mechanism is still not well understood.

Moreover, several attempts have been made to reduce wind turbine aerodynamic noise. Because turbulence ingestion noise is mainly dependent on the inflow velocity and the atmospheric turbulence, reducing the noise levels associated with it is difficult. On the other hand, the trailing edge noise can be reduced by altering the turbulent boundary layer structure or the trailing edge shape. Accordingly, several studies have been performed to reduce the trailing edge noise, such as by modifying the airfoil shape or attaching noise reduction materials to the blades [11-17]. However, most of these studies have focused on two-dimensional flow. Only a few studies have practically applied these techniques to the design of wind turbine blades to date [16-19].

1.3 Research objective

Three topics related to wind turbine aerodynamic noise are examined in the present study. In the next chapter, a numerical method to predict wind turbine aerodynamic noise is proposed for use in industrial applications. To reduce the computation time but predict the noise reliably, this model employs Amiet's trailing edge noise model [20, 21] with Rozenberg's wall pressure spectral model [22]. In particular, Reynolds-averaged Navier-Stokes (RANS) simulation is carried out to obtain the wall-point pressure spectra at blade sections. The calculated wall-point pressure spectrum and trailing edge noise in two-dimensional flow as well as the calculated wind turbine aerodynamic noise is validated with the results from wind tunnel tests and a field experiment [23]. Finally, using the numerical model, aerodynamic noise from a 3MW horizontal axis wind turbine is predicted.

In Chapter 3, the amplitude modulation of wind turbine noise is numerically investigated. To compare the acoustical characteristics of wind turbine noise depending on the observer location, the aerodynamic noise from a wind turbine is numerically modeled in the time domain [24]. Using the predicted signals, this study not only examines why the amplitude modulation is heard even at long distances from a wind turbine, but also finds the main cause of the amplitude modulation.

Chapter 4 introduces two studies for reducing the trailing edge noise generated from wind turbines. In the first study, the trailing edge noise is reduced by modifying the airfoil shape and the blade planform [18]. Optimization methods that involve genetic algorithms are used to obtain the optimal designs of the airfoil shape and the blade planform. The optimization design is also tested with wind tunnel experiments. In the second study, the trailing edge noise is

reduced by attaching serrated trailing edge on the blades of a 10kW wind turbine [19]. From a field experiment, the effect of the trailing edge serrations on the wind turbine noise reduction is evaluated.

Chapter 2

A prediction model for wind turbine noise

2.1 Overview of wind turbine prediction models

In the early days of wind power development, not only upwind wind turbines but also downwind wind turbines were studied and developed. In contrast to upwind wind turbines, downwind wind turbines produce strong low frequency loading noise due to the interaction between the tower wake and the rotor blades. Several studies proposed a method to predict the loading noise harmonics [25, 26]. In particular, Viterna developed a simple prediction code to calculate the loading noise harmonics with the blade geometry and the operating condition [26]. Calculated noise levels with Viterna's model showed good agreement with measured data. The prediction of the loading noise harmonics, though, is unnecessary for a modern upwind wind turbine.

For the prediction of wind turbine broadband noise, Grosveld first proposed a simple model to calculate one-third octave band sound pressure level for turbulence inflow noise, trailing edge noise, and trailing edge bluntness noise [27]. In this model, the turbulence inflow noise was assumed as a point dipole, while the trailing edge noise and the bluntness noise were obtained by integrating the noise components in the spanwise direction. The trailing edge noise

model was made based on the model of Schlinker and Amiet [28]. The calculated noise spectra were compared with measured data from MOD-0A, MOD-2, WTS-4, and USWP wind turbines. Moreover, Lawson developed a prediction method for wind turbine aerodynamic noise [29]. The two dominant noise sources were modeled: trailing edge noise and turbulence ingestion noise. The models for the trailing edge noise and the turbulence ingestion noise were based on models by Brooks, Pope, and Marcolini [2] and Amiet [30], respectively. Prediction results for the MOD-2 wind turbine were in good agreement with experimental data.

Recently, numerical predictions by use of empirical models were performed for calculating the sound pressure level of wind turbine aerodynamic noise. Zhu et al. numerically modeled the aerodynamic noise from a 300kW wind turbine using a semi-empirical model by Brooks, Pope, and Marcolini [2], and they compared the predicted results with measurement data [6]. Although the semi-empirical model that they used was in terms of NACA0012 airfoil, they successfully calculated the wind turbine noise by altering the input data of the boundary layer displacement thickness so that it matched the data pertaining to the actual airfoil shape of the wind turbine blade; the boundary layer parameters were calculated by XFOIL [31]. Oerlemans and Schepers also predicted the noise from two large wind turbines using the same empirical model [32]. They measured the wind turbine noise using a microphone array and then validated the prediction results with experimental data.

Furthermore, Moriarty, Guidati, and Migliore utilized the TNO model for calculating the trailing edge noise of a wind turbine [33]. The TNO model is originally proposed by Parchen [34]. Although this model also has some empirical parameters, the authors claimed that this model is more physical detail than the semi-empirical model by Brooks, Pope, and Marcolini. In their study, they also proposed a prediction model for turbulence ingestion noise of a wind

turbine. This model is a simplified form of the previous study by the authors [35]. This prediction model can describe the effect of airfoil thickness on the turbulence ingestion noise.

In addition, a full numerical simulation was carried out by Fleig, Iida, and Arakawa to predict noise radiated from a wind turbine [36]. They predicted the aerodynamic noise from a 16.5kW small wind turbine using a compressible large eddy simulation. Far-field noise was calculated using a formulation based on the Ffowcs Williams and Hawkings equation [5]. However, because the computational cost of this method is considerably high, this numerical simulation method is less favorable than the previous introduced models.

In the present study, a numerical method to predict the trailing edge noise from a wind turbine is proposed. This model employs Amiet's original trailing edge noise model [20, 21]. This trailing edge noise model has been widely used for predicting helicopter rotor noise [28], propeller noise [37, 38], and fan noise [39, 40]. However, this original model has been rarely applied to predicting wind turbine noise although this model is used for the basis of other models such as Grosveld's model. The reason may be that there were few models to correctly predict the wall-pressure wavenumber-frequency spectrum, which is the input for Amiet's model. Recently, Rozenberg, Robert, and Moreau develop a wall-pressure spectral model for the flow with adverse mean-pressure gradient (APG) [22]. This empirical model is known to give a reasonable spectrum not only for a flat-plate but also airfoil geometries. Other noise sources of the turbulence ingestion noise and the trailing edge bluntness noise are modeled by Lawson's model [29] and Brooks, Pope, and Marcolini model [2], respectively.

2.2 Numerical method

2.2.1 Trailing edge noise model

When a large wind turbine blade rotates in an open environment, turbulent boundary layers typically develop on the blade surfaces. The turbulent eddies in these boundary layers are a weak radiation source. However, as the turbulent eddies convect downstream, these eddies interact with the trailing edge of the blade, and more sound is radiated. This sound is called the turbulent-boundary-layer trailing edge noise, or the trailing edge noise. Various trailing edge noise theories have been proposed to model this mechanism [20, 21, 41-43]. These theories assume that the turbulent eddies convect in a frozen pattern as they pass the trailing edge. This assumption makes it possible to decompose the total pressure field into an incident and a scattered field. The problem then reduces to determining the scattered pressure resulting from the assumed incident pressure field.

This study uses the model proposed by Amiet [20, 21]. This model assumes the airfoil is a flat plate, and provides a chordwise surface pressure distribution on the flat plate. Although this model is intended for an isolated airfoil, it can be extended to a rotor blade using a strip theory approach, as employed in previous studies [28, 37, 40, 44].

Figure 2.1 presents a schematic for a flat plate in rectilinear motion. The plate is placed in the plane $x_3 = 0$, and moves with velocity U in the negative x_1 -direction. The trailing edge of the plate is aligned with the x_2 -axis, and the origin of the Cartesian coordinate system is at the center of the trailing edge. The incident pressure jump due to turbulent flow at point \mathbf{y} at time t can then be described as

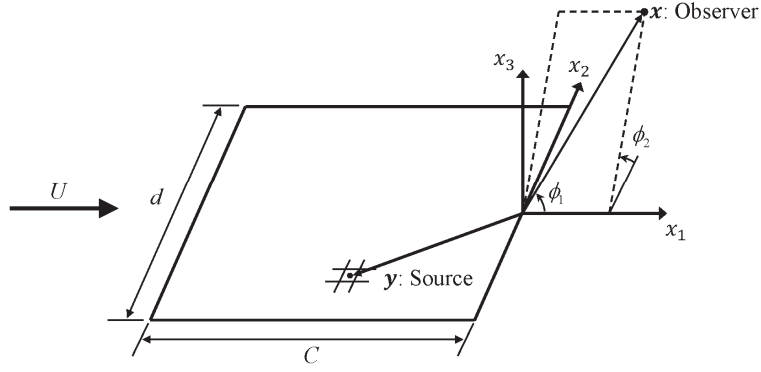


Fig. 2.1. Schematic of the trailing edge noise model problem

$$\Delta p_i(y_1, y_2, t) = \int \int_{-\infty}^{\infty} p_0(k_c, k_2) e^{i(\omega t - k_c y_1 - k_2 y_2)} dk_c dk_2, \quad (2.1)$$

where p_0 is the amplitude of the pressure wavenumber component, k_c is the streamwise convective wavenumber, k_2 is the spanwise wavenumber, and ω is the angular frequency. This surface pressure jump is the difference between the upper and the lower surface pressure. According to Amiet's model, the corresponding scattered pressure jump can be written as

$$\Delta p_s(y_1, y_2, t) = \int \int_{-\infty}^{\infty} p_0 e^{i(\omega t - k_c y_1 - k_2 y_2)} \left\{ -1 + (1+i) E^* \left[-y_1 (k_c + \mu M + \zeta) \right] \right\} dk_c dk_2, \quad (2.2)$$

where M is the Mach number, $\zeta = \sqrt{\mu^2 - k_2^2 / \beta^2}$, $\mu = M\omega / \beta^2 U$, and $\beta = \sqrt{1 - M^2}$. Here $E^* []$ represents the complex conjugate of the Fresnel integral, which is defined as

$$E^*(x) = \frac{1}{\sqrt{2\pi}} \int_0^x e^{-it} \frac{dt}{\sqrt{t}}. \quad (2.3)$$

The total surface pressure jump is the sum of the incident and the scattered pressure jump.

However, as suggested by Amiet [21], to reduce the abrupt increase in incident pressure at the leading edge, the incident pressure jump is multiplied by an exponential convergence factor, $e^{\varepsilon k_c y_1}$, where ε is a positive small value. This makes the incident pressure jump gradually increase near the leading edge. Therefore, the total pressure jump becomes

$$\Delta p_t(y_1, y_2, t) = \iint_{-\infty}^{\infty} p_0 e^{i(\omega t - k_c y_1 - k_2 y_2)} \left\{ e^{\varepsilon k_c y_1} - 1 + (1+i) E^*[-y_1(k_c + \mu M + \zeta)] \right\} dk_c dk_2. \quad (2.4)$$

Based on the surface pressure jump in Eq. (2.4), Amiet calculates the far-field noise using the acoustic analogy by Curle [45]. The detail procedure are explained in Ref. [30] and will not be derived here. The final form of the far-field sound spectrum is

$$S_{pp}(\mathbf{x}, \omega) = \left(\frac{k_1 M x_3 C}{4\pi\sigma'^2} \right)^2 \frac{\pi d}{2U_c} \left| \mathcal{L}(x_1, k_1, k_c, k_2) \right|^2 \Phi_{qq}(k_c, k_2), \quad (2.5)$$

where \mathcal{L} is the effective lift, which is explained in Ref. [28].

The wall-pressure wavenumber-frequency spectrum, Φ_{qq} in Eq. (2.5) is the Fourier wavenumber spectrum of the incident pressure field on the surface. This spectrum can be empirically modeled as the following equation provided that the convection velocity is constant [46].

$$\Phi_{qq}(\omega/U_c, 0) = \frac{U_c}{\pi} S_{qq}(\omega) l_2(\omega) \quad (2.6)$$

Here $S_{qq}(\omega)$ is the wall-point pressure frequency spectrum, and $l_2(\omega)$ is the turbulence correlation length in the spanwise direction [47]. The wall-point pressure frequency spectrum in Eq. (2.6) is predicted by Rozenberg's APG model [22]. In addition, the convection velocity, U_c is a function of frequency, and this relationship is usually given by $U_c \approx 0.5U \sim 0.7U$ for an

airfoil. In this calculation, the convection velocity is assumed to be constant, and is set to $U_c = 0.7U$.

2.2.2 Turbulence ingestion noise model

The turbulence ingestion noise is predicted by an empirical model proposed by Lawson [1, 29]. According to this model, the frequency spectrum can be expressed as

$$\text{SPL}_{\text{TIN}} = \text{SPL}_{\text{H, TIN}} + 10 \log_{10} \left(\frac{K_{lc}}{1 + K_{lc}} \right), \quad (2.7)$$

with

$$\text{SPL}_{\text{H, TIN}} = 10 \log_{10} \left\{ \rho_0^2 c_0^2 l_T \frac{d}{r_e^2} M^3 \overline{D_l} \overline{w}^2 \hat{k}^3 (1 + \hat{k}^2)^{-7/3} \right\} + 58.4, \quad (2.8)$$

where K_{lc} is the low-frequency correction factor, l_T is the atmospheric turbulence length scale, \overline{w} is the turbulence intensity, and \hat{k} is the normalized wave number. The atmospheric turbulence length scale and the turbulence intensity are determined from an empirical model using the ground roughness [48]. These are determined as follows:

$$l_T = 25h^{0.35} z^{-0.063} \quad (2.9)$$

and

$$\overline{w} = \left\{ 0.24 + 0.096 \log_{10} z + 0.016 (\log_{10} z)^2 \right\} \frac{\log(30/z)}{\log(h/z)}, \quad (2.10)$$

where z is the ground roughness and h is the height from the ground.

2.2.3 Trailing edge bluntness noise model

A semi-empirical model proposed by Brooks, Pope, and Marcolini is used to calculate the trailing edge bluntness noise [2]. This model is developed based on wind tunnel experiments using a NACA0012 airfoil. With this semi-empirical model, the 1/3 octave band sound pressure level of the trailing edge bluntness noise can be calculated as

$$\text{SPL}_{\text{TEBN}} = 10 \log \left(\frac{h_e M^{5.5} d \overline{D}_h}{r_e^2} \right) + G_4 \left(\frac{h_e}{\delta_{avg}^*}, \nu \right) + G_5 \left(\frac{h_e}{\delta_{avg}^*}, \nu, \text{St}_{\text{peak}} \right), \quad (2.11)$$

where h_e is the bluntness height of the trailing edge, St is the Strouhal number based on the trailing edge height, δ_{avg}^* is the average boundary layer displacement thickness of the suction and the pressure side, and ν is the solid angle between beveled surfaces near the trailing edge. The function, \overline{D}_h is the directivity function for high frequency noise, and G_4 and G_5 are the functions that determine the peak level and the shape of the noise spectrum, respectively. The details of the functions, \overline{D}_h , G_4 , and G_5 are given in Ref. [2].

2.2.4 Wall-pressure spectral model

In principle, the wall-point pressure frequency spectrum can be accurately obtained by wind tunnel experiments or large eddy simulations. However, repeated tests under different configurations are difficult to perform with experiments or extensive numerical simulations. Accordingly, the present study adapts an empirical spectral model proposed by Rozenberg, Robert, and Moreau [22]. This model is an extended version of Goody's model [49] for the flow with adverse pressure gradient. According to Rozenberg's model, the wall-point pressure spectrum can be expressed as

$$\frac{S_{qq}(\omega)U_e}{\tau_{\max}^2\delta^*} = \frac{\left\{2.82\Delta^2(6.13\Delta^{-0.75} + F_1)^{A_1}\right\}\left\{4.2\left(\frac{\Pi}{\Delta}\right) + 1\right\}\tilde{\omega}^2}{(4.76\tilde{\omega}^{0.75} + F_1)^{A_2} + (C'_3\tilde{\omega})^{A_2}}, \quad (2.12)$$

where

$$F_1 = 4.76\left(\frac{1.4}{\Delta}\right)^{0.75} (0.375A_1 - 1),$$

$$A_1 = 3.7 + 1.5\beta_c, \quad A_2 = \min\left[3, \frac{19}{\sqrt{R_T}}\right] + 7,$$

$$C'_3 = 8.8R_T^{-0.57}.$$

In Eq. (2.12), $\tilde{\omega}$ is the non-dimensional circular frequency defined as $\tilde{\omega} = \omega\delta^*/U_e$, Δ is the ratio of the boundary layer thickness to the boundary layer displacement thickness, β_c is the equilibrium parameter defined as $\beta_c = (\theta/\tau_w)(dp/dx)$ by Clauser [50], Π is the wake strength parameter, and R_T is the ratio of the outer layer to inner layer timescale defined in Ref. [49].

2.3 Model validation

2.3.1 Wall-point pressure spectrum with RANS simulation and XFOIL

The numerical method for predicting wall-point pressure spectrum of wing surfaces is validated before predicting trailing edge noise. In order to utilize wall-pressure spectral model proposed by Rozenberg, inner and outer boundary layer variables as well as pressure and skin-friction coefficients should be predicted. In this section, Reynolds-averaged Navier-Stokes (RANS) simulation is carried out to obtain these variables. These variables are first validated with experimental data to confirm that they are properly predicted, and then the predicted wall-point pressure spectra are compared with experiment results.

A two-dimensional RANS simulation is carried out for NACA0012 airfoil using ANSYS Fluent version 13.0, a commercial computational fluid dynamics (CFD) software. In all computations presented in this section, the pressure-based coupled solver is used for improving the rate of solution convergence. Turbulence is modeled using the $k - \omega$ shear stress transport (SST) turbulence model because it is known that this model gives good results in adverse pressure gradients flow, which is a typical flow around airfoils with positive angle of attack [51]. The spatial discretization employs second-order schemes.

Figure 2.2 shows the mesh used in the computation. The computation domain extends to a distance of 25 times the chord length from the airfoil in the wake zone and 18 times the chord length in upper, lower, and forward directions. The y^+ value of the first cells above the wall lies between 0.9 and 1.0, and the expansion ratio above the wall is less than 1.1.

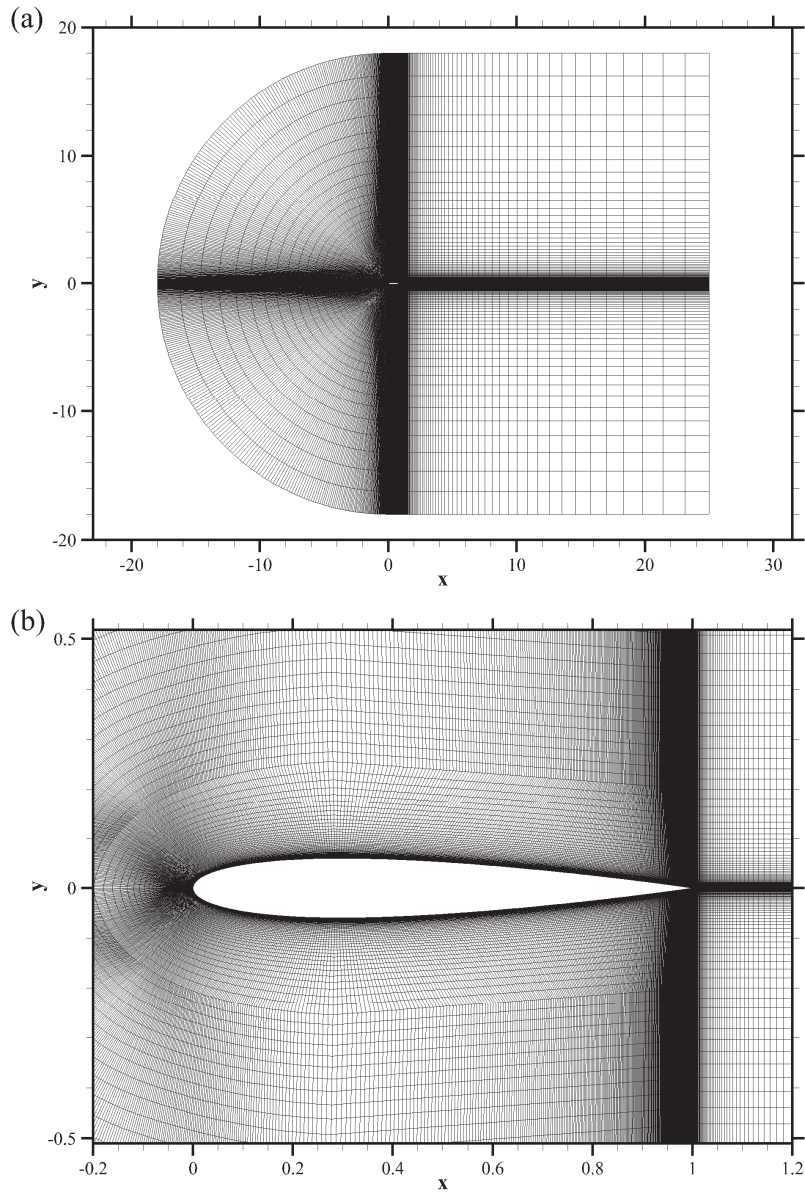


Fig. 2.2. Computational mesh: (a) entire domain (b) zoom on airfoil vicinity

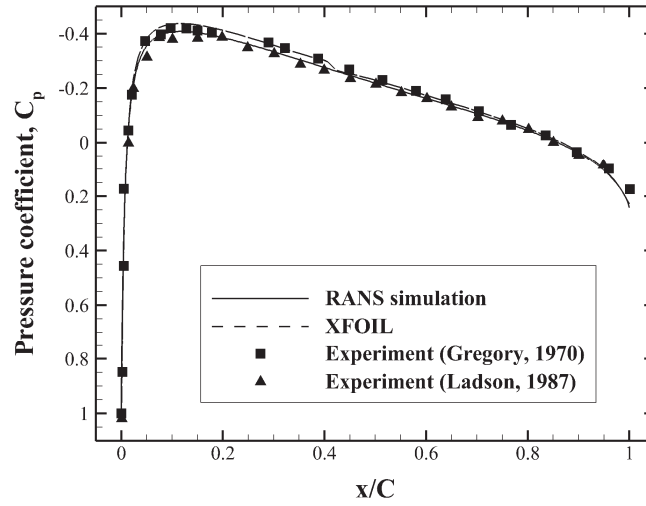


Fig. 2.3. Comparison of chordwise pressure distribution between the results of the two simulations and experiments

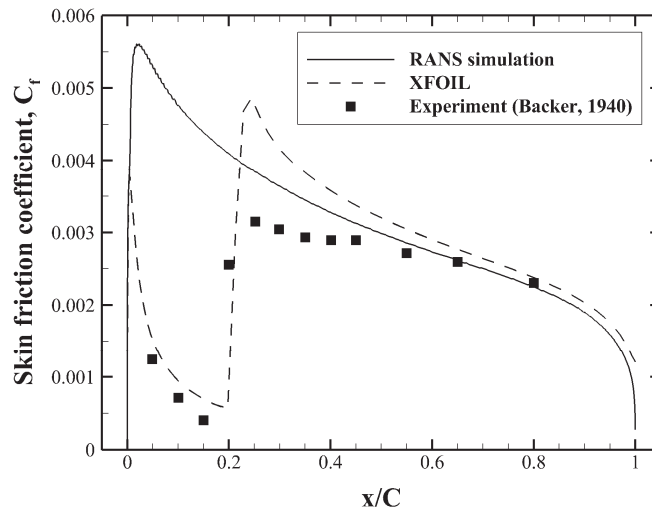


Fig. 2.4. Comparison of skin friction coefficient between the results of the two simulations and an experiment

Moreover, XFOIL is used to calculate the velocity profile and pressure distribution on an airfoil [31]. XFOIL is a well-known open-source program for airfoil analysis by a viscous-inviscid coupling approach. The viscous formulation of XFOIL consists of three integral boundary layer equations: the momentum thickness, the kinetic energy shape parameter, and the maximum shear stress coefficient equations. It also utilizes the e^n method for the prediction of transition location. For use in this study, XFOIL is modified by the author, so it can calculate various boundary layer variables and wall-point pressure frequency spectrum.

All calculations are made for a NACA0012 airfoil at a zero angle of attack but with different inflow velocities. The inflow velocities are chosen to match the Reynolds number to that of experimental cases. First of all, the chordwise pressure distribution obtained from the RANS simulation is compared with that from two experiments. The Reynolds number based on the chord length for an experiment by Gregory and O'Reilly [52] was $Re = 2.88 \times 10^6$, and that for an experiment by Ladson et al. [53] was $Re = 6.0 \times 10^6$. The boundary layer was not tripped in both cases. The comparison of chordwise pressure distribution between the results of the simulations and the two experimental cases is shown in Fig. 2.3; In both calculations the Reynolds number for the simulation is $Re = 6.0 \times 10^6$. A good agreement of the pressure coefficients is obtained between the two simulation results and the experimental data.

In addition, the skin friction coefficients obtained from the two simulations are compared with that from an experiment by Becker [54], as plotted in Fig. 2.4. The experiment was carried out at a Reynolds number of $Re = 1.025 \times 10^7$ with forced transition occurring at 0.2 of the chord length. Because the $k-\omega$ SST model cannot take into account laminar turbulent transition, the RANS simulation result gives poor agreement with the experimental result in

laminar and transitional regions. A large discrepancy is also found in transitional region between the result obtained by XFOIL and the experimental result. However, these discrepancies become small near the trailing edge, where the values are used for the prediction of surface pressure spectrum.

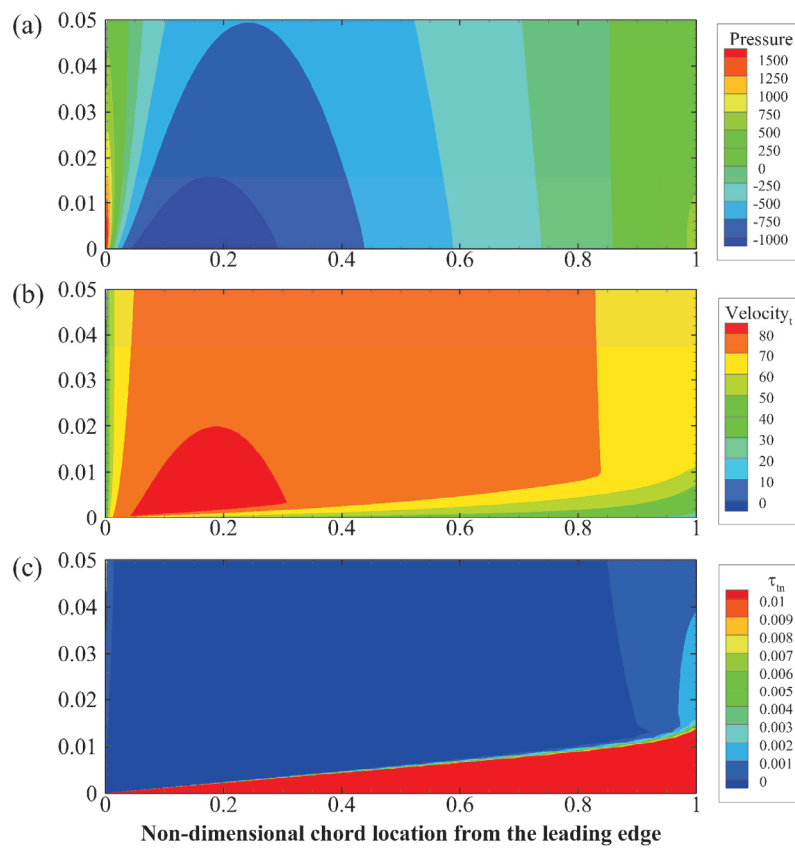


Fig. 2.5. The RANS simulation results for (a) pressure, (b) tangential velocity, and (c) shear stress along the upper side of NACA0012 airfoil

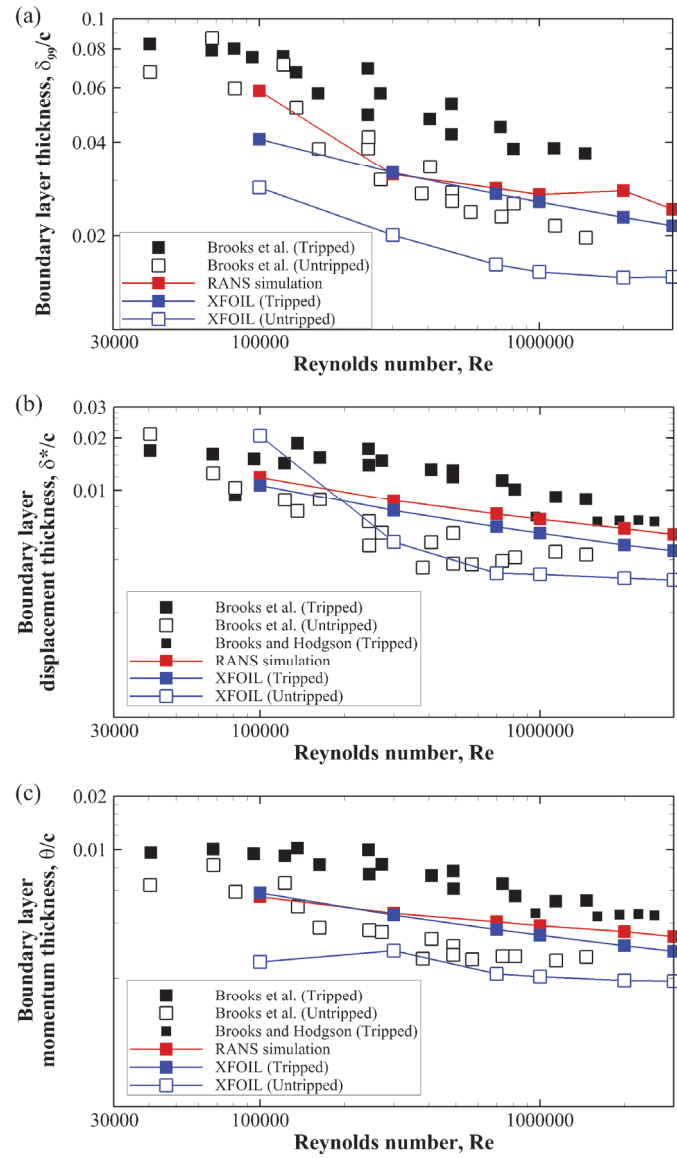


Fig. 2.6. Comparison of boundary layer thickness, displacement thickness, and momentum thickness between the results of the two simulations and experiments

Furthermore, an in-house post-processing code for the RANS simulation is developed to determine the edge of the boundary layer and calculate the boundary layer parameters. Pressure, tangential velocity, and shear stress along the upper side of the airfoil is obtained as shown in Fig. 2.5. The edge of the boundary layer is then determined when the shear stress is less than a criterion value between 0.001 and 0.00001. The boundary layer variables obtained from the RANS simulation are selected at 99.6% chord from the leading edge.

Using these results, the validation of the boundary layer thickness, displacement thickness, and momentum thickness is carried out with a comparison with the experiments of Brooks, Pope, and Marcolini [2] and Brooks and Hodgson [55], plotted in Fig. 2.6. For the cases of the tripped boundary layer of Brooks et al. and Brooks and Hodgson, forced transitions were achieved at 20% and 15% chord from the leading edge, respectively. For the case of XFOIL forced transition is assumed at 20% chord the leading edge, and the boundary layer variables are extracted at the trailing edge. The comparison results show that the boundary layer displacement thickness and momentum thickness agree well, while the boundary layer thickness does not. In particular, this discrepancy is considerable at Reynolds numbers below about one million. However, this difference is small at high Reynolds number in which wind turbine blades operate.

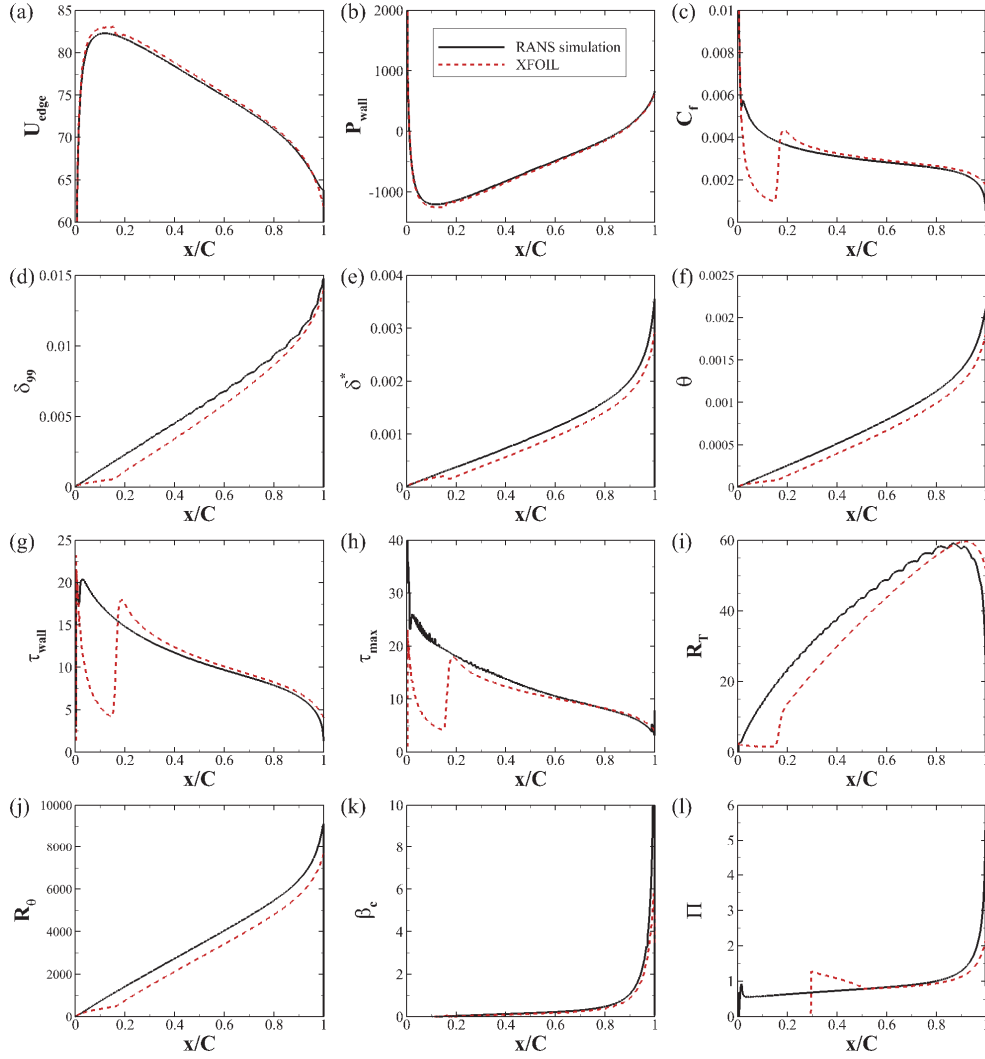


Fig. 2.7. Chordwise distributions of the inner and outer boundary layer variables obtained from RANS simulation and XFOIL: (a) boundary layer edge velocity, (b) pressure at the wall, (c) skin friction coefficient, (d) boundary layer thickness, (e) boundary layer displacement thickness, (f) boundary layer momentum thickness, (g) wall shear stress, (h) maximum shear stress, (i) ratio of timescales of pressure, (j) Reynolds number based on U_e and θ , (k) Clauser's parameter, (l) wake strength parameter

Finally, the wall-point pressure frequency spectrum is calculated using the model proposed by Rozenberg [22] and compared with the result of the experiment by Brooks and Hodgson [55]. The validation case is an inflow velocity of $U = 69.5\text{m/s}$. To utilize the wall-pressure spectral model, boundary layer variables are first calculated by RANS simulation and XFOIL. The predicted chordwise distribution of the boundary layer variables are plotted in Fig. 2.7. The maximum shear stress for XFOIL is calculated by using wall shear stress and velocity profile in the boundary layer, instead of using shear stress coefficient, C_τ . The predicted results of RANS simulation and XFOIL are somewhat different, but these differences become small near the trailing edge. Figure 2.8 compares the velocity profile at $x/C = 0.991$ in the boundary layer between RANS simulation and XFOIL. It is seen that the shear stress is the maximum at the wall for both simulations.

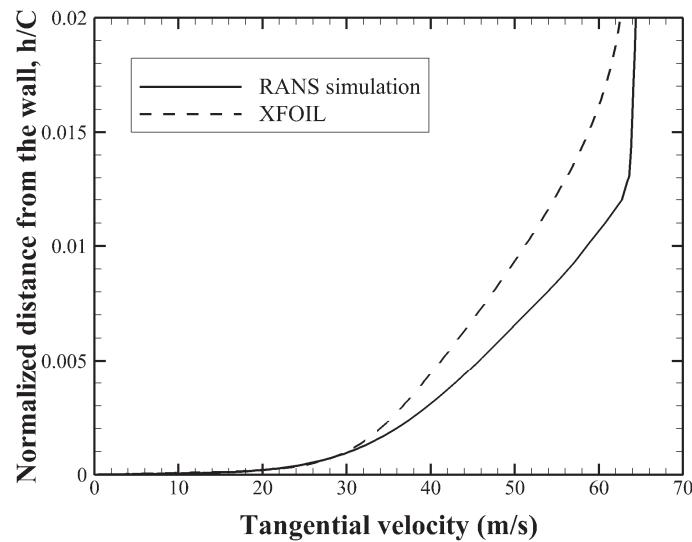


Fig. 2.8. Comparison of velocity profile at $x/C = 0.991$ in the boundary layer between RANS simulation and XFOIL

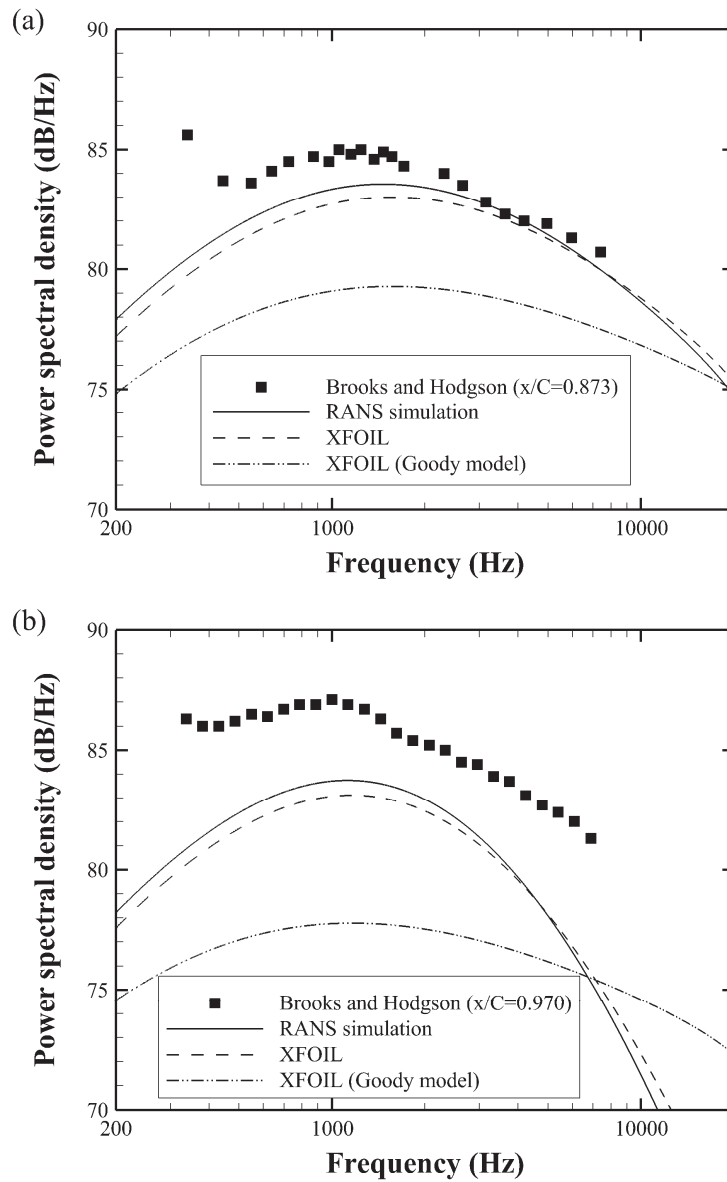


Fig. 2.9. Comparison of wall-point pressure frequency spectrum between the results of the two simulations and experiments by Brooks and Hodgson

Figure 2.9 compares the wall-point pressure frequency spectrum between the experimental data and the predicted results of RANS simulation and XFOIL. The results indicate that Rozenberg's model with RANS simulation or XFOIL gives better prediction than Goody's model. Note that the spectra obtained from XFOIL are little different from those from RANS simulation.

2.3.2 Trailing edge noise

In this section, the validation of the prediction method for trailing edge noise is performed with a comparison with the result of the experiment by Brooks and Hodgson [55]. The validation case is identical to the case of calculating Figs. 2.7 to 2.9. Thus, the boundary layer variables used in this calculation can be found in Fig. 2.7. For the calculation of the wall-point pressure frequency spectrum, the boundary layer variables calculated by the RANS simulation and XFOIL are extracted at 99.5% and 99% chord from the leading edge, respectively.

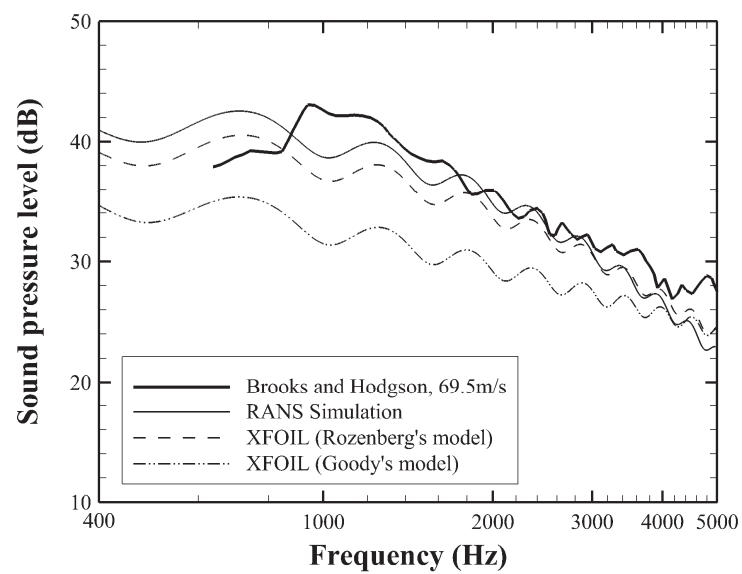


Fig. 2.10. Measured and predicted far-field acoustic spectra of trailing edge noise

The predicted narrowband spectra obtained from RANS simulation and XFOIL are compared with the measurement data of Brooks and Hodgson in Fig. 2.10. The narrowband spectrum calculated by Goody's model is over 10dB lower than that of the experimental data because this model does not reflect the pressure gradient near the trailing edge. On the other hand, the narrowband spectra calculated by Rozenberg's model agree well with those of the experimental data. Although a discrepancy between the numerical results and the experimental data is seen near 1kHz, predicting low frequencies of trailing edge noise is less important for wind turbine noise because turbulence ingestion noise is typically dominant in this frequency range.

In addition, a comparison is made with the experiment of Brooks, Pope, and Marcolini [2]. Figure 2.11 compares the measured and predicted 1/3 octave band spectra at inflow velocities of $U = 71.3\text{m/s}$ and 39.6m/s . As it can be expected, the 1/3 octave band spectrum calculated by RANS simulation agrees well with the experimental data. Moreover, a good prediction is also achieved when XFOIL is used for the calculation of the wall-point pressure spectrum. In particular, the accordance between the spectrum obtained from XFOIL and the experimental data is excellent in high frequencies, while the spectrum obtained from RANS simulation drops rapidly with frequency in high frequencies. From these results, it can be seen that Amiet's model with Rozenberg's model whose boundary layer variables are obtained with XFOIL can be a good numerical method to predict trailing edge noise.

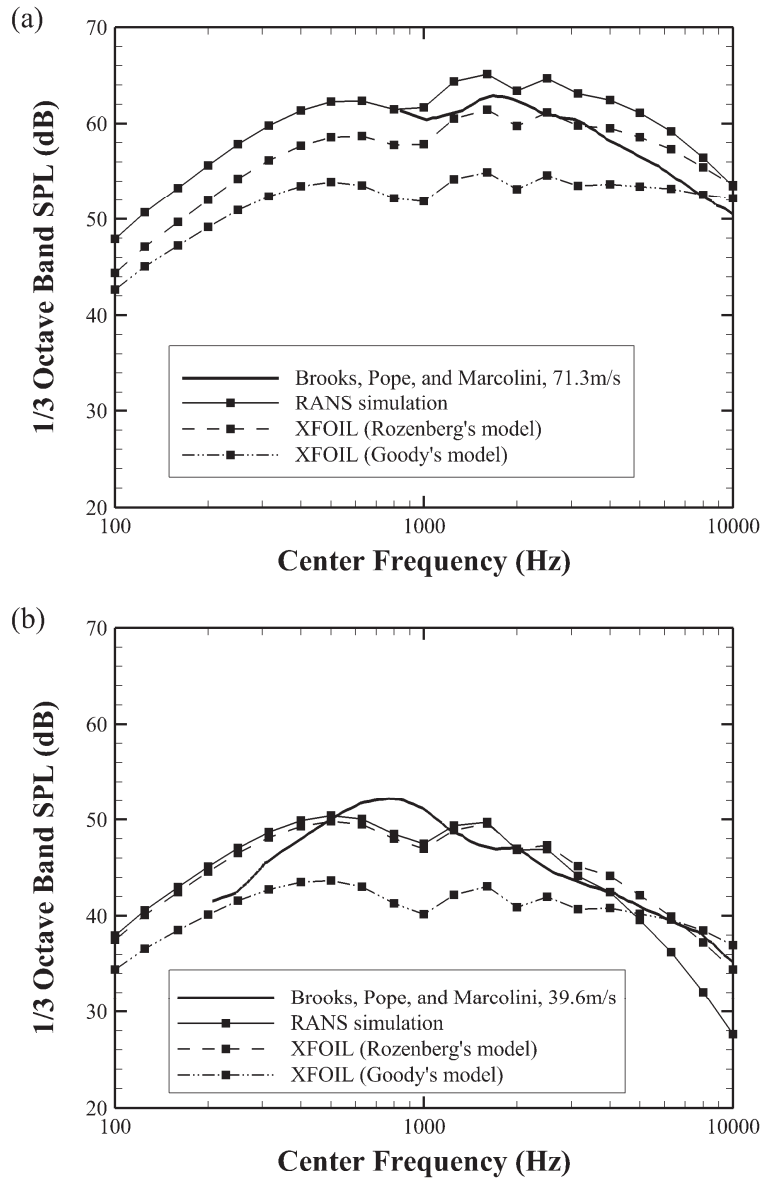


Fig. 2.11. Measured and predicted 1/3 octave band spectra of trailing edge noise for inflow velocities of (a) 71.3m/s and (b) 39.6m/s

2.3.3 Wind turbine aerodynamic noise

2.3.3.1 Noise measurement

To validate the numerical method for predicting wind turbine aerodynamic noise, noise measurements were carried out with a 10kW three-bladed horizontal axis wind turbine [23]. This wind turbine, which was developed for an experimental purpose, is located in Gyeonggi Province, Korea. Figure 2.12 presents a photograph of the wind turbine. The rotor diameter and the hub height of the wind turbine were 8m and 18m, respectively. The wind turbine began to rotate at a wind speed of 1.5m/s, and the rotational speed increased with an increase in the wind speed. The wind turbine reached its rated rotational speed of 180RPM at a wind speed of about 10m/s. After a wind speed of 12m/s, the wind turbine was stopped by yawing the rotor from the wind direction.

At the test site, a computer was installed and connected to the wind turbine monitoring system. This computer recorded the rotational speed and power output of the wind turbine. Furthermore, an anemometer and a wind vane were mounted on the tower at a height of 10m from the ground, as shown in Fig. 2.12. They were used to measure the wind speed and direction at the site during the experiment. These data were also recorded in the computer in one-minute intervals.

Acoustic signals were recorded by three sets of hand-held sound level meters (Brüel & Kjær type 2250) with free-field microphones (Brüel & Kjær type 4190), as shown in Fig. 2.13. The microphones were mounted on circular boards 1m in diameter and were connected to hand-held sound level meters with extension cables. The microphones were covered with foam windscreens to minimize the wind noise. Acoustic signals were recorded with a sampling rate



Fig. 2.12. Photograph of a 10kW small wind turbine model

of 48 kHz. One microphone was positioned in the downwind direction at a distance of 22m from the wind turbine, which is the reference position according to the IEC 61400-11 standard [56]. The other two microphones were placed at an offset of 30 degrees from the downwind position. When the wind turbine yawed more than 15 degrees from the initial position, the other microphone close to the downwind direction took over the acoustic measurement.

The measured acoustic signals were divided into one-minute intervals. The 1/3 octave band spectra were obtained from the acoustic signals. Using these spectra, the average 1/3 octave band spectra were calculated for each integer wind speed bin. In addition to the measurement of acoustic signals, inflow wind speed, power output, and wind turbine rotational speed were measured at intervals of one minute. These data were recorded synchronously with the acoustic signals.



Fig. 2.13. Noise measurement with a handheld sound pressure level meter and a microphone

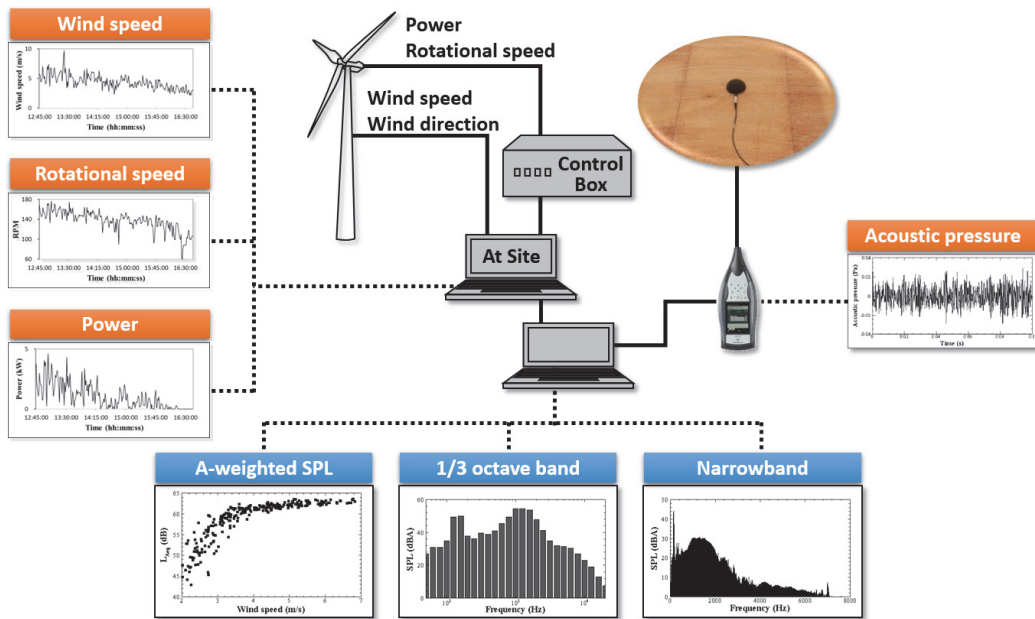


Fig. 2.14. Schematics of wind turbine measurement and post-processing procedure

2.3.3.2 Results

The measured power and the rotational speed of the wind turbine with respect to the wind speed are presented in Fig. 2.15. Each point shown in Fig. 2.15 represents data averaged for one minute. The electrical power began to be generated at a wind speed of about 3m/s and increased with an increase in the wind speed. During the measurement, the wind speed rose to about 7m/s. The corresponding rotational speed ranged from about 50RPM to 170RPM.

A strip theory approach is used to apply the two-dimensional models to rotating wind turbine blades. Each blade is divided into 20 segments of equal lengths, and the three prediction models for the trailing edge noise, turbulence ingestion noise and trailing edge bluntness noise are then applied to the segments. The trailing edge noise is predicted by Amiet's model, and the wall-point pressure spectra are calculated by Rozenberg's model with use of XFOIL. The prediction code for wind turbine noise used in this work is integrated with XFOIL for fast calculations.

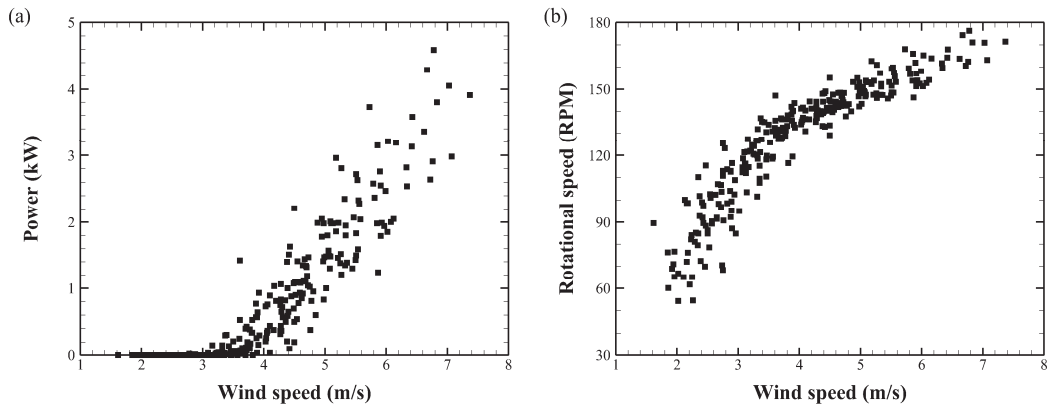


Fig. 2.15. (a) Measured power and (b) rotational speed with respect to wind speed

A 1/3 octave band spectrum analysis was performed, as shown in Fig. 2.16. In the experimental data, a large peak was found from 100Hz to 200Hz. This low-frequency noise is the mechanical noise from the generator. However, this low-frequency mechanical noise cannot be modeled in a numerical analysis because numerical predictions only include the aerodynamic noise from the wind turbine rotor. Note that the large peak due to mechanical noise is not a typical characteristic of small wind turbines. The mechanical noise from the 10kW wind turbine was not reduced well, as it was developed for experimental purposes.

Except for the mechanical noise, the spectral trends of the prediction results agree well with that of the experimental data. The results of the numerical prediction indicate that low-frequency broadband noise was generated due to the turbulent ingestion noise, while the turbulent-boundary-layer trailing edge noise influenced the high-frequency broadband noise. Furthermore, trailing edge bluntness noise caused a quasi-tone in the frequency range of 1kHz to 2kHz. However, at low wind speeds, the measured peak level for the trailing edge bluntness noise was much higher than that of the prediction results. This error may stem from the fact that the boundary layer displacement thickness was not predicted well at low wind speeds due to a laminar-turbulent transition.

Note that for this small wind turbine, trailing edge noise is dominant in high frequencies over 4kHz. For a typical large wind turbine, high frequency noise is less important because this high frequency noise at immission points is greatly attenuated by atmospheric absorption. However, because small wind turbines are generally located in the vicinity of a dwelling, the high-frequency trailing edge noise can be an important noise source.

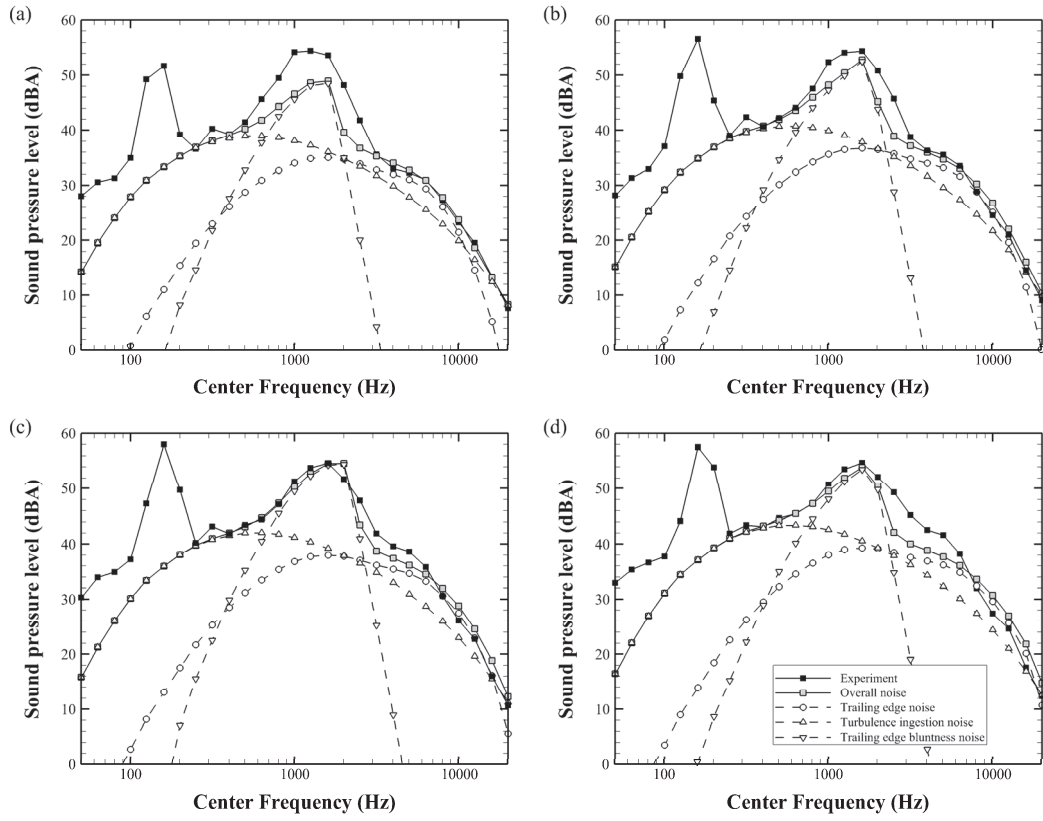


Fig. 2.16. 1/3 octave band spectra of the measured data and the numerical predictions at wind speeds of (a) 4m/s, (b) 5m/s, (c) 6m/s, and (d) 7m/s

2.4 Results

2.4.1 Wind turbine model

Using the numerical method validated in the previous section, aerodynamic noise from a large wind turbine is predicted in this section. The wind turbine model used in the calculation is a 3MW three-blade horizontal axis wind turbine that has typical multi-MW wind turbine characteristics. This turbine is a pitch regulated, variable speed type with a rotor diameter of 91.6m and a hub height of 90m. The specification of the wind turbine model is presented in Table 2.1. Figure 2.17 shows the wind turbine blade planform for the 3MW wind turbine, and the operating schedule for the pitch and rotational speed of the wind turbine is plotted in Fig. 2.18.

Table 2.1. Specification of the wind turbine model

Rated power	3MW
Rotor diameter	91.6m
Number of blades	3
Hub height	90m
Cut in wind speed	4m/s
Rated wind speed	13m/s
Cut out wind speed	25m/s

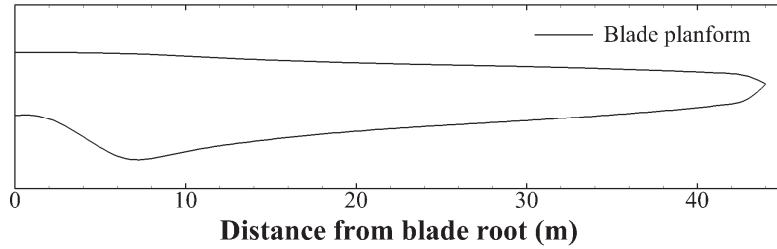


Fig. 2.17. Blade planform for a 3MW wind turbine model

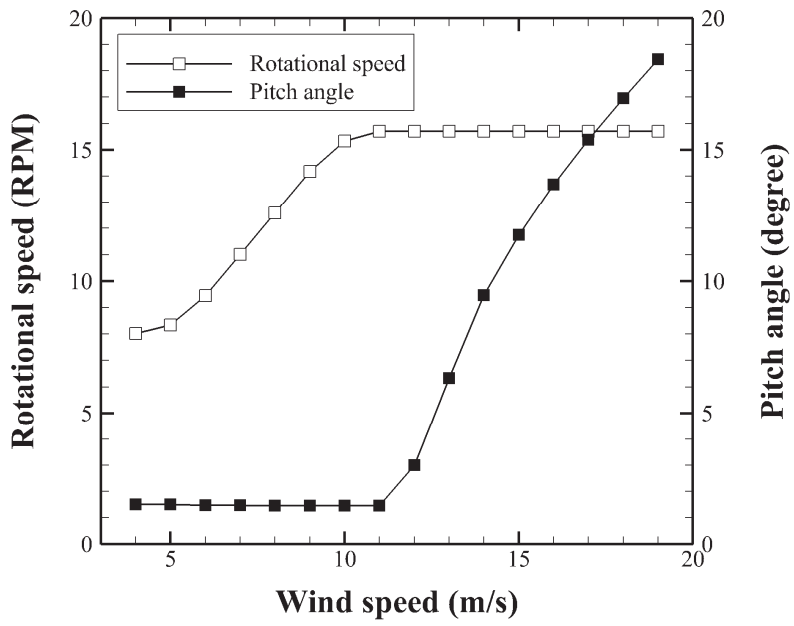


Fig. 2.18. Operating schedule of 3MW wind turbine: pitch angle and rotational speed

2.4.2 Aerodynamic analysis

An aerodynamic analysis is first made to obtain the relative inflow velocity and effective angle of attack of each segment. Aerodynamic power is calculated at wind speeds from 4m/s to 15m/s using WINFAS [57], which is an in-house program using a vortex lattice method. The calculated aerodynamic power is shown in Fig. 2.19. During the calculations, inflow wind speed is assumed to be uniform over the rotor plane. It is shown that the shaft power increases as the wind speed increases until the rated wind speed. Figures 2.20 and 2.21 present the calculated sectional relative inflow velocity and effective angle of attack at three wind speeds, respectively. It can be seen that the sectional inflow velocity and angle of attack increase with increasing wind speed. These results will be used as input for the noise prediction.

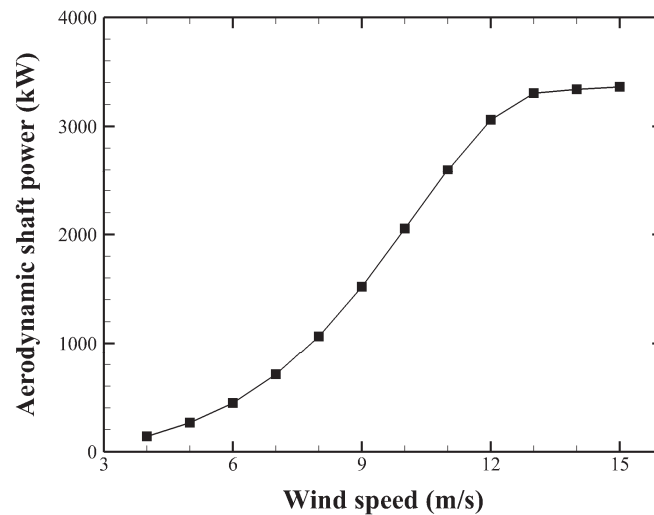


Fig. 2.19. Calculated aerodynamic shaft power with respect to wind speed

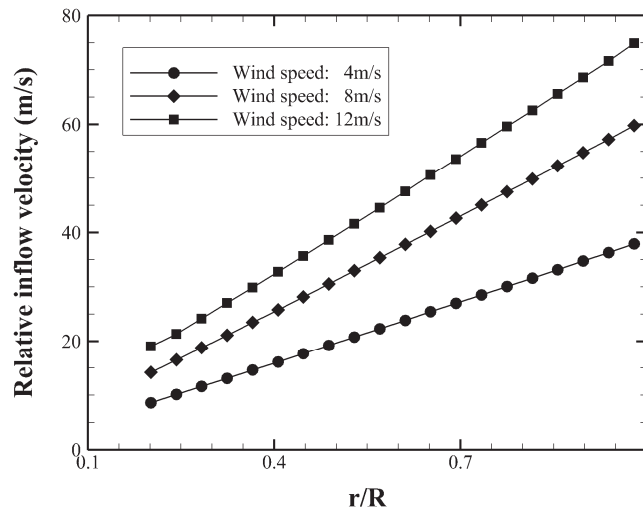


Fig. 2.20. Calculated sectional relative inflow velocity at three wind speeds

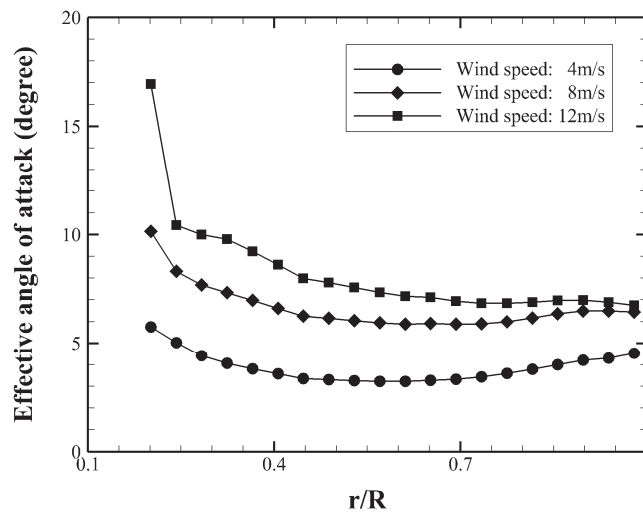


Fig. 2.21. Calculated sectional effective angle of attack at three wind speeds

2.4.3 Noise prediction

Using the results of the aerodynamic analysis in the previous section, the aerodynamic noise from the wind turbine is predicted in this section. First, noise is calculated with use of RANS simulation at a wind speed of 14m/s. The predicted wall-point pressure spectrum are shown in Fig. 2.22. The wall-point pressure spectra are obtained at $x/C = 0.95$ from the leading edge. It is shown that the peak frequency and the magnitude of the power spectrum density increase as the radial distance is close to the outboard region. Figure 2.23 presents the 1/3 octave band spectrum of the trailing edge noise which is predicted using the wall-point pressure spectra in Fig 2.22. The frequency spectrum of the turbulence ingestion noise calculated by Lawson's empirical model is also shown in Fig. 2.23. The observer is assumed to be located at the reference position according to the IEC 61400-11 standard [56]; the observer is located in the downwind direction, and the distance from the wind turbine to the observer position is equal to the sum of the hub height and the rotor radius. The result indicates that low-frequency broadband noise was generated due to the turbulent ingestion noise, while the turbulent-boundary-layer trailing edge noise partly influenced the high-frequency broadband noise. This trend is identical to that of previous studies [1].

The wind turbine aerodynamic noise is also predicted at the same inflow wind speed with use of in-house code developed based on XFOIL. Figure 2.24 compared the trailing edge noise between the 1/3 octave band spectra calculated by RANS simulation and XFOIL. As discussed in the validation section, the trailing edge noise spectrum calculated by RANS simulation drops more rapidly than that by XFOIL in high frequencies. Thus, the spectrum obtained from XFOIL is more plausible than that from RANS simulation.

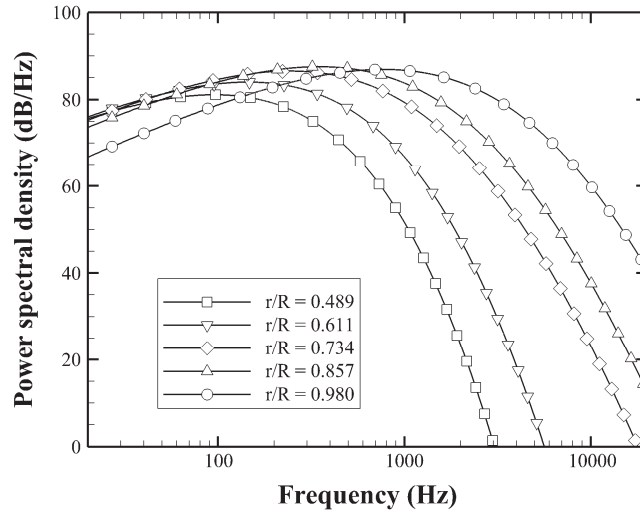


Fig. 2.22. Predicted sectional power spectral density with RANS simulation

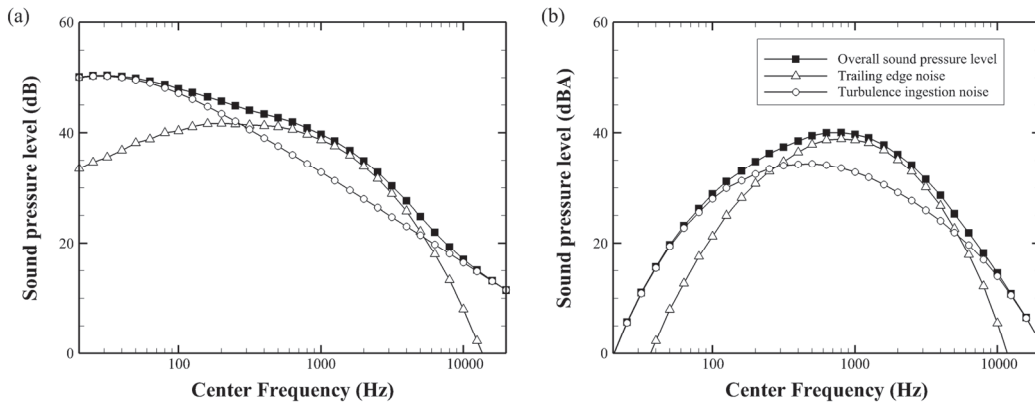


Fig. 2.23. (a) Predicted 1/3 octave band spectrum and (b) A-weighted 1/3 octave band spectrum of trailing edge noise and turbulence ingestion noise with RANS simulation

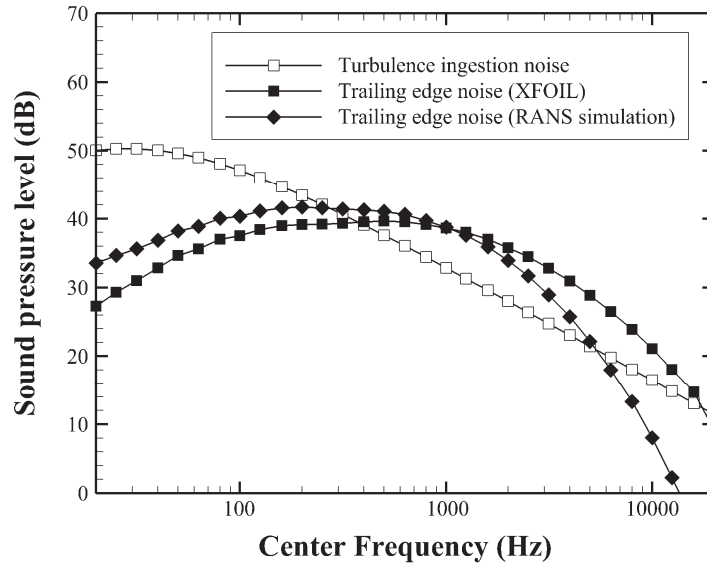


Fig. 2.24. Comparison of 1/3 octave band spectrum between RANS simulation and XFOIL

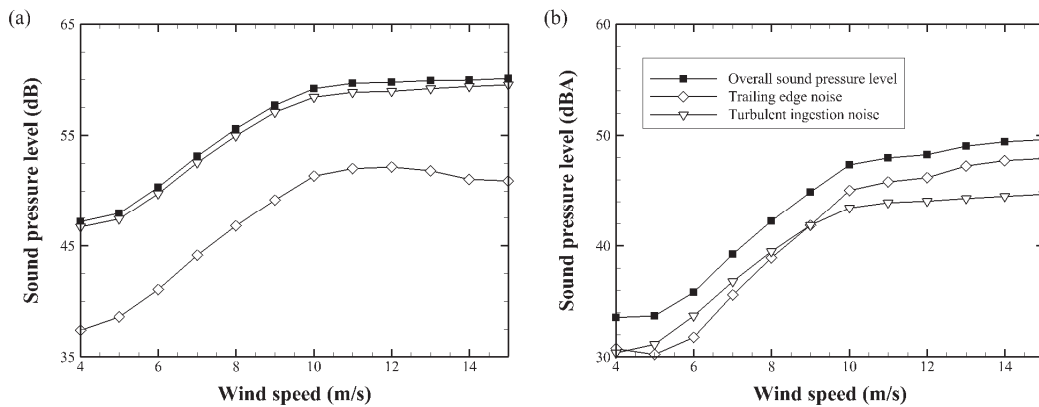


Fig. 2.25. (a) Overall sound pressure level (b) A-weighted sound pressure level of wind turbine noise with respect to wind speed

Moreover, the sound pressure levels of the trailing edge noise and turbulence ingestion noise are calculated at wind speeds of 4 to 15m/s in Fig. 2.25. Because the wind turbine model is variable speed type, the sound pressure level increases as the wind speed increases. At low wind speeds the sound pressure level increases rapidly with increasing wind speed, while the wind turbine noise maintains its sound level at high wind speeds. In addition, note that the sound pressure level of turbulence ingestion noise is significantly higher than that of trailing edge noise. On the other hand, the A-weighted sound pressure level of trailing edge noise is comparable to that of turbulence ingestion noise.

Additionally, the sound pressure level with respect to the distance from the wind turbine is plotted in Fig. 2.26. The wind turbine noise is predicted in the downwind direction at a wind speed of 14m/s. It is seen that the sound pressure level decreases by 6dB per doubling of distance. It is also of note that the sound pressure level of wind turbine aerodynamic noise decreases in the vicinity of the wind turbine. This trend occurs because the wind turbine blades radiate little noise in the plane of the rotor disk. The directivity of trailing edge noise and its effect on the sound directivity of wind turbine noise will be discussed further in the next chapter.

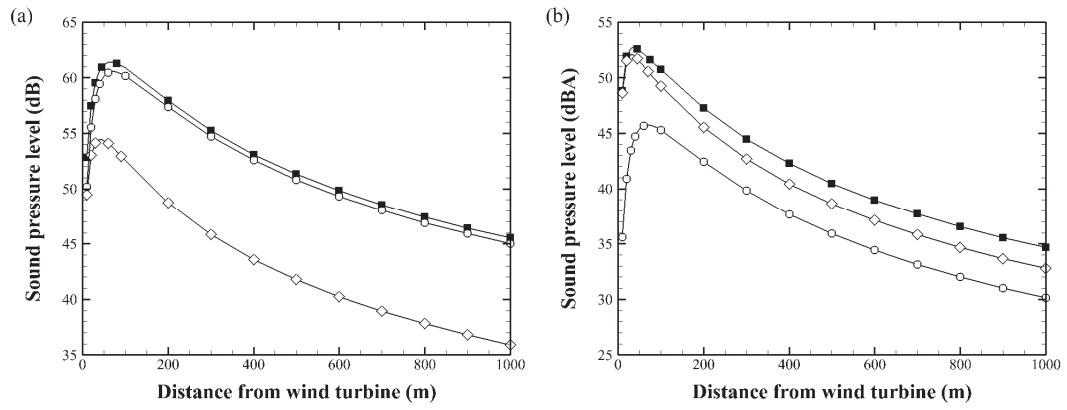


Fig. 2.26. (a) Overall sound pressure level (b) A-weighted sound pressure level with respect to distance from the wind turbine in the downwind direction at a wind speed of 14m/s.

2.5 Discussion

Using the numerical method proposed in this chapter, this study successfully predicts the aerodynamic noise from wind turbines. This method gives more reliable results than other methods for predicting trailing edge noise such as a semi-empirical formula proposed by Brooks, Pope, and Marcolini. Because the semi-empirical formula was made based on experiments for measuring noise from NACA0012 airfoil models, it was questionable whether the application of this formula to other airfoils is appropriate or not. On the other hand, the surface pressure spectral model proposed by Rozenberg, Robert, and Moreau is an empirical model made from several numerical and experimental cases. Thus, this model would be more suitable for the prediction of wind turbine aerodynamic noise.

Moreover, the computational cost of the proposed method with RANS simulation is much lower than that of methods using direct numerical simulations or large-eddy simulations. In particular, the wind turbine noise can be calculated in less than a minute provided that the wall-point pressure spectrum is obtained with XFOIL. Hence, the prediction code developed based on XFOIL in this work could be used when fast computation is necessary, such as the design optimization of wind turbine blades.

However, more studies are still needed to predict wind turbine noise accurately using the proposed method. Although Rozenberg's APG model can take into account adverse pressure gradient flow, this model cannot be applied when the angle of attack is high or the flow is stalled. For wind turbine blades, the angle of attack can be high enough to be stalled in inboard regions, as shown in Fig. 2.20.

It should be noted that this study only predicts the aerodynamic noise from wind turbines. In a real wind turbine, noise is also emitted from the generator or gearbox in a nacelle, which is typically classified as mechanical noise. Thus, the sound pressure level of the noise measured from a real wind turbine can be higher than that predicted in this chapter. In addition, the sound pressure level of turbulence ingestion noise can vary depending on atmospheric conditions such as turbulence intensity and turbulence length scale.

Chapter 3

Time domain simulation of wind turbine noise

3.1 Introduction

3.1.1 Amplitude modulation of wind turbine noise

In the previous chapter, the aerodynamic noise from a typical 3MW wind turbine was predicted at various locations. From the numerical results, it is found that the sound pressure level of the wind turbine aerodynamic noise is rather low compared to other community noise sources. The A-weighted sound pressure level is about 40dBA at a distance of 400m from the wind turbine. Nevertheless, despite this low sound pressure level, several field studies have showed that wind turbine noise can annoy residents near wind farms [7, 8, 58]. They claim one of the reasons for this annoyance is that wind turbines generate a periodic swishing sound at a blade passing frequency.

In the vicinity of a wind turbine, the swishing sound can be easily heard due to the rotational motion of wind turbine blades. As an observer becomes more distant from the wind turbine, this swishing sound is difficult to perceive. However, van den Berg [7, 8] reported that at night a periodic thumping sound is heard at distances of more than 1km from the wind farm although in

daytime the wind turbine noise is only perceivable within a few hundred meters. He maintained that this thumping sound has a more impulsive character compared than the reported swishing sounds. These swishing or thumping sounds are called the amplitude modulation of wind turbine noise. Figure 3.1 presents the A-weighted sound pressure level of wind turbine noise observed by van den Berg when the noise contains the amplitude modulation [7].

Since van den Berg first reported the thumping sound, several other researchers have also investigated the amplitude modulation of wind turbine noise. Di Napoli carried out noise measurement for a wind turbine in Finland, finding that the amplitude modulation is observed at a distance of 530m [9]. Larsson and Öhlund measured wind turbine noise at two wind farms for one year in Sweden and observed the amplitude modulation depending on propagation paths and meteorological conditions [10].

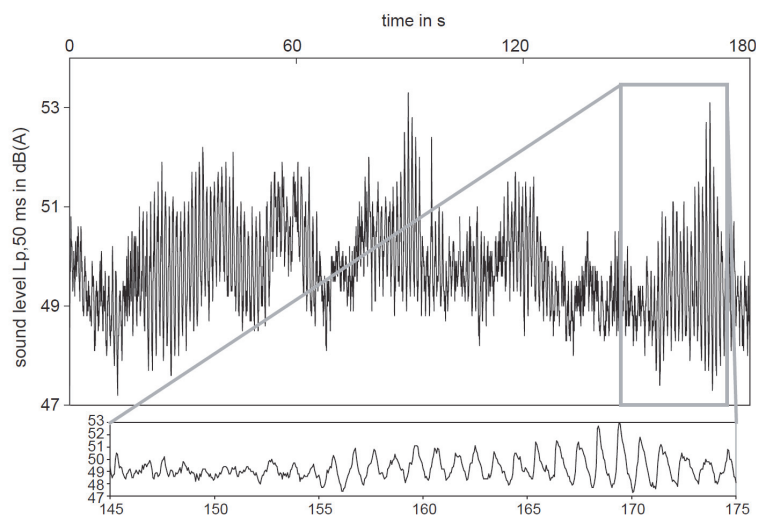


Fig. 3.1. The amplitude modulation of wind turbine noise observed by van den Berg [7]

Several previous studies [7, 58] have argued that the amplitude modulation of wind turbine noise may increase noise annoyance. Pedersen and Persson Waye [58] performed a field study to evaluate the prevalence of annoyance caused by wind turbine noise. The result of their study suggested that wind turbine noise is more annoying than other community noise sources with the same A-weighted sound level. They mentioned that one of the reasons for this result could be the presence of the amplitude modulation of wind turbine noise.

Indeed, amplitude modulated sound is generally known to be more annoying than unmodulated sound. Kantarelis and Walker examined the source of difference between the annoyance of diesel and electric train noises [59]. They suggested that the amplitude modulation in diesel engine noise is the reason for the extra annoyance. The annoyance caused by the diesel train noise decreased as the modulation depth was reduced from 13dB to 5dB. Furthermore, Bradley investigated the influence of amplitude modulated low-frequency sounds from heating, ventilation, and air conditioning (HVAC) systems on annoyance, finding that annoyance is correlated with both the sound pressure level and the amplitude modulation of the noise from HVAC systems [60]. In particular, for wind turbine noise, Lee et al. investigated the relation between noise annoyance and the amplitude modulation of wind turbine noise [61]. They performed a listening test to examine the annoyance caused by the amplitude modulation of wind turbine noise. The experimental results suggested that the swishing sound could cause additional annoyance. Thus, in order to evaluate the effect of wind turbine noise on people, there needs to be a better understanding of the characteristics of the amplitude modulation in wind turbine noise.

3.1.2 Literature review

Although several studies have investigated the characteristics of the amplitude modulation by measuring wind turbine noise, but the cause of the amplitude modulation is still not clearly known [7, 62, 63]. Dunbabin performed an experiment to record noise from a 400kW wind turbine [62]. From the noise measurement taken at a distance of 30m from the wind turbine, it was argued that the amplitude modulation is dominant in the 1~2kHz frequency bands, and that the modulation has no relation to the blade passing the tower. Van den Berg maintained that the thumping sound is due to the stable atmospheric conditions at night because a periodic thumping sound is heard especially at night at long distances from a wind farm [7, 8].

Notably, Oerlemans et al. conducted acoustic measurements on a wind turbine using a microphone array in order to characterize the noise sources of the wind turbine [63]. The wind turbine tested had a rotor diameter of 58m, and the measurements were carried out at a distance roughly equal to one rotor diameter. The results of the study showed that convective amplification and trailing edge noise directivity are the main causes of the periodic swishing sound. However, because the noise measurements were performed only in the vicinity of the wind turbine, this study could not confirm whether the source of the thumping sounds, i.e. the amplitude modulation of wind turbine noise which is heard at long distances from wind turbines, is convective amplification and trailing edge noise directivity or stable atmospheric conditions.

Recently, Laratro et al. discussed possible reasons that have been suggested to explain the amplitude modulation of wind turbine noise [64]. These include the sound directivity of trailing edge noise, turbulence ingestion noise due to atmospheric turbulence or the wake of upstream

turbines, dynamic stall noise, and blade vortex interaction noise. In particular, they claimed that turbulence ingestion and dynamic stall due to the wake of upstream turbines can be a source of the thumping sound. However, an experimental or numerical study is further needed to verify this hypothesis.

To date, a number of studies have numerically calculated aerodynamic noise from wind turbines as introduced in the previous chapter [6, 27, 29, 32-36, 65]. However, only a few studies have predicted the amplitude modulation of wind turbine noise. Oerlemans and Schepers [32] calculated the swish amplitude of wind turbine noise using a semi-empirical model proposed by Brooks, Pope, and Marcolini [2]. They claimed that in the crosswind direction, wind turbine noise retains the amplitude modulation even at long distances. However, it is still not known why the perceived sounds are different and how they differ depending on observer locations.

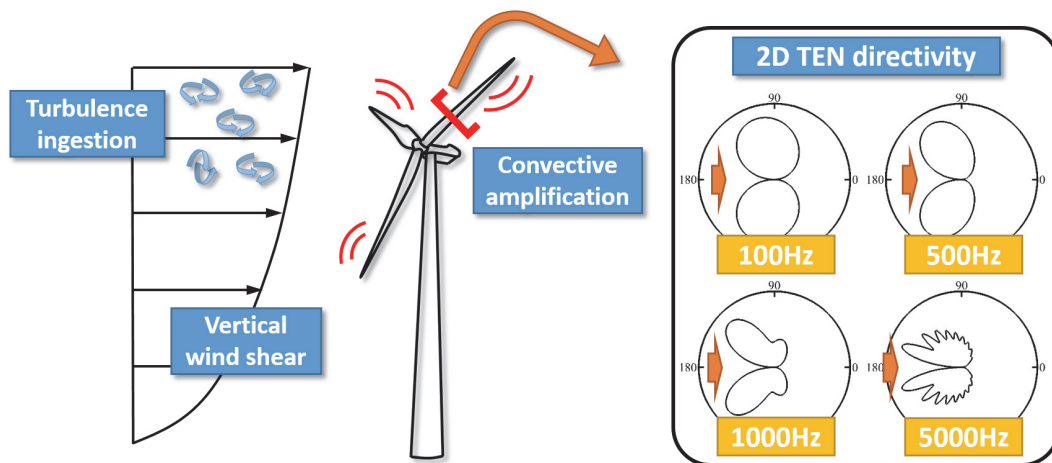


Fig. 3.2. Possible cause of the amplitude modulation of wind turbine noise at long distances

3.1.3 Research objective

In this chapter, to compare the acoustical characteristics of wind turbine noise depending on the observer location, the aerodynamic noise from a wind turbine is numerically modeled in the time domain [24]. Time domain simulation is an appropriate method to model the amplitude modulation of wind turbine noise, because it can not only give good predictions about the temporal variation of wind turbine noise, but allows us to actually hear the amplitude modulation of the predicted signals. This helps us to better understand the acoustical characteristics of the wind turbine noise with respect to the distance and direction from the wind turbine. From this understanding, it will be investigated why the thumping sound is heard at long distances from a wind turbine. To examine the main cause of the thumping sound among the possible reasons, the numerical simulations are carried out for four calculation cases.

A simplified analytic models proposed by Amiet [20, 21] and Amiet [30] are used to obtain the unsteady pressure on the blade surfaces due to the trailing edge noise and the turbulence ingestion noise, respectively. The wall-point pressure spectrum used in the trailing edge noise model is predicted by Rozenberg's APG model with XFOIL, which is introduced in the previous chapter. The far field noise due to the unsteady surface pressure is then calculated using the Ffowcs Williams and Hawking equation [4].

In the following section, the two noise models for the unsteady pressure on blade surfaces is presented. Formulation 1A [66, 67], one of the integral forms of the Ffowcs Williams and Hawking's equation, is introduced for the numerical calculation of acoustic pressure. Furthermore, validation of the numerical prediction model is carried out using experimental data from Brooks and Hodgson [55] and Paterson and Amiet [68]. The sound directivity for

the two noise sources is also examined by looking at the same validation test cases. In Chapter 3.3, the numerical prediction model for an isolated airfoil is extended to predict rotor broadband noise, using a strip theory approach. After a brief introduction of the wind turbine model and the calculation cases, the aerodynamic noise from the wind turbine is calculated at a number of observer locations. Using these results, the characteristics of the amplitude modulation of wind turbine noise are discussed in Chapter 3.4.

3.2 Numerical method

3.2.1 Trailing edge noise model

The model proposed by Amiet [20, 21] is again used for the modeling of the trailing edge noise. In order to solve Eq. (2.4), it is necessary to integrate in two wavenumber dimensions. However, because the surface pressure spectrum in the boundary layer is at its strongest within the convective ridge centered on $k_c = \omega/U_c$, $k_2 = 0$ [47], it is possible to simplify the equation into

$$\Delta p_t(y_1, t) \approx \left[\Delta p_t(y_1, y_2, t) \right]_{k_c = \frac{\omega}{U_c}, k_2 = 0}, \quad (3.1)$$

where U_c is a convection velocity. The convection velocity is again assumed to be constant, and is set to $U_c = 0.7U$. Thus, Eq. (3.1) becomes

$$\Delta p_t(y_1, t) = \int_{-\infty}^{\infty} p_0 e^{-ik_c(y_1 - U_c t)} \left\{ e^{\varepsilon k_c y_1} - 1 + (1+i) E^* \left[-y_1 \{k_c + \mu(1+M)\} \right] \right\} dk_c. \quad (3.2)$$

Equation (3.2) is numerically integrated by the method described in earlier work [69]. This is given by

$$\Delta p(y_1, t) \approx -4\pi \sum_{n=1}^N A_n e^{-i\{k_{c,n}(y_1 - U_c t) + \psi_n\}} \left[e^{\varepsilon k_{c,n} y_1} - 1 + (1+i) E^* \left[-y_1 \{k_{c,n} + \mu(1+M)\} \right] \right], \quad (3.3)$$

where $A_n = \sqrt{\Phi_{qq}(k_{c,n}, 0, k_c U_c) \Delta k_c}$, ψ_n are independent random variables uniformly distributed at $[0, 2\pi]$, $k_{c,n}$ are the streamwise convective wavenumbers, and N is the number of computing wavenumbers [69]. The complex conjugate of the Fresnel integral in Eq. (3.3) can be numerically calculated in the way described in [70]. Hence, the real value of Eq. (3.3)

is the fluctuating pressure on the surface, and this is used as the input for the calculation of the far-field acoustic pressure.

The wall-pressure wavenumber-frequency spectrum, Φ_{qq} is modeled in the same manner described in Chapter 2.2.1. The spectrum is modeled as Eq. (2.6), and the wall-point pressure frequency spectrum is predicted by Rozenberg's APG model.

3.2.2 Turbulence ingestion noise model

For the modeling of the turbulence ingestion noise, an analytic model proposed by Amiet is used [30]. Figure 3.3 presents a schematic of the turbulence ingestion noise model problem for a flat-plate in rectilinear motion. The plate is placed in the plane $x_3 = 0$, and moves with velocity U in the negative x_1 -direction. The leading edge of the plate is aligned with the x_2 -axis, and the origin of the Cartesian coordinate system is at the center of the leading edge. Starting from the convected wave equation for the perturbation potential [47, 71] and using the solution of Schwartzschild [71, 72], the surface pressure jump due to turbulent inflow at point \mathbf{y} at time t is described as

$$\Delta p_a(y_1, y_2, t) = 2\rho_0 U \int_{-\infty}^{\infty} \int_{-\infty}^{\infty} \tilde{w}(k_1, k_2) g(y_1, k_1, k_2) e^{i(k_1 U t + k_2 y_2)} dk_1 dk_2. \quad (3.4)$$

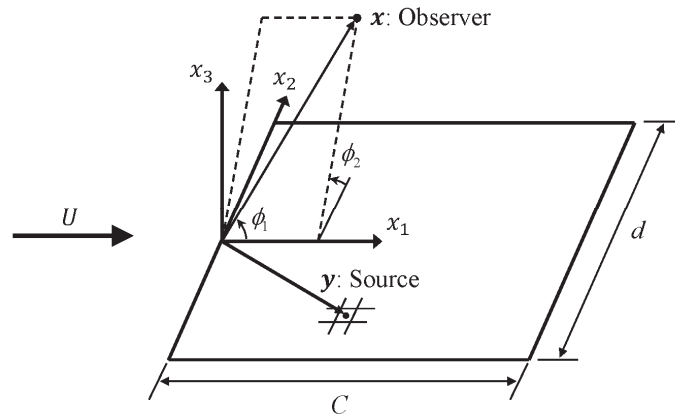


Fig. 3.3. Schematic of the turbulence ingestion noise model problem

In the same manner previously described in Chapter 3.2.1, the integration with respect to k_2 is neglected, and then Eq. (3.4) becomes

$$\Delta p_a(y_1, t) = 2\pi\rho_0 U \int_{-\infty}^{\infty} \tilde{w}(k_1, 0) g(y_1, k_1, 0) e^{ik_1 U t} dk_1. \quad (3.5)$$

Again, Eq. (3.5) is numerically integrated by the method described in a previous study [73], which is given by

$$\Delta p_a(y_1, t) \approx 4\pi\rho_0 U \sum_{n=1}^N A_{n,0} g(y_1, k_{1,n}, 0) e^{i(k_{1,n} U t + \psi_n)}, \quad (3.6)$$

where $A_{n,0} = \sqrt{S_{ww}(k_{1,n}, 0)} \Delta k_1$, ψ_n are independent random variables uniformly distributed at $[0, 2\pi]$, $k_{1,n}$ are the streamwise wavenumbers, and N is the number of computing wavenumbers [73]. The transfer function $g(y_1, k_{1,n}, 0)$ is selected as the first two terms of Adamczyk's solution, which can be used for $\mu > 0.4$ [74]. This is given by

$$g(y_1, k_{1,n}, 0) = (g_1 + g_2) e^{i\{2\mu_n(1-M)y_1/C + 4/\pi - \bar{k}_{1,n}\}}, \quad (3.7)$$

where

$$g_1(y_1, k_{1,n}) = \frac{1}{\sqrt{2\pi\bar{k}_{1,n}y_1(1+M)/C}},$$

$$g_2(y_1, k_{1,n}) = \frac{-1 + (1+i)E^*[4\mu_n(1-y_1/C)]}{\sqrt{2\pi\bar{k}_{1,n}(1+M)}}.$$

3.2.3 Acoustic formulation

The Ffowcs Williams and Hawkings equation [4] is used to calculate the sound radiated by wind turbine blades. This equation determines the far-field acoustic pressure generated by solid bodies in arbitrary motion. According to [4], the far-field acoustic pressure, $p'(\mathbf{x}, t)$ is expressed in a differential form as

$$\square^2 p'(\mathbf{x}, t) = \frac{\partial}{\partial t} [\rho_0 v_n \delta(\mathbf{g})] - \frac{\partial}{\partial x_i} [p_{ij} n_i \delta(\mathbf{g})] + \frac{\partial^2}{\partial x_i \partial x_j} [H(\mathbf{g}) T_{ij}], \quad (3.8)$$

where $\square^2 \equiv (1/c_0^2) \partial^2 / \partial t^2 - \nabla^2$ is the d'Alembertian operator, c_0 is the ambient speed of sound, ρ_0 is the ambient density, and the symbols v_n , p_{ij} , and T_{ij} in each bracket are the normal velocity on the surface, the local gage surface pressure, and Lighthill stress tensor, respectively. In the above equation, \mathbf{g} is defined as $\mathbf{g} = 0$ and $\nabla \mathbf{g} = \mathbf{n}$ on the solid surface, where \mathbf{n} is the unit outward normal vector from the surface.

The three terms on the right of Eq. (3.8) are the sources of the sound, and they are known as the thickness, loading, and quadrupole source terms, respectively. Among the noise sources, the trailing edge noise mechanism when the flow is at low Mach number is known to be closely associated with the loading source term [69]. Thus, this study neglects the thickness and quadrupole terms, and we only consider the loading source in Eq. (3.8).

Formulation 1A of Farassat is used to numerically calculate the far-field acoustic pressure in Eq. (3.8) [66, 67]. Formulation 1A is one of the integral forms of the Ffowcs Williams and Hawkings equation, which is well suited for numerical calculations. By using this equation, the far-field acoustic pressure in Eq. (3.8) can be expressed as

$$\begin{aligned}
4\pi p'(\mathbf{x}, t) = & \frac{1}{c_0} \int_{\mathbf{g}=0} \left[\frac{\dot{p}_i \hat{r}_i}{r(1-M_r)^2} \right]_{\text{ret}} dS + \int_{\mathbf{g}=0} \left[\frac{p_r - p_i M_i}{r^2(1-M_r)^2} \right]_{\text{ret}} dS \\
& + \frac{1}{c_0} \int_{\mathbf{g}=0} \left[\frac{p_r (r\dot{M}_i \hat{r}_i + c_0 M_r - c_0 M^2)}{r^2(1-M_r)^3} \right]_{\text{ret}} dS, \quad (3.9)
\end{aligned}$$

where \mathbf{x} and \mathbf{y} are the observer and the source locations, respectively; $r = |\mathbf{x} - \mathbf{y}|$ is the radiation distance; dS is an element of surface area of blade; and $\hat{\mathbf{r}} = (\mathbf{x} - \mathbf{y})/|\mathbf{x} - \mathbf{y}|$ is the unit radiation vector. The subscript r indicates a component in the radiation direction, and the dots represent a derivative with respect to the source time. The square brackets $[\]_{\text{ret}}$ indicate that the integration is evaluated at a retarded time. The surface pressure vector, \mathbf{p} in Eq. (3.9) is the real value of $\Delta p(y_1, \tau)$ in Eqs. (3.3) and (3.6) in the normal direction from the surface.

3.2.4 Validation

3.2.4.1 Trailing edge noise

Before rotor noise predictions, the validation of the numerical prediction method for a two-dimensional flow is carried out via a comparison with the result of the experiment by Brooks and Hodgson [55]. They performed extensive experiments to measure trailing edge noise from NACA0012 airfoil models. The case of interest here is the tripped boundary layer case of the 2D sharp trailing edge model at a zero angle of attack. The span and the chord length of this airfoil model is 0.46m and 0.6096m, respectively. The inflow velocity used in the validation case is 69.5m/s.

For the numerical prediction of the trailing edge noise, the airfoil is modeled as a flat-plate grid which has the same span and chord length as the experiment model. The rectangular surface grid is uniformly applied not only in the spanwise direction, but also in the chordwise direction. The longest chordwise grid is sufficiently small to resolve the highest frequency, i.e. the maximum grid length is smaller than $\lambda_N/10$. The maximum frequency for the acoustic prediction is set to $f_N = 10\text{kHz}$. The frequency range is divided into $N = 1000$ partitions for numerical integration. Consequently, the bandwidth and the minimum frequency become $f_1 = \Delta f = 10\text{Hz}$. The wall-point pressure frequency spectrum is calculated using XFOIL in the same way as Chapter 2.3.1. The calculation is performed during one period of the minimum frequency, i.e., $T = 0.1$.

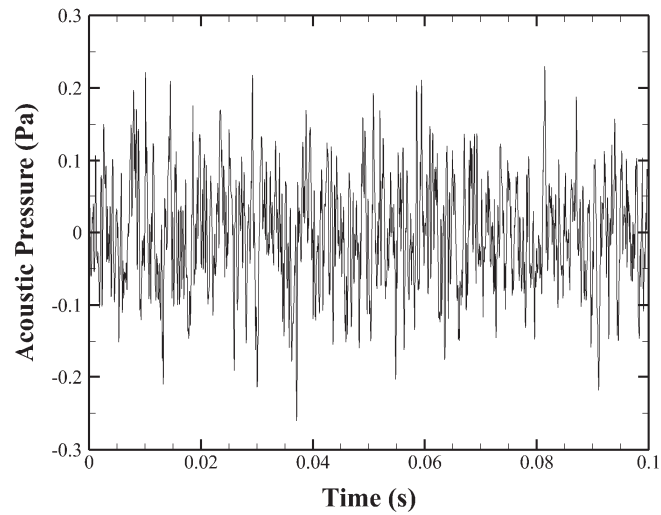


Fig. 3.4. Predicted time domain signal of trailing edge noise

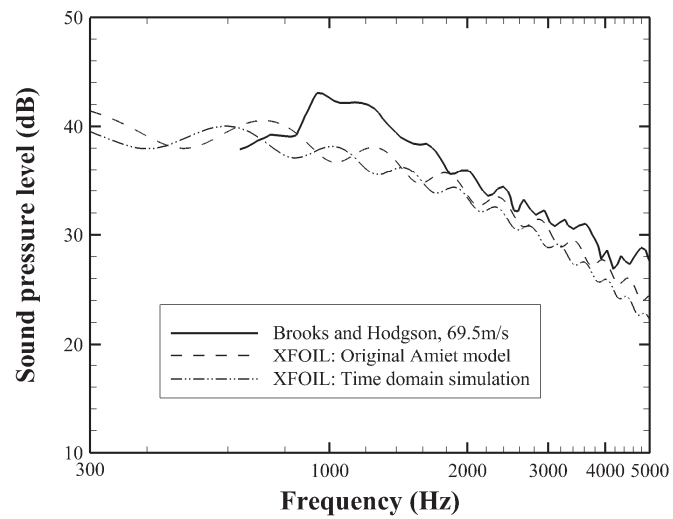


Fig. 3.5. Comparison of 1/3 octave band spectrum between experimental data and numerical prediction in the frequency and time domain

Figure 3.4 shows the predicted acoustic pressure for an observation position at $x = (0, 0, 1.22)$. Figure 3.5 compares the 1/3 octave band spectra between the experimental data and the numerical results calculated in the frequency and time domain. It is seen that the sound pressure level predicted by time domain simulation agrees well with those obtained by original Amiet's frequency domain model.

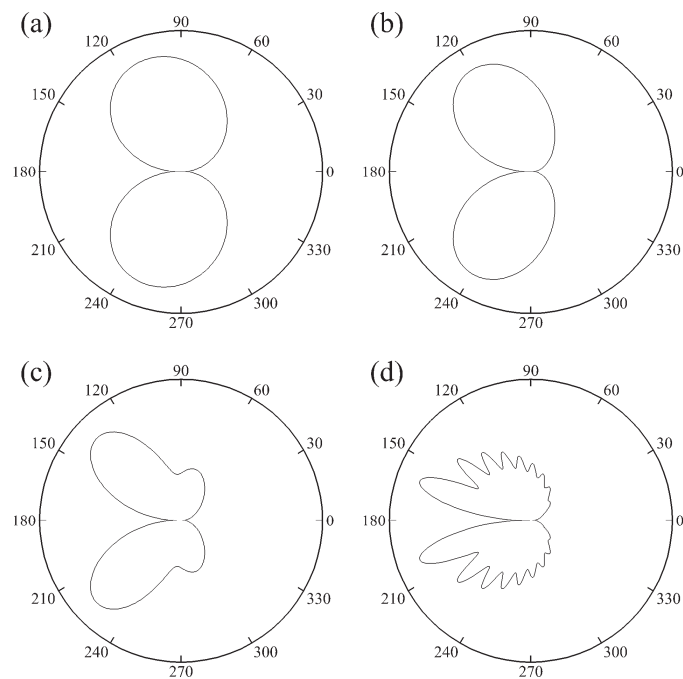


Fig. 3.6. Streamwise trailing edge noise directivity in the mid-span plane for frequencies of (a) $f = 100\text{Hz}$, (b) $f = 500\text{Hz}$, (c) $f = 1000\text{Hz}$, and (d) $f = 5000\text{Hz}$

As the amplitude modulation of wind turbine noise seems to be produced in the main part by the trailing edge noise directivity, it is important to properly predict this sound directivity for modeling the amplitude modulation. Hence, this study also investigates the sound directivity of the model airfoil. The acoustic pressure is predicted in the same way as the previous validation, except the observer location is different. Unlike the validation case, the noise is calculated in the range from $\phi_1 = 0^\circ$ to 360° in step of 1° . The radiation distance from the trailing edge is the same as the validation case, i.e. $r = 1.22\text{m}$. Next, the narrowband spectra for each acoustic pressure are obtained by applying a fast Fourier transform to the acoustic signals. Each frequency component is then extracted at each observer location. The directivity is determined by the root-mean-square pressure of the narrowband spectrum.

Figure 3.6 shows the streamwise noise directivity for the frequency bands at 100, 500, 1000, and 5000Hz. Each curve is normalized by its maximum value. For low frequency bands, the directivity appears to be similar to a dipole source. On the other hand, as the frequency increases, multiple lobes emerge and the directivity becomes similar to a cardioid pattern. This trend is identical to those observed in previous studies [75].

3.2.4.2 Turbulence ingestion noise

The validation of the numerical method for the prediction of turbulence ingestion noise is also performed with a comparison with the experimental result of Paterson and Amiet [68]. A comparison is made with the case of the 2D NACA0012 airfoil at a zero angle of attack. The span and the chord length of this airfoil model is 0.53m and 0.23m, respectively. The inflow velocities used in the validation case is 165m/s.

The acoustic pressure is predicted in the same way as the previous section although an observation position is change to $x = (0.115, 0, 2.25)$. However, to correct shear layer effect discussed in Ref. [76], the amplitude and the microphone position are corrected by the methods proposed in Ref. [68]. Detailed descriptions of the correction procedure are explained in the literature [73], and they will not be discussed here.

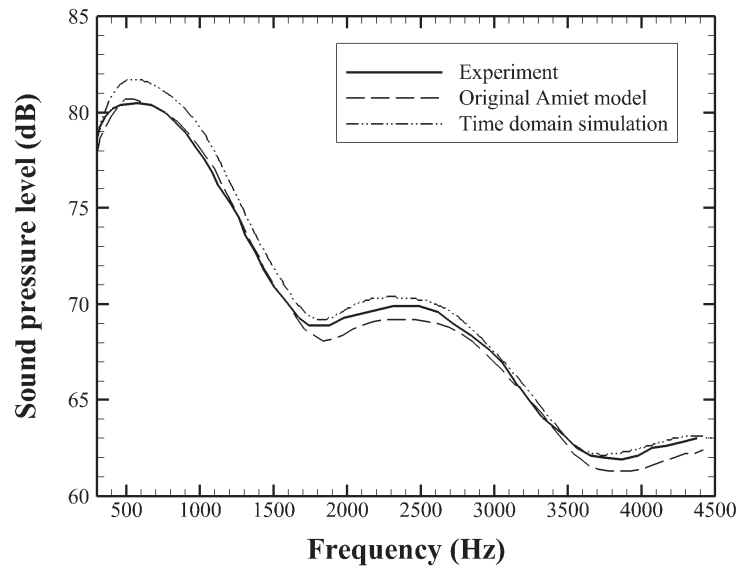


Fig. 3.7. Comparison of 1/3 octave band spectrum between experimental data and numerical prediction in the frequency and time domain

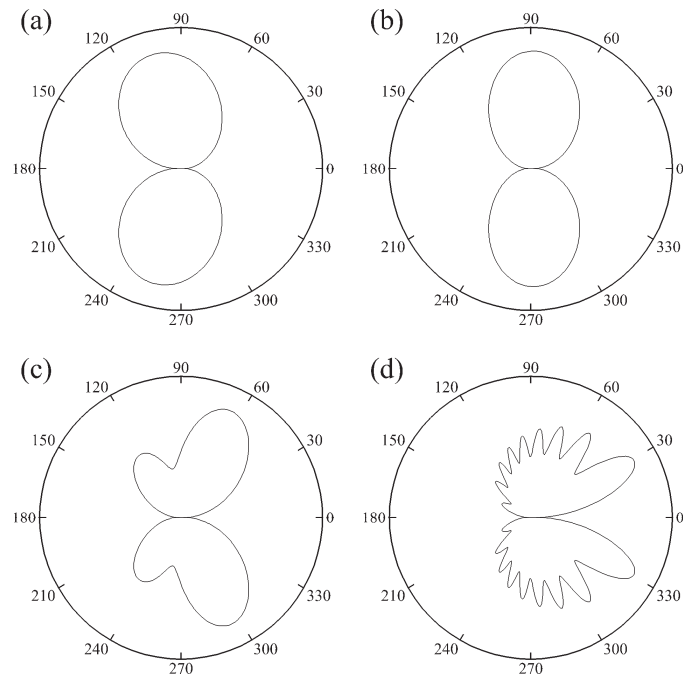


Fig. 3.8. Streamwise turbulence ingestion noise directivity in the mid-span plane for frequencies of (a) $f = 100\text{Hz}$, (b) $f = 500\text{Hz}$, (c) $f = 1000\text{Hz}$, and (d) $f = 5000\text{Hz}$

Again, a comparison is made between the experimental data and the numerical results calculated in the frequency and time domain, as shown in Fig. 3.7. The result shows that the difference of the sound pressure levels predicted by the time domain simulation and by the original Amiet's frequency domain model is less than about 1dB. Moreover, the streamwise directivity for the turbulence ingestion noise is also examined, as shown in Fig. 3.8. Frequency dependent directivity pattern of turbulence ingestion noise is similar to that of trailing edge noise. However, because the sound is mainly generated at the leading edge, the direction of the main lobe is inverted. This trend is identical to those observed in previous studies [73].

3.2.5. Calculation case

3.2.5.1 Rotor noise prediction

The wind turbine model used in the calculation is a 3MW three-blade horizontal axis wind turbine that has typical multi-MW wind turbine characteristics. This turbine is a pitch regulated, variable speed type with a rotor diameter of 91.6m and a hub height of 90m. In this study, noise is predicted at a wind speed of 14m/s at the hub height.

A strip theory approach is used to apply the two-dimensional noise model to the rotating blades. The blades are divided into 20 segments of equal lengths. Each segment is modeled as a flat-plate grid, as shown in Fig. 3.9. Because the blade span is very large compared to the turbulence correlation length in the spanwise direction, it is assumed that the fluctuating surface pressure has no correlation not only between the segments, but also between the blades. The inflow velocity and the effective angle of attack are assumed as uniform in each segment, and they are calculated by WINFAS. Various boundary layer parameters, which are necessary for the prediction of the wall-point pressure frequency spectrum, are obtained with XFOIL code.

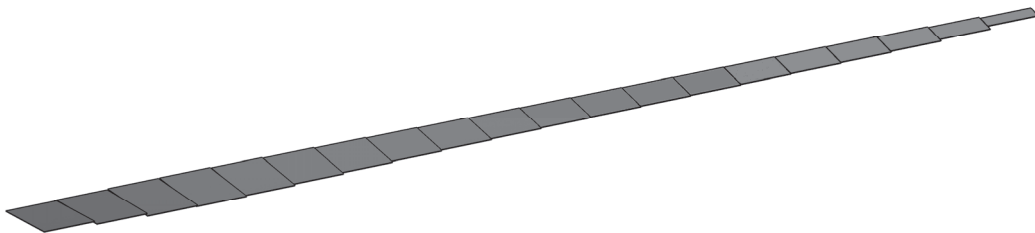


Fig. 3.9. Rectangular surface grids for modeling of the wind turbine blade

The calculations are performed for a duration of one-third of a rotation, i.e., $T = 1/f_{\text{BPF}}$. The maximum frequency and the frequency bandwidth are set to $f_N = 3\text{kHz}$ and $\Delta f = 10\text{Hz}$, respectively. The time step is set to $\Delta T = 0.16667\text{ms}$, which satisfies the Nyquist sampling criterion. Moreover, for the calculation of air absorption, it is assumed that the air temperature is 15°C , the relative humidity is 60% , and the air pressure is one standard atmosphere. The approximate attenuated sound levels are determined by the multiplication of the attenuation coefficients and the radiation distance in kilometers [77]; this is set as the distance between the center of the rotor hub and an observer location. The calculated acoustic signals are filtered by a finite impulse response filters with an arbitrary magnitude to apply the attenuated sound levels. In addition, acoustic reflections from the ground and acoustic refraction caused by wind and temperature gradients were not considered in this calculation.

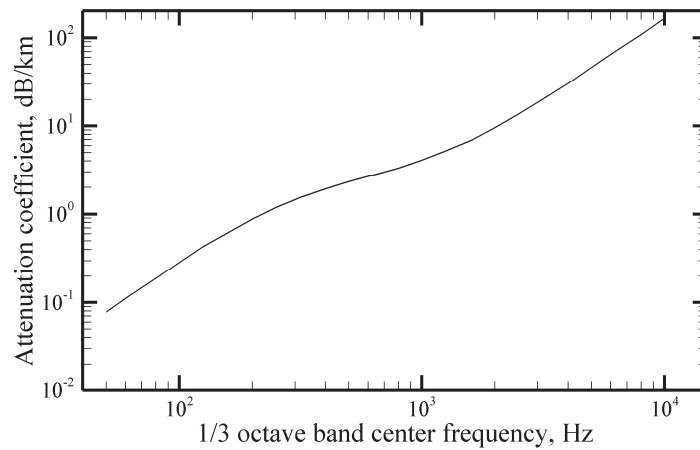


Fig. 3.10. Atmospheric-absorption attenuation coefficients when air temperature, relative humidity, and air pressure are 15°C , 60% , and one standard atmosphere, respectively

3.2.5.2 Calculation cases

A total of four cases are calculated to examine the main cause of amplitude modulation in wind turbine noise, as shown in Table 3.1. Case I defines when uniform inflow is ingested into the rotor disk. Because atmospheric turbulence does not exist, trailing edge noise is the only noise source, and turbulence ingestion noise is excluded in this case. This case will help to reveal the existence of the amplitude modulation of wind turbine noise at long distances.

Case II also calculates trailing edge noise only, but this case assumes that the rotor blades are stationary in motion. It is the wind turbine blades that rotate in a real case, but in this case it is assumed that the blades are stationary in motion even though the sectional inflow and effective angle of attack are the same as the real case. This case is performed to investigate the relative contribution of convective amplification and trailing edge noise directivity.

In Case III, the wind turbine noise is predicted when wind speed varies with height above the ground. In a real environment, the mean wind speed increases as the height increases. The velocity profile is typically influenced by a roughness length and atmospheric stability condition. The trailing edge noise from the wind turbine blades is calculated in two atmospheric conditions, which are a stable and an unstable conditions.

Furthermore, Case IV evaluates the effect of turbulence ingestion on the amplitude modulation of wind turbine noise. Because turbulence ingestion will introduce another noise source at the blade leading edge, this case calculates not only the trailing edge noise, but also the turbulence ingestion noise from the wind turbine blades. The results will be compared with that of Case I.

Table 3.1. Four calculation cases for the time domain simulation

	Trailing edge noise	Stationary in motion	Vertical wind shear	Turbulence ingestion noise
Case I	○	×	×	×
Case II	○	○	×	×
Case III	○	×	○	×
Case IV	○	×	×	○

3.3 Results

3.3.1 Case I—Uniform inflow

3.3.1.1 IEC 61400-11 reference position

The acoustic pressure due to trailing edge noise is predicted when the inflow is uniformly ingested into the rotor disk. First al all, the observer is assumed to be located at the reference positions according to the IEC 61400-11 standard, $R = 135.8\text{m}$ [56]. Atmospheric attenuation is not considered in this calculation as the observer is close to the wind turbine. For this case, the maximum frequency of the acoustic pressure is set to 5kHz for the demonstration purpose. The predicted acoustic signal is shown in Fig. 3.11. The acoustic signal are also presented as an audio clip at Aud. 3.1. It can be seen that the acoustic signal is amplitude modulated at a blade passing frequency of 0.785Hz.

Aud. 3.1. <https://drive.google.com/folderview?id=0B1dAuFX-upUweUoySUFnbGJGSEk&usp=sharing>

This audio is an acoustic signal, which is predicted at the reference positions according to IEC 61400-11. The calculations are performed for a duration of one rotation. This is a file of type “wav”.

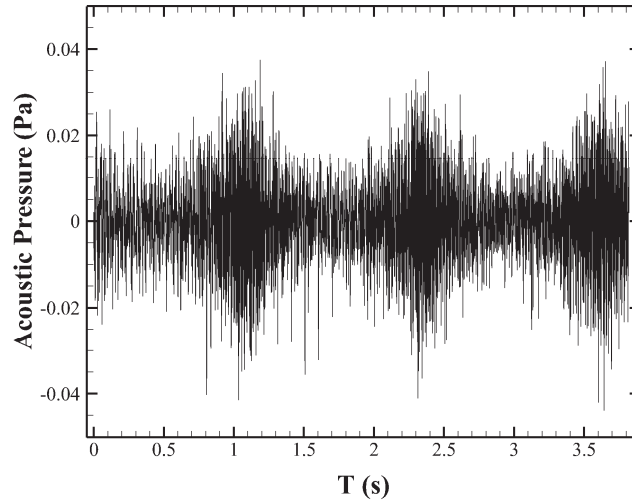


Fig. 3.11. Predicted acoustic pressure at the IEC 61400-11 reference position

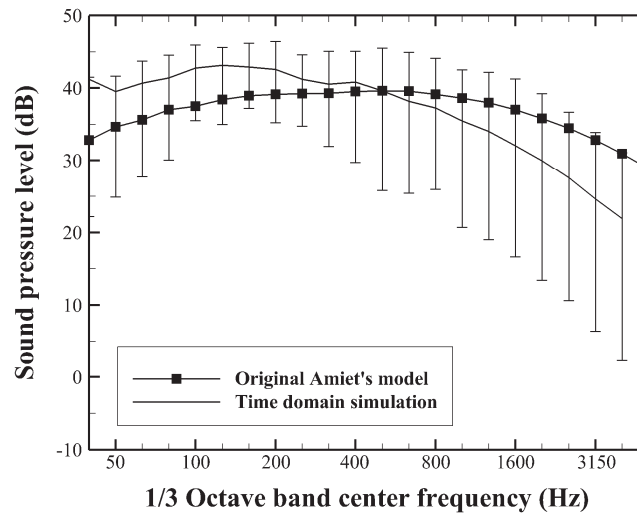


Fig. 3.12. Comparison of 1/3 octave band spectra between original Amiet's model and time domain simulation. Upper and lower bars represent the maximum and the minimum sound pressure levels of L_{FAST} in each frequency spectrum. It should be noted that the maximum and minimum sound pressure levels in each frequency spectrum do not occur at the same time.

Moreover, one-third octave band frequency spectrum is calculated to analyze the predicted signal in the frequency domain. Figure 3.12 compares the one-third octave band spectra calculated from the time domain simulation and the original Amiet's model. It can be seen that the sound pressure level obtained from the time domain simulation is slightly higher than that from the original Amiet's model in low frequency region, while the time domain simulation severely under-predict sound pressure levels in high frequencies. However, because at long distances from wind turbines most of the high-frequency noise is attenuated due to atmospheric attenuation, these large discrepancies may not be a serious problem to assess the wind turbine noise.

In addition, the modulation depth, which is defined as the difference between the maximum and the minimum sound pressure levels of L_{FAST} in each frequency spectrum, is also shown in Fig. 3.12. It is found that the amplitude modulation exist in all frequency bands and the modulation depth increases as the frequency increases. This is due to the frequency dependency of the trailing edge noise directivity; the directionality of trailing edge noise increases as the frequency increases, as previously shown in Fig. 3.6.

3.3.1.2 Noise characteristics with respect to distance and direction

The acoustic signals are calculated at distances of $R=135.8\text{m}$, 250m , 500m , and 1000m from the wind turbine at azimuthal intervals of $\Delta\Psi=15^\circ$. The sound pressure level and the modulation depth of the predicted signals are presented in Fig. 3.13. The figure shows that the A-weighted sound pressure level reaches its maximum in the upwind and downwind directions, while it reaches its minimum in the crosswind direction. On the other hand, the modulation

depth is greatest in the crosswind direction, whereas it is small in the upwind and downwind directions.

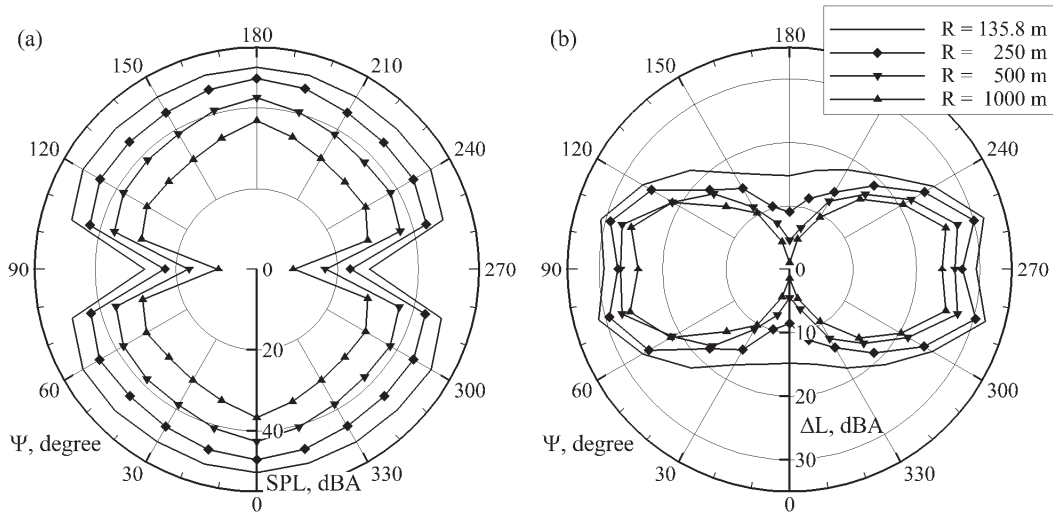


Fig. 3.13. (a) The sound pressure level and (b) the modulation depth of the predicted acoustic signals. The azimuth angle, Ψ is defined as the angle between the rotor axis and the line connecting the wind turbine to the observer. The wind is blowing from the $\Psi = 180^\circ$ direction. The modulation depth is defined as the difference between L_{AFmax} and L_{AFmin} .

Furthermore, the acoustical characteristics of the amplitude modulation in wind turbine noise are evaluated in terms of observer locations by comparing a part of the predicted signals presented at Aud. 3.2 and 3.3. In the vicinity of the wind turbine (Aud. 3.2), the amplitude modulation is detected from all azimuthal directions. These sounds are similar to a typical swishing sound. On the other hand, at long distances from the wind turbine (Aud. 3.3), the amplitude modulation is hardly perceived in the upwind, downwind, and crosswind directions; the amplitude modulation disappears in the upwind and downwind directions, and the noise level is too low to be heard in the crosswind direction. Nevertheless, even at long distances the

amplitude modulation is still audible in other directions. In addition, these sounds are no longer similar to the swishing sound. They are low-frequency amplitude-modulated sounds, as most of the high-frequency noise is attenuated due to air absorption.

Aud. 3.2. <https://drive.google.com/folderview?id=0B1dAuFX-upUweUoySUFnbGJGSEk&usp=sharing>

This audio is the sum of 13 acoustic signals, which are predicted at a distance of $R = 135.8\text{m}$ with an azimuth angle ranging from $\Psi = 0^\circ$ to $\Psi = 180^\circ$ at intervals of 15° . Each signal repeats three times, and there is an interval of one second between different signals. This is a file of type “wav”.

Aud. 3.3. <https://drive.google.com/folderview?id=0B1dAuFX-upUweUoySUFnbGJGSEk&usp=sharing>

This audio is the sum of 13 acoustic signals, which are predicted at a distance of $R = 1000\text{m}$ with an azimuth angle ranging from $\Psi = 0^\circ$ to $\Psi = 180^\circ$ at intervals of 15° . Each signal repeats three times, and there is an interval of one second between different signals. This is a file of type “wav”.

These characteristics can also be confirmed as one-third octave band frequency spectra. Figure 3.14 presents the one-third octave band frequency spectra of the sound pressure level and the modulation depth predicted at distances of $R = 135.8\text{m}$ and 1000m with azimuth angles of $\Psi = 0^\circ$ and 60° . In the vicinity of the wind turbine (Fig. 3.14(a)), the modulation depth is large in downwind and crosswind directions. However, at long distances from the wind turbine (Fig. 3.14(b)), the modulation depth becomes small in downwind direction, while the strength of the amplitude modulation is still maintained in crosswind direction.

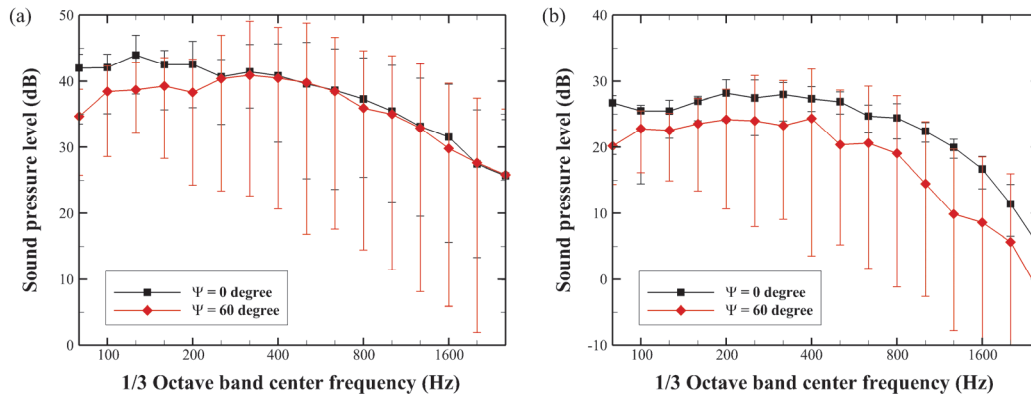


Fig. 3.14. 1/3 octave band frequency spectra of the sound pressure level and the modulation depth predicted at distances of (a) $R = 135.8\text{m}$ and (b) $R = 1000\text{m}$

3.3.1.3 Noise source distribution

The noise source distribution on the rotor disk is calculated to examine how the amplitude modulation in wind turbine noise is generated depending on the observer location. First of all, the acoustic pressure generated by each segment is calculated individually during the one-third of a rotation period. Because each three-blade was divided into 20 segments, a total of 60 acoustic signals are recorded. Moreover, during the calculation, the positions of all 60 segments are also recorded at each time step. It is assumed that the sound from the segments is generated at the center point of the segments. Each acoustic signal and the corresponding position records are then averaged over a time interval of one-twelfth of the total period. Consequently, the average level is the sound pressure level due to a segment during the set interval, and the corresponding average position is the location where the sound is generated.

The source distributions of different observer locations are compared in Fig. 3.15. The asymmetry of the source distribution along the azimuthal direction is clearly apparent in the

figures. This asymmetry is the cause of the amplitude modulation. The red contours in the figures indicate the regions at which the swishing sound is generated. The locations and the shapes of these regions are dependent on the observer position. These regions correspond to the positions where the blade approaches the observer.

The results indicate that the asymmetric shapes are different with respect to the distance and direction from the wind turbine. In the downwind direction ($\Psi = 0^\circ$), the asymmetry of the source distribution along the azimuthal direction gradually disappears as the distance increases. On the other hand, the strength of this asymmetry remains the same in the $\Psi = \pm 60^\circ$ directions, or it slowly decreases but does not disappear in the $\Psi = \pm 30^\circ$ directions. Note that the locations on the rotor where the maximum sound levels are generated vary as the distance to the observer increases. In the direction where the blade passed downward ($0^\circ < \Psi < 180^\circ$), this location rises to the top of the rotor disk as the distance increases. On the other hand, in the direction where the blade passed upward ($180^\circ < \Psi < 360^\circ$), this location moves slightly towards the bottom of the rotor disk as the distance increases.

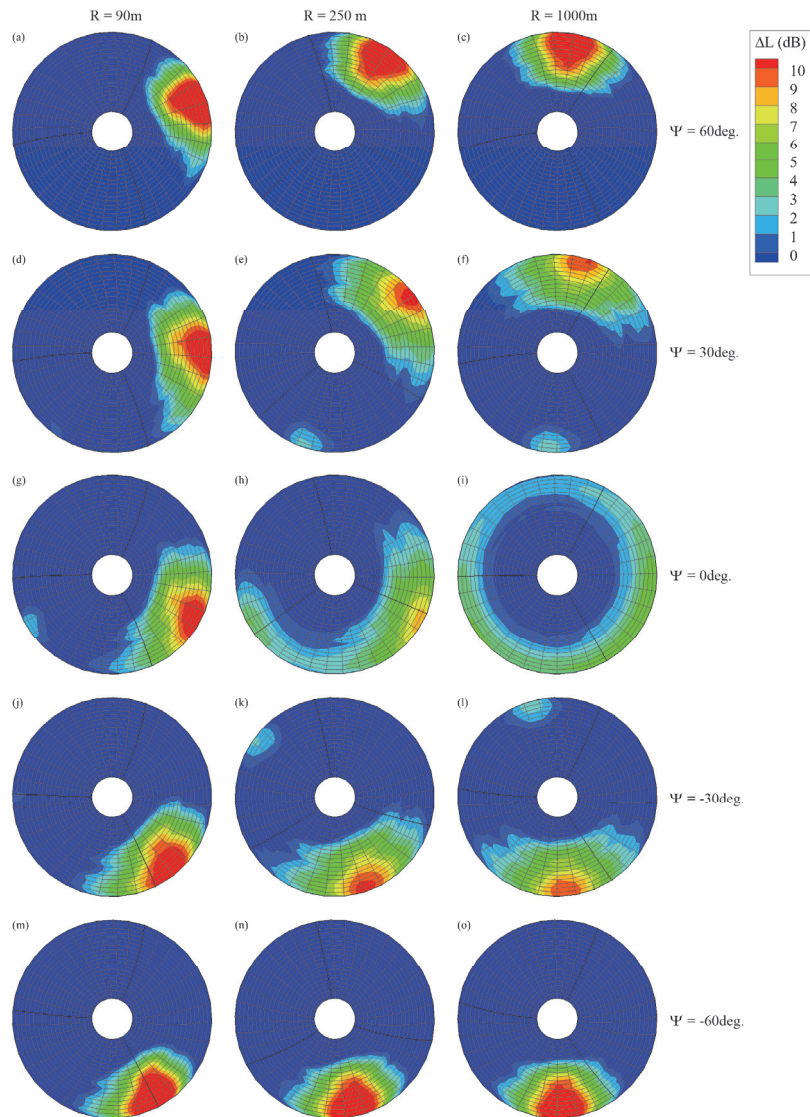


Fig. 3.15. Level difference between the calculated source distribution and the average sound pressure level of the rotor disk. The source distributions are calculated at three distances in five directions. For each source distribution, the average level of the total segment for the overall time is subtracted from the sound pressure level distribution on the rotor disk. This makes it possible to compare source distributions whose overall sound levels are different.

3.3.1.4 Noise index for the amplitude modulation of wind turbine noise

As we heard from the previous section, wind turbine aerodynamic noise is inherently amplitude modulated sound. Because the amplitude modulated sound is easily perceived and may increase noise annoyance, a noise index for wind turbine noise should reflect the strength of the amplitude modulation as well as the sound pressure level. However, A-weighted sound pressure level (L_{Aeq}) cannot properly consider the amplitude modulation characteristics. For example, when we hear the predicted sound at a distance of 1km (Aud. 3.3), the sound in the $\Psi = \pm 60^\circ$ directions seem more distinct than that in the downwind direction. Nevertheless, the A-weighted sound pressure level in the downwind direction is higher than that in the $\Psi = \pm 60^\circ$ directions.

Motivated by this limitation, a listening test was carried out to find a noise index that is correlated with annoyance caused by wind turbine noise [78]. The stimuli are generated by the time domain simulation method described in this paper. L_{Aeq} , loudness, fluctuation strength, and L_{AFmax} are the candidates for the possible noise index. Details test procedure are explained in Ref. [78] and will not be described here. The results of the listening test showed that L_{AFmax} is the most correlated with the level of noise annoyance for the amplitude modulated wind turbine noise, as shown in Fig. 3.16. This result proposes that the level of noise annoyance can be well explained by the maximum noise level, rather than by the average noise level.

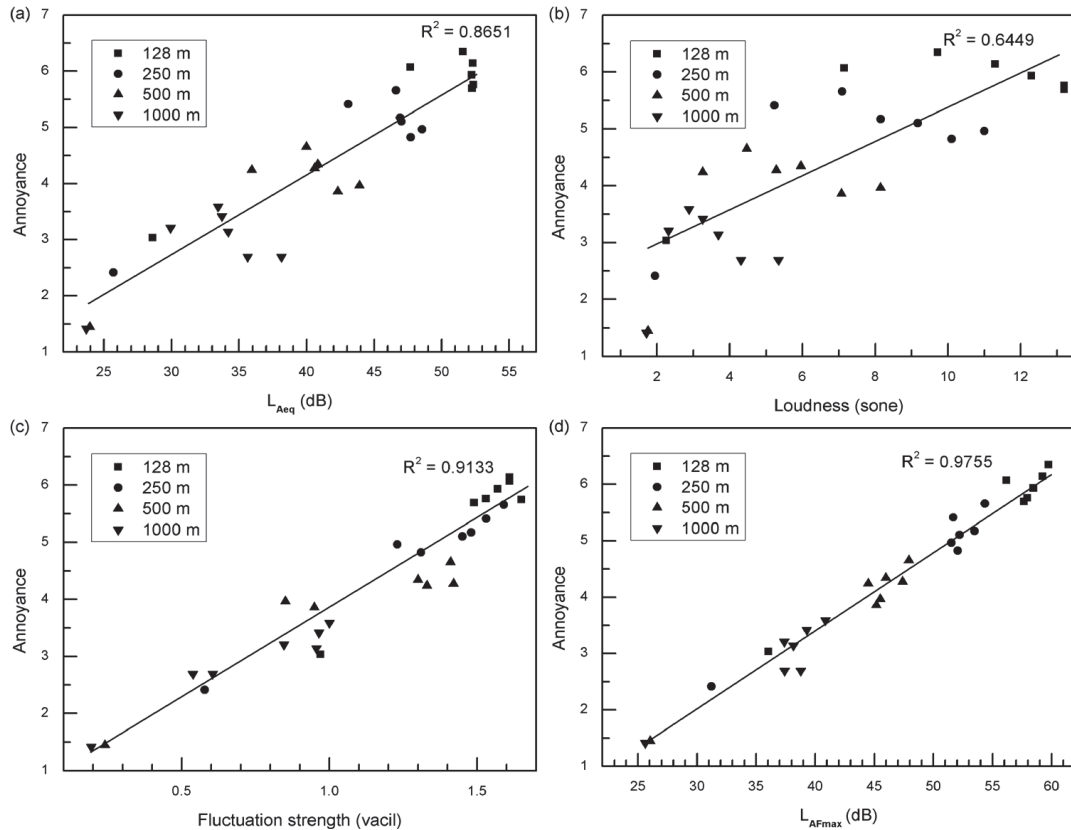


Fig. 3.16. Correlation between four noise metrics and noise annoyance using linear regression analysis: (a) L_{Aeq} , (b) loudness, (c) fluctuation strength, and (d) L_{AFmax} [78]

Using this as a background, the comparisons among the L_{Aeq} , L_{AFmax} , and modulation depth are made in terms of the distance and direction from the wind turbine in Fig. 3.17. As we have seen from the previous section, the A-weighted sound pressure level (L_{Aeq}) is maximum in downwind direction; L_{Aeq} at 1km from the wind turbine in downwind direction is about 3~4dB higher than that in the $\Psi = \pm 60^\circ$ directions. In contrast, because the modulation depth increases as the observer moves to the crosswind directions, the maximum A-weighted

sound pressure level (L_{AFmax}) is maximum in the $\Psi = \pm 60^\circ$ directions; L_{AFmax} at 1km from the wind turbine in the $\Psi = \pm 60^\circ$ directions is about 2~3dB higher than that in downwind direction. Consequently, it is likely that L_{AFmax} is more appropriate than L_{Aeq} to evaluate the sound directivity in terms of noise annoyance. It is also expected that the level of annoyance by wind turbine noise is maximum in the $\Psi = \pm 60^\circ$ directions.

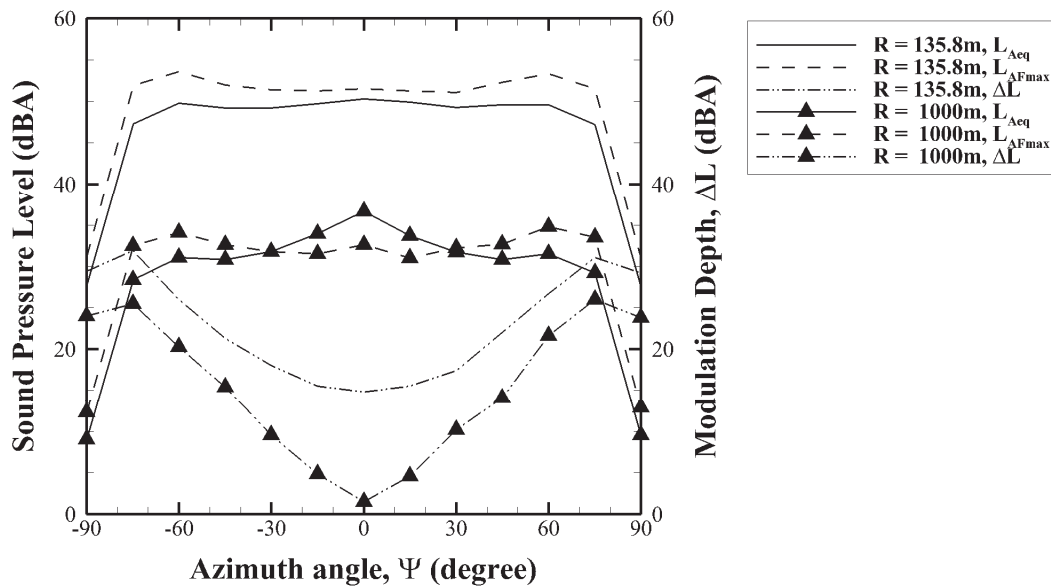


Fig. 3.17. Comparison of the L_{Aeq} , L_{AFmax} , and modulation depth in terms of the distance and direction from the wind turbine

3.3.2 Case II—Stationary in motion

Case II assumes that the wind turbine rotor is stationary in motion. At each time step, the wind turbine blades are positioned simply by multiplying the rotational speed by the time. In other words, for this assumption the retarded time is set to zero during calculations.

The acoustic signals are calculated at distances of $R=135.8\text{m}$ and 1000m from the wind turbine at azimuthal intervals of $\Delta\Psi = 15^\circ$. The sound pressure level and the modulation depth of the predicted signals are compared with those of Case I, as shown in Fig. 3.18. The result show that the sound directivity of Case II is similar to that of Case I; the sound pressure level is maximum in downwind direction, while it is minimum in crosswind direction.

However, the modulation depth greatly decreases as the wind turbine rotor is assumed to be stationary. In Case II, the modulation depths are almost zero in downwind directions irrespective of the distance from the wind turbine to the observers. This shows that the effect of the convective amplification is more significant on the amplitude modulation of wind turbine noise than that of the trailing edge noise directivity. Although the trailing edge noise directivity influences on the generation of the amplitude modulation, its effect is limited compared to the convective amplification, and it only influences in crosswind directions.

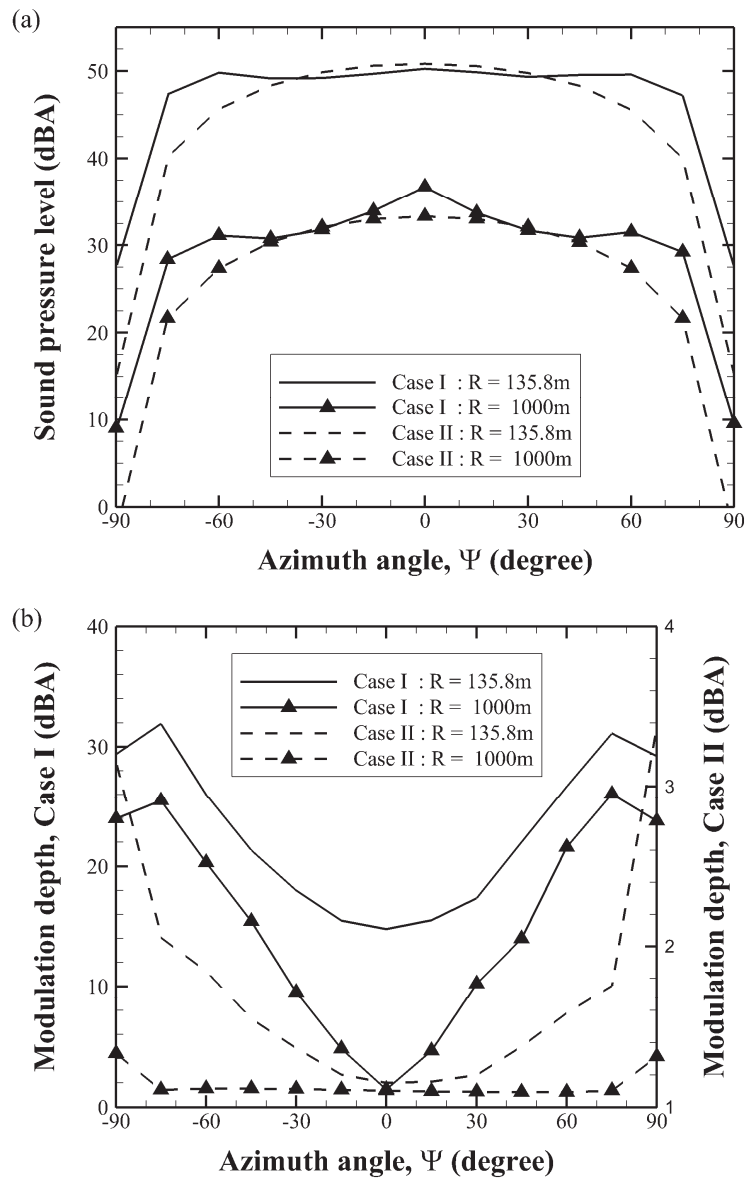


Fig. 3.18. Comparison of (a) The sound pressure level and (b) the modulation depth of the predicted acoustic signals between Case I and Case II.

3.3.3 Case III—Vertical wind shear

In Case III, to examine the effect of atmospheric stability on the amplitude modulation of wind turbine noise, the trailing edge noise from the wind turbine blades is calculated in two atmospheric conditions, which are a stable ($\alpha = 0.4$) and an unstable ($\alpha = 0.07$) conditions. The wind profiles corresponding to the two atmospheric conditions are obtained using an atmospheric power law, as shown in Eq. (3.10).

$$U = U_{hub} \left(\frac{h}{H} \right)^\alpha \quad (3.10)$$

Figure 3.19(a) shows the wind speed with respect to height from the ground in the two atmospheric conditions. The sectional inflow velocity and effective angle of attack in these two inflow conditions are calculated by WINFAS. Figure 3.19(b) presents the predicted variation of sectional effective angle of attack at $r/R = 0.90$. The results shows that the difference between the maximum and minimum effective angle of attack in a stable and an unstable atmosphere is about 3.9° and 0.7° , respectively. In contrast, the sectional inflow velocity was little influenced by the vertical wind shear.

Using the predicted sectional inflow velocity and effective angle of attack, the acoustic pressure radiated from the wind turbine blades is calculated in the same manner. The acoustic signals are calculated at distances of $R = 135.8\text{m}$ and 1000m from the wind turbine at azimuthal intervals of $\Delta\Psi = 15^\circ$. Figure 3.20 presents the maximum A-weighted sound pressure level of the predicted signals in terms of inflow wind conditions and compared with that of Case I. For an unstable atmosphere, the $L_{AF\max}$ is little different from that obtained for uniform inflow condition. However, a different trend is observed for a stable atmosphere. For

a stable atmosphere, the L_{AFmax} is increased to 2dB in the $\Psi = 60^\circ$ direction, while it is decreased to 3dB in the $\Psi = -60^\circ$ direction. This is due to the change of the effective angle of attack at positions where the swishing sound is generated.

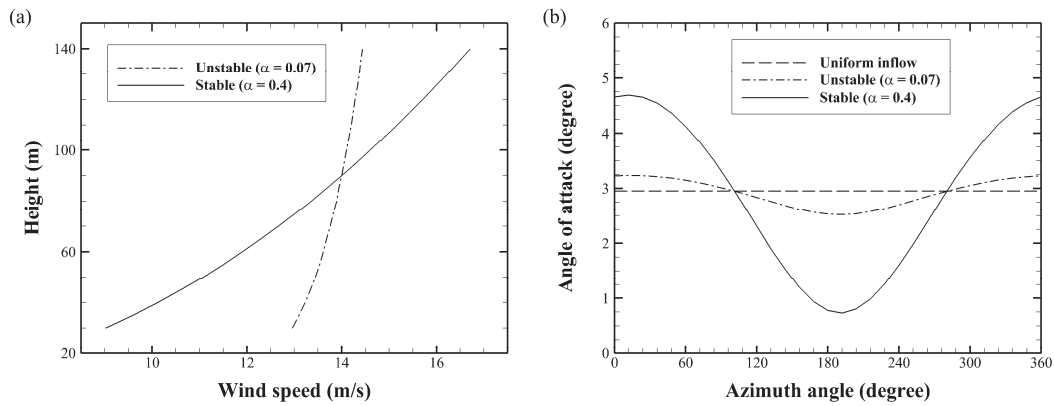


Fig. 3.19. (a) Wind speed with respect to height from the ground and (b) the variation of sectional effective angle of attack at $r/R = 0.90$

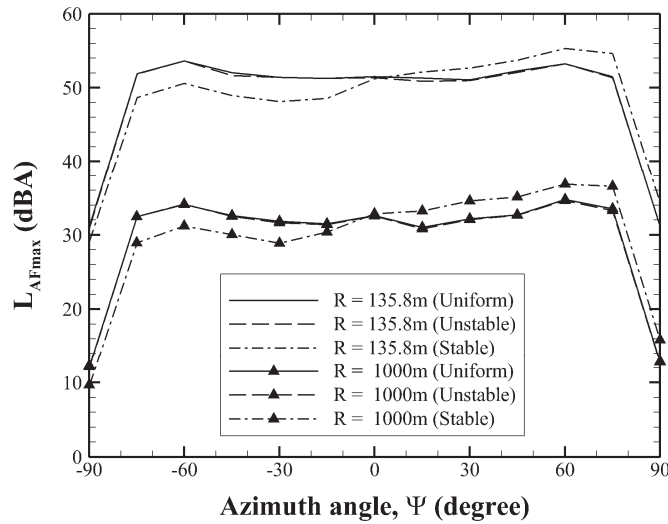


Fig. 3.20. The comparison of the maximum A-weighted sound pressure level in three inflow wind conditions at two distances from the wind turbine.

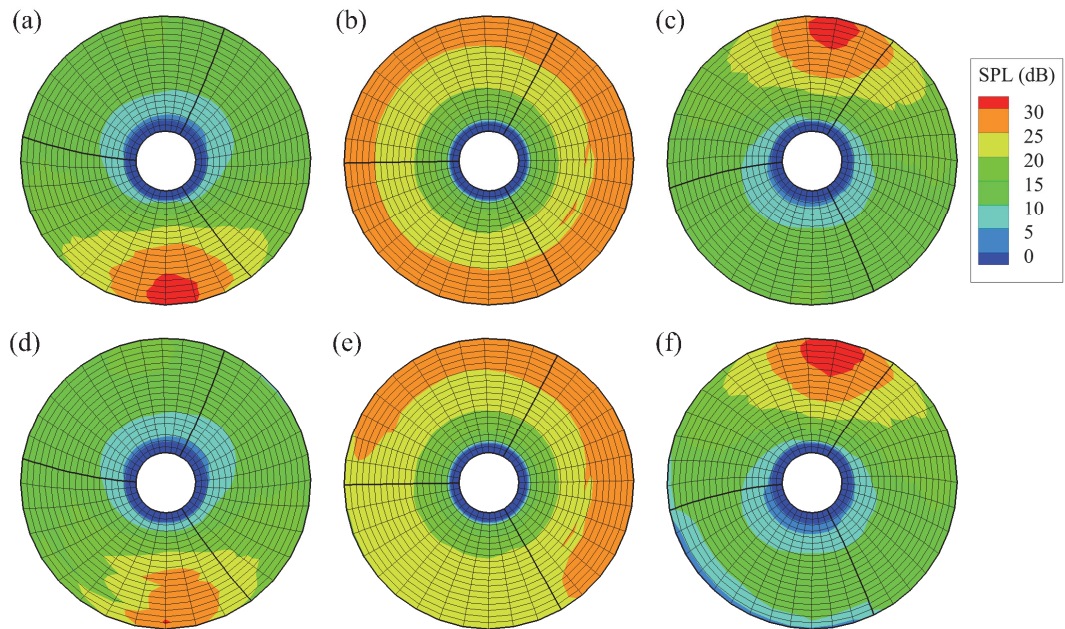


Fig. 3.21. Calculated source distributions on the rotor disk at $R=1000\text{m}$: (a) Unstable, $\Psi = -60^\circ$; (b) Unstable, $\Psi = 0^\circ$; (c) Unstable, $\Psi = 60^\circ$; (d) Stable, $\Psi = -60^\circ$; (e) Stable, $\Psi = 0^\circ$; (f) Stable, $\Psi = 60^\circ$

To examine the reason why the $L_{AF\max}$ varies, the noise source distributions on the rotor disk is calculated with respect to observer direction and atmospheric condition, as shown in Fig. 3.21. For the $\Psi = \pm 60^\circ$ directions the locations at which the noise from the wind turbine rotor is a maximum are the top and the bottom of the rotor, respectively. For a stable atmosphere the effective angle of attack increases at the top of the rotor and decreases at the bottom. Thus, depending on the observer direction from the wind turbine, $L_{AF\max}$ varies due to the change of the noise source strength.

Aud. 3.4. <https://drive.google.com/folderview?id=0B1dAuFX-upUweUoySUFnbGJGSEk&usp=sharing>

This audio is the sum of 6 acoustic signals, which are predicted at a distance of $R = 1000\text{m}$. The signals are presented as the following order: unstable, $\Psi = -60^\circ$; stable, $\Psi = -60^\circ$; unstable, $\Psi = 0^\circ$; stable, $\Psi = 0^\circ$; unstable, $\Psi = 60^\circ$; stable, $\Psi = 60^\circ$. Each signal repeats three times, and there is an interval of one second between different signals. This is a file of type “wav”.

Moreover, the predicted acoustic signals for the two atmospheric conditions can be heard in Aud. 3.4. It is discernible that the maximum sound level is increased or decreased due to the stable atmospheric condition. Note also that in a stable atmosphere the amplitude modulated sound is heard twice in the $\Psi = -60^\circ$ direction. This secondary amplitude modulated sound is produced because the additional asymmetry of the source distribution is introduced when the blades moves to the top of the rotor disk. As a result, for a stable atmosphere the frequency of the amplitude modulation of wind turbine noise can be twice the blade passing frequency in the direction where the blade passed upward.

3.3.4 Case IV—Turbulence ingestion

Case IV examines the effect of turbulence ingestion on the amplitude modulation of wind turbine noise. During the operation of a wind turbine, the turbulence can be ingested to the rotor disk due to wakes from other wind turbines or atmospheric turbulence. Thus, depending on the atmospheric or operation condition, turbulence ingestion noise may or may not be generated.

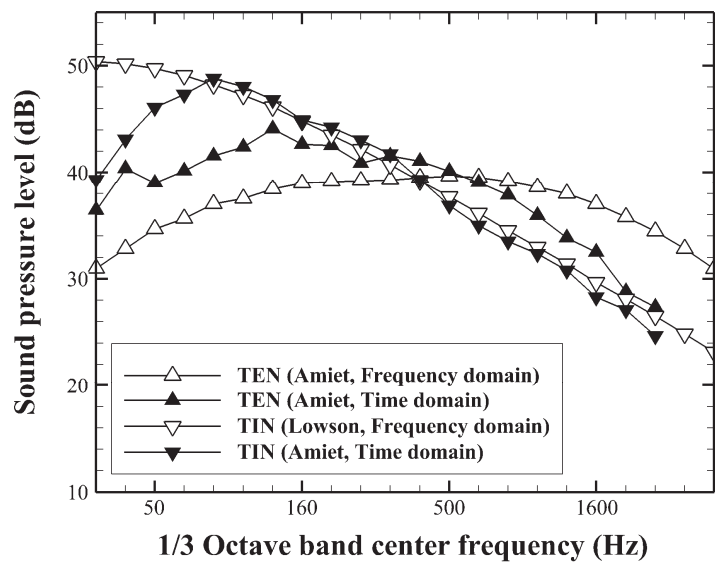


Fig. 3.22. Comparison of 1/3 octave band frequency spectra between frequency domain modeling and time domain modeling

The use of Amiet’s turbulence ingestion noise model enables us to predict the acoustic pressure because this model gives the unsteady pressure on the blade surface. However, this model does not predict well the sound pressure level at low Mach number due to the flat-plate

assumption [68]. On the other hand, the model proposed by Lawson [29], which is a simple empirical form based on the Amiet's model, is designed for the prediction of wind turbine noise, so this model is suitable for the prediction of one-third octave band frequency spectrum. Thus, in this work, to obtain the frequency spectrum properly with the Amiet's model, the parameters used in the Amiet's model are arbitrarily chosen to result in the best agreement with the prediction with Lawson's model. The one-third octave band spectrum obtained from the time domain modeling is compared with that from the frequency domain modeling, as shown in Fig. 3.22. The comparison result of the turbulence ingestion noise shows that the discrepancy is less than 2dB except at low frequencies.

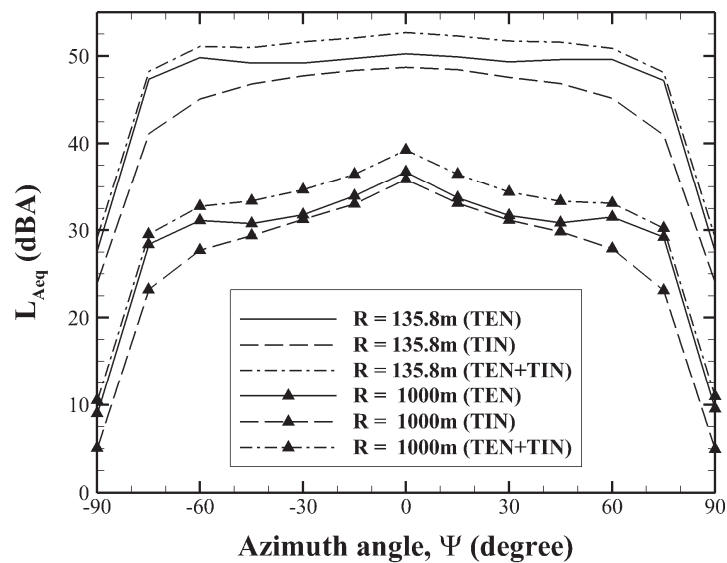


Fig. 3.23. The A-weighted sound pressure level of the trailing edge noise and turbulence ingestion noise at two distances from the wind turbine

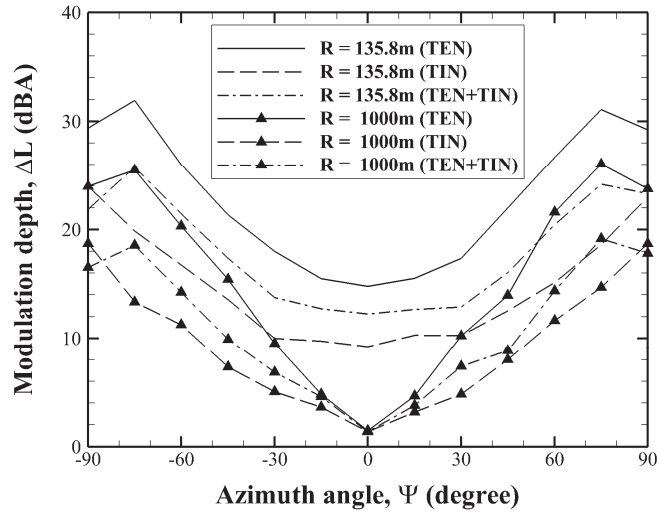


Fig. 3.24. The modulation depth of the trailing edge noise and turbulence ingestion noise at two distances from the wind turbine

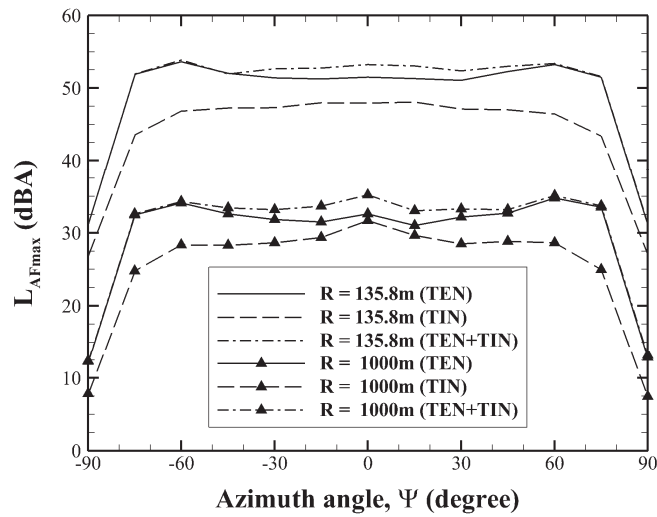


Fig. 3.25. The maximum A-weighted sound pressure level of the trailing edge noise and turbulence ingestion noise at two distances from the wind turbine

Figures 3.23 and 3.24 compare the A-weighted sound pressure level and the modulation depth of the trailing edge noise, turbulence ingestion noise, and their summation at two distances from the wind turbine, respectively. Due to the existence of the turbulence ingestion noise, the A-weighted sound pressure level increases for all distances and directions, while the modulation depth decreases. However, the maximum A-weighted sound pressure level shown in Fig. 3.25 increases only in downwind direction, but it does not increase in the $\Psi = \pm 60^\circ$ directions, where the amplitude modulation is mainly perceived. Hence, it is expected that the annoyance caused by the amplitude modulation does not increase much due to the turbulence ingestion noise.

To examine why the L_{AFmax} increases little in the $\Psi = \pm 60^\circ$ directions, the noise source distribution on the rotor disk is calculated for the trailing edge noise and the turbulence ingestion noise at 1km from the wind turbine, as shown in Fig. 3.26. The calculated source distributions reveal that the locations where the maximum sound levels are generated are different in terms of the noise source. This difference is because the sound directivities of the two noise sources are different from each other, as already shown in Chapter 3.2.4. Consequently, in the $\Psi = \pm 60^\circ$ directions, the turbulence ingestion noise cannot influence at the moment when the trailing edge noise is maximum.

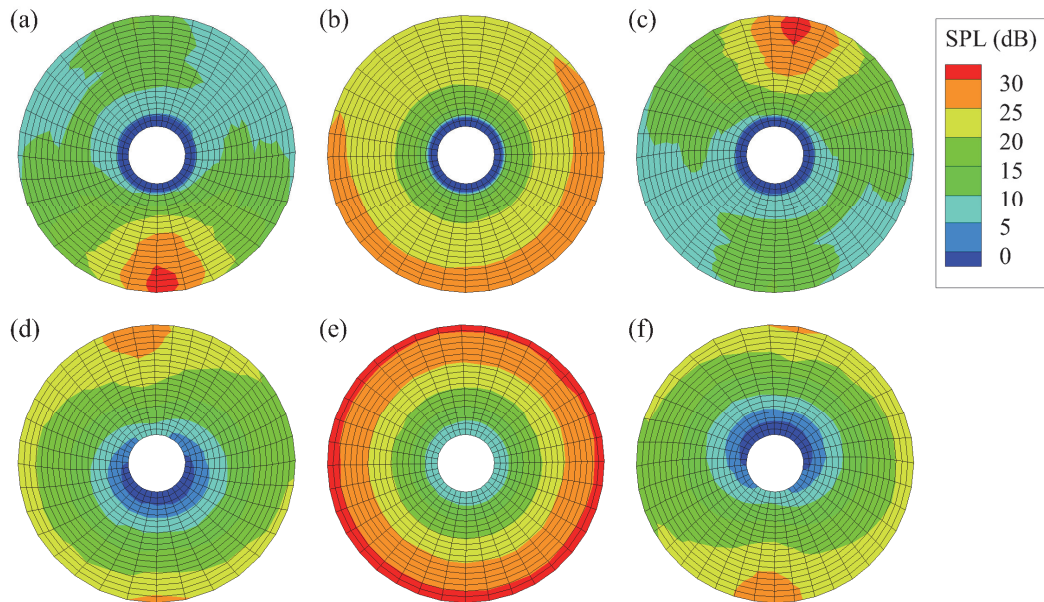


Fig. 3.26. Calculated source distributions on the rotor disk at $R=1000\text{m}$: (a) Trailing edge noise, $\Psi = -60^\circ$; (b) Trailing edge noise, $\Psi = 0^\circ$; (c) Trailing edge noise, $\Psi = 60^\circ$; (d) Turbulence ingestion noise, $\Psi = -60^\circ$; (e) Turbulence ingestion noise, $\Psi = 0^\circ$; (f) Turbulence ingestion noise, $\Psi = 60^\circ$

3.4 Discussion

Using the proposed numerical method, this study successfully predicts the acoustic pressure radiated from a wind turbine. Because this method provides us with the ability to actually hear the noise from a wind turbine, the present results will be utilized to predict the adverse effect of wind turbine noise on people before the construction of wind farms. Moreover, this study can be used for other researches related to annoyance or perception of wind turbine noise. For example, as already introduced in Chapter 3.3.1.4, Seong et al. produced acoustic signals by using the method proposed in this study and performed a listening test with them to find a noise index which is best correlated with noise annoyance.

The acoustical characteristics of wind turbine noise are quite different with respect to the distance and direction from the wind turbine, although the operating and atmospheric conditions are identical. In the vicinity of a wind turbine, typical swishing sounds are perceived from all azimuthal directions. On the other hand, at long distances from a wind turbine, low-frequency amplitude-modulated sounds are heard in particular directions. Moreover, in contrast to the swishing sounds, these low-frequency sounds are heard only at the moments when the sound pressure level is sufficiently high, e.g., when the blades pass the red contours shown in Fig. 3.15. This effect may make the wind turbine noise seem more impulsive at long distances despite the fact that its overall sound pressure level is low.

The results from this study clearly show that the amplitude modulation of wind turbine noise can be heard even at long distances from a wind turbine, which confirms the previous reports by van den Berg [7, 8]. However, although van den Berg suggested that the thumping sound occurs due to excessive vertical wind shear at night, the numerical results from this study

propose that even when a uniform wind is blowing into the rotor disk, different types of noise can be heard depending on the observer location. Moreover, these results indicate that the amplitude modulation greatly decreases provided that the wind turbine rotor is stationary. This implies that the main cause of the thumping sound could be the convective amplification rather than the trailing edge noise directivity or the strong wind shear.

Figure 3.27(a) and (b) present the variation of two angles, ϕ_1 and ϕ_2 with respect to rotor azimuth, respectively, for an observer who locates at a distance of the hub height from the turbine. Fig. 3.27(c) also shows the variation of $1/(1-M_r)$ at the same distance, where M_r is the Mach number in the radiation direction. These three values are calculated at the center of the outermost segment of the blade. It is clearly seen that all the three values vary considerably as the blades rotate. This leads to the variation of the sound pressure level of trailing edge noise and makes the periodic swishing sound. However, it is important to note that these variations with respect to blade rotation are still present when the observer is located far from the turbine. Figure 3.28(a), (b), and (c) show the calculated values for ϕ_1 , ϕ_2 , and $1/(1-M_r)$, respectively, when the observer is at a distance of 1km from the turbine. Figures 3.27 and 3.28 demonstrate that in the downwind direction the variation of the three values greatly reduces as the distance increases. However, in other directions the variation does not decrease or it decreases slightly but is still high enough to make the periodic swishing sound. This is why the amplitude modulation in wind turbine noise exists even at long distances.

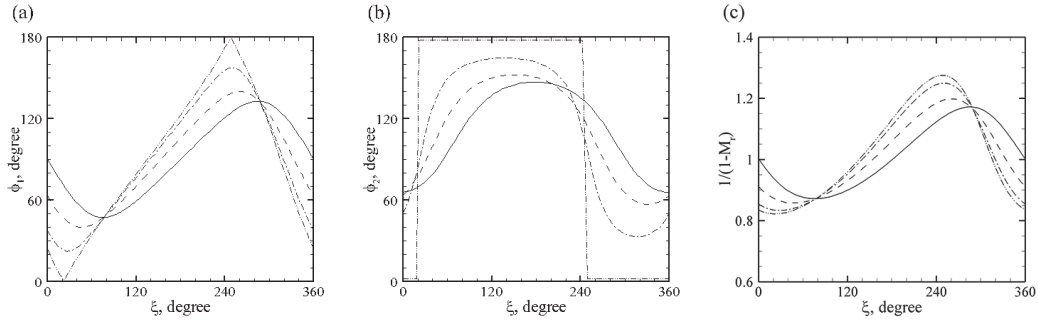


Fig. 3.27. Angles from (a) the x_1 -axis and (b) x_2 -axis of the outermost segment of the blade to an observer at $R = 90\text{m}$ with respect to the rotor azimuth; (c) $1/(1-M_r)$ of the outermost segment of the blade to an observer at $R = 90\text{m}$ with respect to the rotor azimuth: $\Psi = 0^\circ$ (————), $\Psi = 30^\circ$ (— — —), $\Psi = 60^\circ$ (— · — ·), and $\Psi = 90^\circ$ (— · — ·)

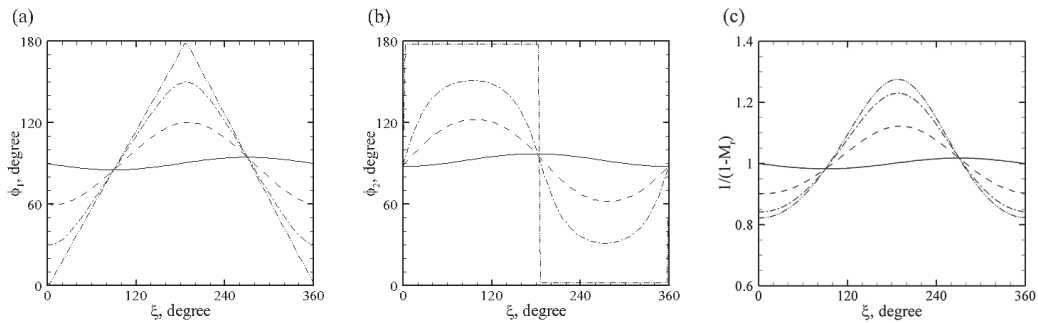


Fig. 3.28. Angles from (a) the x_1 -axis and (b) x_2 -axis of the outermost segment of the blade to an observer at $R = 1000\text{m}$ with respect to rotor azimuth; (c) $1/(1-M_r)$ of the outermost segment of the blade to an observer at $R = 1000\text{m}$ with respect to the rotor azimuth: $\Psi = 0^\circ$ (————), $\Psi = 30^\circ$ (— — —), $\Psi = 60^\circ$ (— · — ·), and $\Psi = 90^\circ$ (— · — ·)

Nevertheless, the strong wind shear additionally increases the strength of the amplitude modulation in wind turbine noise. At long distances in the directions where the blade passes downward, the amplitude-modulated sound occurs when the blades are at the top of the rotor disk, as shown in Fig. 3.15. Hence, if the vertical wind shear is strong, the effective angle of

attack at the top of the rotor disk will increase, as will the sound level of the amplitude-modulated sound in these directions. The numerical results indicate that for a stable atmosphere of $\alpha = 0.4$, the L_{AFmax} is increased to up to 2dB in these directions. In addition, in the downwind directions, sound rays are bent toward the ground in a strong wind shear [79]. This effect will also raise the level of the amplitude-modulated sound in the downwind directions.

Furthermore, it is found that the effect of the turbulence ingestion on the amplitude modulation is only a minor factor. The amplitude modulation caused by the turbulence ingestion noise has a different phase from that by the trailing edge noise, so the L_{AFmax} does not increase in spite of the existence of turbulence ingestion. However, excessive turbulence ingestion still has a possibility to increase the amplitude modulation if the level of turbulence ingestion noise greatly exceeds that of trailing edge noise. More studies will be necessary to identify the effect of excessive turbulence ingestion on the amplitude modulation of wind turbine noise.

Although the amplitude modulation in wind turbine noise occurs as long as the wind turbine operates, it will only be heard in certain directions. The results from this study indicate that the modulation depth is large near the rotation plane. However, there is little possibility of perceiving the sound in this direction, because the sound pressure level is too low; the overall sound pressure level is less than 20dBA in the crosswind directions. On the other hand, in the downwind direction, even though the sound pressure level is relatively high, the amplitude modulation does not exist. Thus, this sound will be easily masked by background noise. However, the amplitude modulation may be perceived in the directions of about $\Psi = \pm 60^\circ$. In these directions, not only does the amplitude modulation exist, but also the sound level is relatively high even at long distances from the turbine. Therefore, if the background noise level

is quite low, there is a possibility of perceiving the amplitude modulation in these directions. Detailed experimental observations would be required to validate this hypothesis.

In addition, whether the wind turbine noise is perceived or not depends on the one-third octave band sound pressure level of the background noise. For a modulation frequency of 1Hz, just-noticeable degree of amplitude modulation of white noise is 5% ($\Delta L = 1\text{dB}$) when the sound pressure level is over 30dB [80]. Accordingly, it can be estimated that the amplitude modulation of wind turbine noise is perceived provided that the maximum A-weighted sound pressure level (L_{AFmax}) in any frequency band of wind turbine noise is roughly over 1dB higher than the A-weighted equivalent sound pressure level (L_{Aeq}) in the same frequency band of background noise.

Chapter 4

Wind turbine noise reduction techniques

4.1 Introduction

In the previous chapter, it was found that wind turbine noise can be heard even at long distances due to the amplitude modulation of wind turbine noise. For this reason, reducing the noise from wind turbines is important. Wind turbine aerodynamic noise can be reduced by controlling the turbulence ingestion noise and the trailing edge noise. However, because the turbulence ingestion noise has little relation to the shape of the wind turbine blade but is instead largely dependent on the inflow velocity and the turbulence characteristics, reducing the noise levels associated with it is difficult. On the other hand, the trailing edge noise can be reduced by altering the turbulent boundary layer structure or the trailing edge shape.

For this reason, several attempts have been made to reduce the trailing edge noise by modifying the airfoil shape or attaching noise reduction materials to the blades. Howe analytically investigated the effect of serrated or sawtooth trailing edges on the trailing edge noise reduction [11, 12]. Lutz et al. designed low-noise airfoils and conducted wind tunnel tests to verify the noise reduction due to airfoil modification [13]. Bertagnolio et al. also designed new airfoil to reduce trailing edge noise using an optimization algorithm [14]. Herr and

Dobrzynski experimentally examined a brush-type trailing edge for the reduction of trailing edge noise [15]. However, most of these studies have focused on two-dimensional flow, and only a few studies have practically applied these techniques to an operating wind turbine, which can be influenced by atmospheric conditions such as atmospheric turbulence [16, 17]. Thus, more studies are needed to practically reduce the wind turbine aerodynamic noise.

The purpose of this study is to reduce the turbulent-boundary-layer trailing edge noise generated from a 10kW wind turbine rotor [18]. The trailing edge noise is first reduced by modifying the airfoil shape and the blade planform, while the operating schedule and the rotor diameter remain fixed. To obtain the optimal designs of the airfoil shape and the blade planform, optimization methods that involve genetic algorithms are used. In designing our optimal blade, the optimized airfoil is first determined based on a section of the baseline blade. The optimal blade is then designed with this optimized airfoil. The optimized blade design is verified with wind tunnel experiments. Moreover, based on a 10kW wind turbine, a field experiment is performed to examine the effect of trailing edge serrations on the wind turbine noise reduction [19]. The serrated trailing edge extensions are designed for a tapered baseline blade, and they are attached on the pressure side of the baseline blades. Noise measurement is carried out for the baseline and serrated blades.

4.2 Design optimization of airfoil and blade planform

4.2.1 Airfoil design optimization

4.2.1.1 Airfoil optimization procedure

In order to reduce airfoil self-noise generated from the wind turbine blades, the blade section is first modified from that of the baseline blade by using an optimization method. Because trailing edge noise is mainly generated in the outboard region of wind turbine blades, the outboard section should be redesigned for noise reduction. In this study, the blade section at $r/R=0.75$ is selected as the baseline airfoil. To modify the baseline airfoil, shape functions are added linearly to the airfoil geometry by the method proposed by Hicks and Henne [81]. A total of six shape functions, shown in Eq. (4.1), are applied to the upper and lower surfaces.

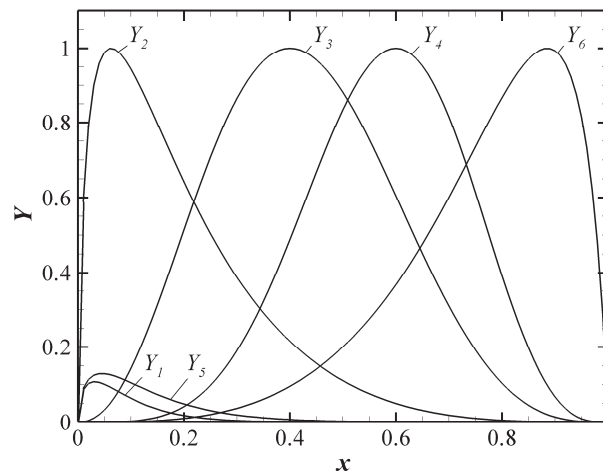


Fig. 4.1. Airfoil shape modification functions

$$y = y_0 + \sum_{i=1}^6 X_i Y_i(x) \quad (4.1)$$

where

$$Y_1(x) = x^{0.5} (1-x) e^{-15x},$$

$$Y_2(x) = \sin^3(\pi x^{0.25}),$$

$$Y_3(x) = \sin^3(\pi x^{0.757}),$$

$$Y_4(x) = \sin^3(\pi x^{1.357}),$$

$$Y_5(x) = x^{0.5} (1-x) e^{-10x},$$

$$\text{and } Y_6(x) = \sin^3\{\pi(1-x)^{0.32}\}.$$

In Eq. (4.1), X_i and Y_i are the shape function coefficients and shape functions, respectively.

The six shape functions are plotted in Fig. 4.1.

A multi-island genetic algorithm is used to determine the optimal values of the shape function coefficients [82]. The objective function for the optimization is defined as the overall sound pressure level of the trailing edge noise. The Reynolds number, Mach number, and angle of attack used in the calculation are 1.32×10^6 , 0.167, and 4° , respectively. These correspond to the aerodynamic conditions of the blade section at $r/R = 0.75$ for the rated wind speed. In addition, the span and chord length used in the calculation are 3.6m and 0.3423m, respectively; this chord length is identical to that of the blade section at $r = 0.75R_r$. The observer is located upwards from the trailing edge and the distance from the trailing edge to the observer is 3m.

A semi-empirical model proposed by Brooks, Pope, and Marcolini [2] is used to predict the overall sound pressure level of the trailing edge noise. They performed extensive wind tunnel experiments to measure airfoil self-noise from NACA0012 airfoil models. The semi-empirical model was made based on the results of these experiments. According to [2], the one-third octave band sound pressure level (SPL) of trailing edge noise can be described by

$$\text{SPL}_{\text{TEN}} = 10 \log \left(10^{\text{SPL}_\alpha/10} + 10^{\text{SPL}_s/10} + 10^{\text{SPL}_p/10} \right) \quad (4.2)$$

where

$$\text{SPL}_p = 10 \log \left(\frac{\delta_p^* M^5 d \bar{D}}{r_e^2} \right) + A \left(\frac{\text{St}_p}{\text{St}_1} \right) + (K_1 - 3) + \Delta K_1,$$

$$\text{SPL}_s = 10 \log \left(\frac{\delta_s^* M^5 d \bar{D}}{r_e^2} \right) + A \left(\frac{\text{St}_s}{\text{St}_1} \right) + (K_1 - 3),$$

$$\text{and } \text{SPL}_\alpha = 10 \log \left(\frac{\delta_s^* M^5 d \bar{D}}{r_e^2} \right) + B \left(\frac{\text{St}_s}{\text{St}_2} \right) + K_2.$$

In Eq. (4.2), δ^* , St , d , \bar{D} indicate the boundary layer displacement thickness, Strouhal number, wing span, and streamwise noise directivity, respectively. The subscript p , s , and α represent pressure side, suction side, and nonzero angle of attack effect, respectively. The function A and B define the spectral shapes of the trailing edge noise. St_1 and St_2 are the peak Strouhal numbers where the trailing edge noise is maximum. K_1 , K_2 , and ΔK_1 are empirical constants to adjust the level of trailing edge noise. The definitions of the spectral curves, the peak Strouhal numbers, and the empirical constants are detailed described in [2].

For the directivity function, this model uses a cardioid-type directivity pattern, which is the theoretical directivity for a semi-infinite flat plate. This directivity is based on the assumption that the chord length is much larger than the dominant acoustic wavelength, which is not satisfied in the present calculation. However, in the present case, the noise is predicted for an observer normal to the airfoil chord, so that the results would be unaffected by this directivity; the directivity function simply equals one.

The displacement thicknesses of the suction and pressure side boundary layers in Eq. (4.2) are calculated by using XFOIL code [31]. The angle of attack used for the calculation of boundary layer displacement thickness is based on the aerodynamic angle of attack at a zero lift angle.

Although the sound pressure level of the trailing edge noise is reduced by using the optimization procedure, the aerodynamic performance of the modified blade should not be worse than that of the baseline blade. In this optimization procedure, a constraint condition is chosen to not only maintain but also enhance the aerodynamic performance of the optimized airfoil; this is shown in Eq. (4.3).

$$L/D_{\text{optimized}, \alpha=4^\circ} > L/D_{\text{baseline}, \alpha=4^\circ} \times 160\% \quad (4.3)$$

where L and D are the lift and drag of the airfoil, respectively. XFOIL code is again used to calculate lift and drag coefficients [31].

Moreover, the maximum thickness of the modified airfoil, t_{max} is also subject to a constraint. If the maximum thickness of the optimized airfoil is thicker than that of the baseline airfoil, there is a possibility of an increase in the blade weight. On the other hand, if the maximum

thickness is thinner than the baseline, a structural problem may arise in the inboard region. Thus, the constraint condition in this optimization procedure is chosen as shown in Eq. (4.4).

$$-5\% < \frac{t_{\max} - t_{\max, \text{baseline}}}{t_{\max, \text{baseline}}} < 5\% \quad (4.4)$$

Although the object function is defined as the level of the trailing edge noise, the trailing edge bluntness noise is also calculated for the purpose of evaluating the airfoil self-noise of the baseline and optimized airfoils. The trailing edge bluntness noise is predicted by the same model proposed by Brooks, Pope, and Marcolini [2]. The trailing edge thickness normalized by chord length is 0.0082, and the flow angle is 22° , which is the solid angle of the airfoil surface near the trailing edge.

4.2.1.2 Airfoil optimization result

Figure 4.2 presents the geometry of the baseline and optimized airfoils. The maximum thickness is decreased from 21.6% to 20.8% in the optimized airfoil. The trailing edge thickness and solid angle at the trailing edge change little after the optimization. Notably, the gradient of the airfoil shape is reduced in the vicinity of the trailing edge.

The overall sound pressure levels of the airfoil self-noise with respect to angle of attack for the baseline and optimized airfoils are shown in Fig. 4.3. The result indicates that the optimized airfoil generated less noise than the baseline airfoil at positive angles of attack. The noise reduction of 3.3dB is achieved at an angle of 4° , which is the target angle for the optimization. The reason for the noise reduction may be that the decrease of the gradient near the trailing edge leads to a decrease in the boundary layer displacement thickness.

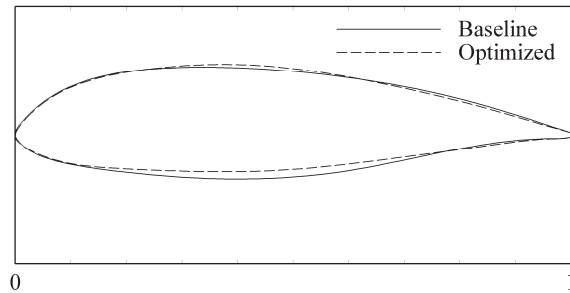


Fig. 4.2. Geometries of the baseline and the optimized airfoils

Moreover, although trailing edge noise is the dominant noise source of the airfoil self-noise, the trailing edge bluntness noise level becomes comparable to that of the trailing edge noise at negative angles of attack. This condition occurs because the boundary layer is thin at a low angle of attack, which leads to high ratio of trailing edge thickness to boundary layer displacement thickness. The airfoil self-noise from the optimized airfoil is higher than that from the baseline airfoil at negative angles of attack due to the high level of the trailing edge bluntness noise. However, this noise increase would not be a problem because the angle of attack of wind turbine blades is positive in typical operating conditions.

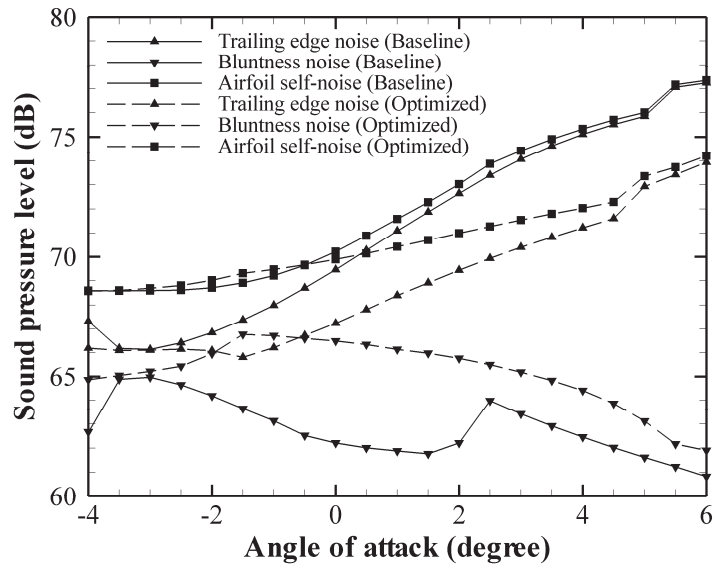


Fig. 4.3. Overall sound pressure levels of the airfoil self-noise for the baseline and optimized airfoil. The airfoil self-noise is the sum of trailing edge noise and trailing edge bluntness noise.

4.2.2 Blade design optimization

4.2.2.1 Blade optimization procedure

In the blade design procedure, the optimized airfoil obtained from the previous section is identically applied to all the blade sections. The blade planform is then optimized to obtain the blade that generates the least airfoil self-noise. The chord length distribution along the blade span is modeled as a linear function, as seen in Eq. (4.5).

$$C = c_1 \times (r - r_{\text{cut}}) / R_r + c_2, \quad (4.5)$$

where r_{cut} is the distance between the hub cutout and the rotor center, and R_r is the rotor radius. The twist distribution along the blade span is modeled to be inversely proportional to the blade radius, as shown in Eq. (4.6).

$$\tau = t_1 \times (r / R_r)^{-t_2} + t_3. \quad (4.6)$$

Thus, a total of five variables (c_1 , c_2 , t_1 , t_2 , and t_3) are used in the optimization procedure.

To design an optimized blade which has a low noise level in a range of wind speeds, the overall sound pressure levels of the trailing edge noise at wind speeds of 7m/s and 10m/s are chosen as the objective functions. The optimization problem has two objective functions, so the neighborhood cultivation genetic algorithm, which is effective for optimization problems with more than one objective function, is used in this optimization procedure [83].

The trailing edge noise generated from the wind turbine blades is predicted at a reference position according to IEC 61400-11 standard [56]. For the prediction of the trailing edge noise, each blade is divided into 20 equally spaced segments. The semi-empirical model used in the

previous section is then applied to each blade segment. One-third octave band spectra are obtained by summing up all the noise spectra of the blade segments with respect to retarded time. The inflow wind speed and the effective angle of attack at each blade segment, which is necessary for the prediction of the trailing edge noise, are calculated by using an in-house program which employed the blade element momentum theory.

Three constraints are imposed in the optimization procedure. First, to maintain the wind turbine performance in all ranges of wind speeds, power outputs at wind speeds of 2.5, 4, 7, and 10m/s are selected as constraints. In this study, to enhance the wind turbine performance, the constraint conditions are set as in Eqs. (4.7a) to (4.7d).

$$P_{2.5m/s} > P_{2.5m/s, \text{baseline}} \times 103\% \quad (4.7a)$$

$$P_{4m/s} > P_{4m/s, \text{baseline}} \times 105\% \quad (4.7b)$$

$$P_{7m/s} > P_{7m/s, \text{baseline}} \times 105\% \quad (4.7c)$$

$$P_{10m/s} > P_{10m/s, \text{baseline}} \times 105\% \quad (4.7d)$$

where P is the rotor power. Furthermore, to avoid increasing the blade weight or applied load to the blade root, the chord length and the solidity are selected as constraints, as shown in Eqs. (4.8) and (4.9).

$$C_{\text{root}} > C_{\text{root, baseline}} \quad (4.8)$$

$$\sigma_{\text{baseline}} \times 95\% < \sigma < \sigma_{\text{baseline}} \quad (4.9)$$

4.2.2.2 Blade optimization result

Figure 4.4 shows the chord and twist distributions for the baseline and optimized blades. The twist angle for the optimized blade is increased from that for the baseline blade. The chord length at the root is slightly longer than that of the baseline blade, whereas the chord length at the blade tip is shorter than that of the baseline blade.

The numerical predictions of the overall sound pressure level for the baseline and optimized wind turbines are plotted in Fig. 4.5. These predictions include not only trailing edge noise but also trailing edge bluntness noise. The result indicates that the optimized wind turbine generated less noise than the baseline wind turbine at most wind speeds. The airfoil self-noise is reduced by 2.3dB at a wind speed of 10m/s . At wind speeds less than 5m/s , little difference is observed between the sound pressure levels of the baseline and optimized blades. However, in this range of wind speeds, the sound pressure level of the airfoil self-noise is small compared with that of typical background noise. Thus, airfoil self-noise reduction at low wind speeds is unnecessary in most situations.

In addition, the prediction results show that the trailing edge bluntness noise is negligible compared with the trailing edge noise. However, for the optimized blade, the contribution of the bluntness noise to the overall noise increased as the wind speed increased.

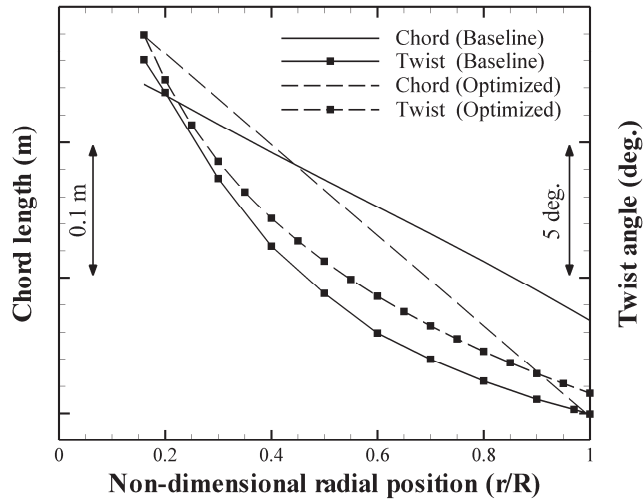


Fig. 4.4. Chord and twist distributions for the baseline and optimized blades

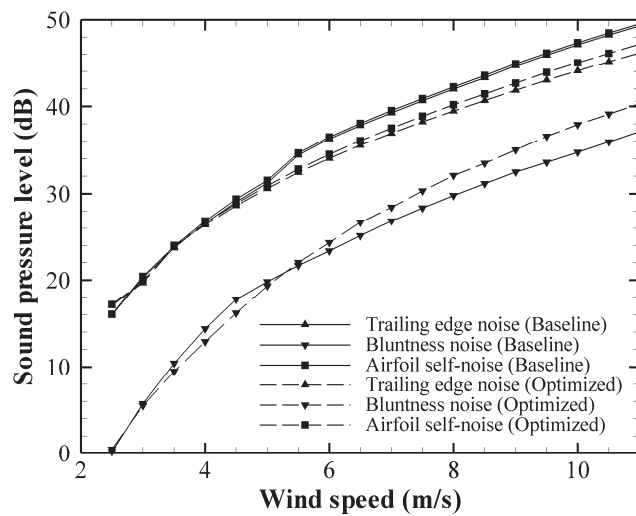


Fig. 4.5. Predicted overall sound pressure levels for the baseline and optimized wind turbines. The airfoil self-noise is the sum of the trailing edge noise and the trailing edge bluntness noise

4.2.3 Experimental results and discussion

A wind tunnel experiment was performed to validate the result of the design optimization [18]. The experiment was carried out in a semi-anechoic wind tunnel at Chungnam National University. Figure 4.6 shows a photograph of the wind tunnel test system and the semi-anechoic chamber. The wind tunnel has a cross section of $1.8\text{m} \times 1.8\text{m}$ and is capable of generating wind speeds of up to 35m/s . The anechoic chamber has a total volume of 211.9m^3 and a cut-off frequency of 150Hz , which is far below the frequency of typical airfoil self-noise.

The baseline and optimized rotors were scaled down by a factor of 5.71 for the wind tunnel test. The small-scale rotors had a diameter of 1.4m , and their rotational speeds ranged from 491RPM to 1473RPM . By increasing the rotational speed of the small-scale rotor, the tip speed of the model blades was set to be equal to that of the full-size 10kW wind turbine blades. Because the disk area of the small-scale rotors was smaller than the cross section of the wind tunnel, the interaction between the rotor blades and shear layer turbulence was expected to be negligible.

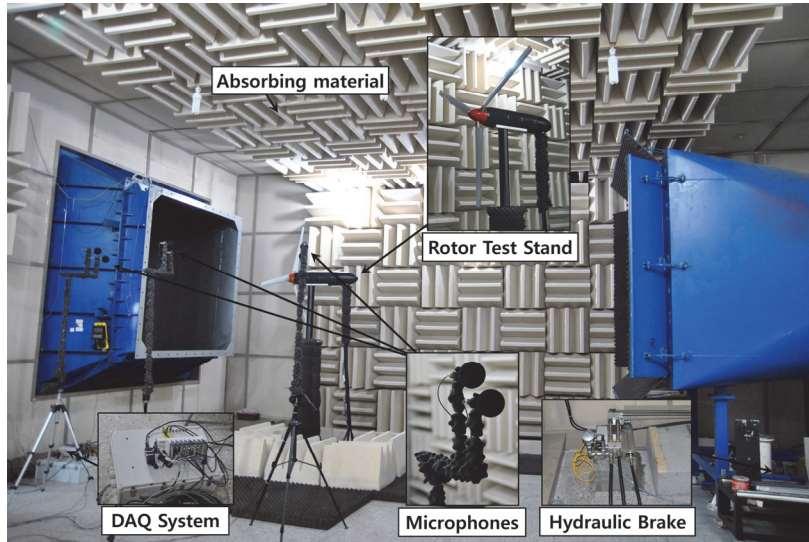


Fig. 4.6. Configuration for the wind turbine rotor test stand in the anechoic wind tunnel [18]

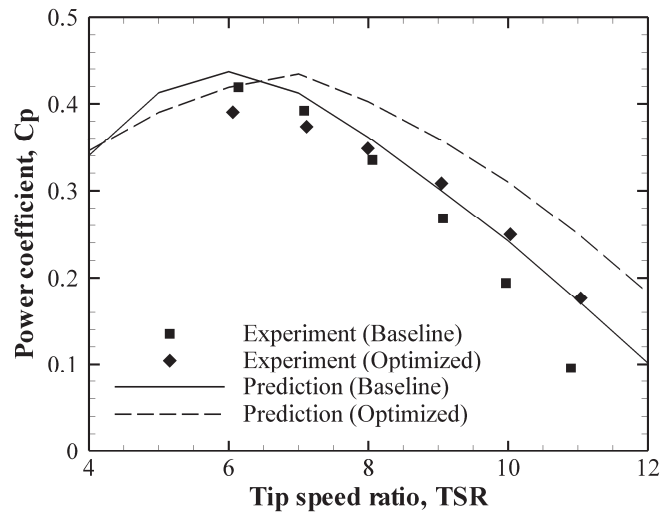


Fig. 4.7. Comparison of power coefficients between the experimental data and prediction results

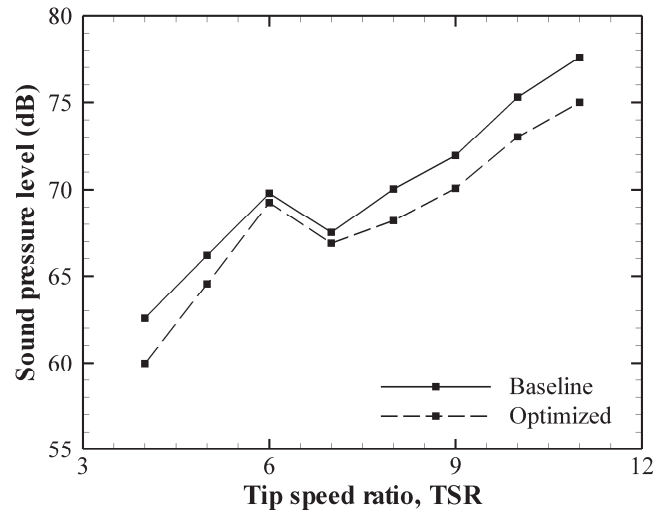


Fig. 4.8. Measured overall sound pressure levels for the baseline and optimized wind turbines

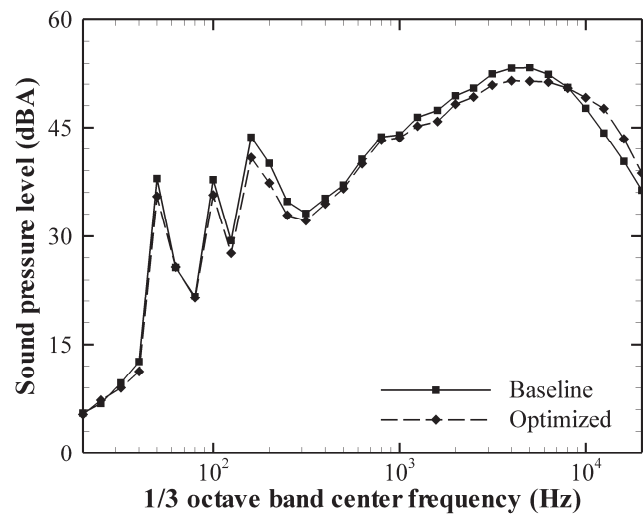


Fig. 4.9. Measured 1/3 octave band spectra for the baseline and optimized wind turbines

Figure 4.7 compares the measured and predicted power coefficients with respect to tip speed ratio. During the measurements, the wind speed was constant at 9m/s. An offset is found between the measured and predicted results. This error is possibly due to the mechanical losses in the rotor hub, which is not considered in the numerical predictions. Furthermore, the numerical results indicate that the power output of the optimized blade is higher than that of the baseline blade in the rated operating condition, which is at a tip speed ratio of about 7.5. However, little difference between the power coefficients of the baseline and optimized blade is observed in the experimental results.

Figure 4.8 shows the overall sound pressure level of the wind turbine noise with respect to tip speed ratio. The airfoil self-noise is reduced by up to 2.6dB due to the design optimization. The A-weighted one-third octave band spectra for the baseline and optimized blade are shown in Fig. 4.9, which were measured at a tip speed ratio of 8. The large hump centered at about 4.5kHz is the noise source due to trailing edge noise. This hump decreased as a result of the modification of the blade shape.

4.3 Serrated trailing edge blade

4.3.1 Experimental setup

The wind turbine model used in this experiment is a 10kW small wind turbine, already introduced in Chapter 2.3.3.1. Noise measurement is also carried out in the same manner described in the previous section.

From the numerical predictions introduced in Fig. 3.15, it was shown that most of the trailing edge noise is radiated from the outboard regions of the wind turbine blades. Little effect is expected on the sound pressure level of the trailing edge noise provided that the serrated trailing edge is applied to inboard regions. Thus, based on these predictions, the serrated trailing edges were applied from 75% to the tip of the rotor blades.

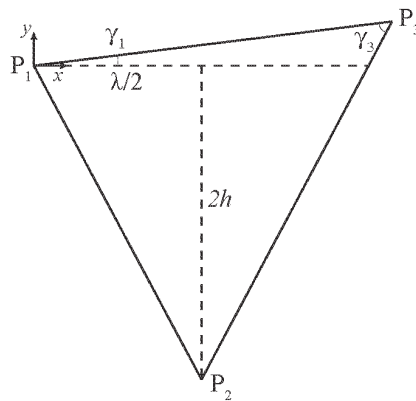


Fig. 4.10. Geometry of serrated trailing edge

The serrated trailing edges were designed as a typical sawtooth shape. For a tapered blade, the width, λ_s and the height, $2h_s$ of the serrated trailing edge can be defined in Fig. 4.10. To maintain the ratio, λ/h , of the width to the amplitude of the serration along the spanwise direction, both the width and height needed to uniformly vary along the radial direction. The coordinates of P_2 and P_3 in Fig. 4.10 were defined as Eqs. 4.10 and 4.11, respectively.

$$P_2(x, y) = (\lambda_s/2, -2h_s) \quad (4.10)$$

$$P_3(x, y) = \frac{\lambda_s \cos \gamma_1 + \lambda_s \cos \gamma_2 \cos(\pi - \gamma_1 - \gamma_2)}{1 - \cos^2 \gamma_2} (\cos \gamma_1, \sin \gamma_1) \quad (4.11)$$

The angle, γ_1 is the constant that is determined by the blade tapered angle, and γ_2 is the one defined by shape of the serrated trailing edge. For the blade used in this experiment, γ_1 and γ_2 were defined as Eqs. 4.12 and 4.13, respectively.

$$\gamma_1 = \tan^{-1} \frac{62.775}{1000} = 3.6 \text{ deg.} \quad (4.12)$$

$$\gamma_2 = \tan^{-1} \left(\frac{4h_s}{\lambda_s} \right) - \gamma_1 \quad (4.13)$$

Two types of serration geometry were tested in this study. The ratios, λ/h , of the width to the amplitude of the serration were selected to be 0.5 and 1.0. Although the blade chord length varied along the blade radial position, the ratios remained the same along the blade span. The height, $2h_s$, of the two serrations was set to be 15% of the local chord length. Furthermore, to evaluate the effect of the serrated trailing edges on noise reduction, a rectangular plate was also used to be attached to the blades. The rectangular plate had 1mm in thickness and 1m in span.

Its length was set to the amplitude, h , of the serrated trailing edge. Thus, a total of four cases were examined: the baseline blade, the two types of serrated trailing edges, and the rectangular plate trailing edge. The geometries of the two serrated trailing edge plates are illustrated in Fig. 4.11. The upper rectangular part of the plates is the portion that is attached to the blades.

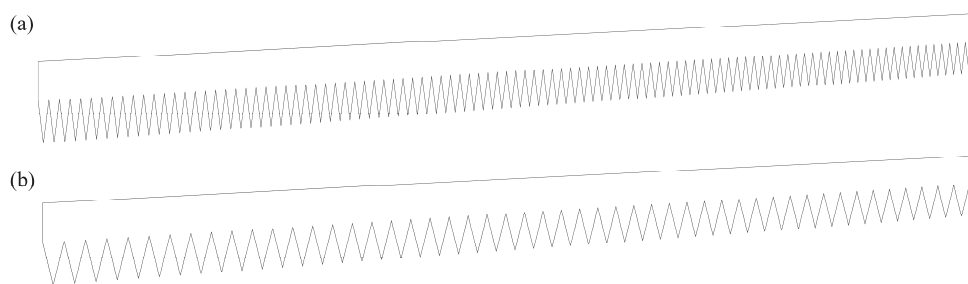


Fig. 4.11. Serrated trailing edge design: (a) $\lambda/h = 0.5$ and (b) $\lambda/h = 1.0$

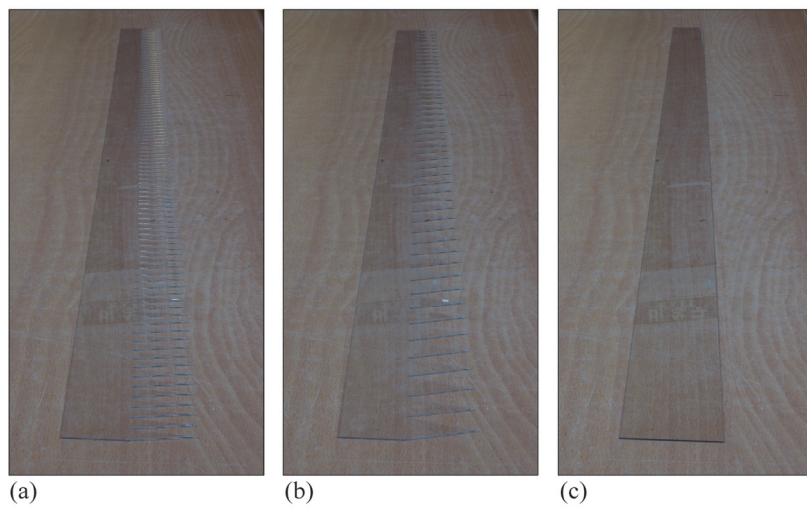


Fig. 4.12. Photographs of serrated trailing edges (a) $\lambda/h = 0.5$, (b) $\lambda/h = 1.0$, and (c) rectangular plate

Wind turbine blades having trailing edge serrations were designed by attaching serrated plates on the blades. The serrated plates were made of polycarbonate plastic with a thickness of 1mm, as shown in Fig. 4.12. The plates were attached on the pressure side of the blades with a double-sided film tape. The photographs of serrated trailing edge blade are shown in Fig. 4.13. The pressure side is selected because the turbulent boundary layer of the suction side makes more noise than that of the pressure side. The plates were firmly fixed during turbine operation, but could easily be detached by hand, when necessary. This enabled us to experiment several trailing edge cases with a single wind turbine rotor.



Fig. 4.13. Photograph of (a) attachment of serrated trailing edge and (b) serrated trailing edge blade

4.3.2 Results and discussion

The measured rotor power and sound pressure level were evaluated for the four trailing edge shapes. Figure 4.14 shows the one-minute average rotor power in terms of wind speed. Although the trailing edge plates were attached on the blades, the powers generated from each of the four rotors were similar with respect to wind speed. This results indicate that attached trailing edge plates had little effect on the wind turbine power curve. Figure 4.15 demonstrates the one-minute average A-weighted sound pressure level with respect to rotational speed. It is shown that the A-weighted noise level was reduced by up to about 5dB due to the use of the serrated trailing edges. Noise reduction is maximized at rotational speeds around 130RPM. However, it is unexpected that noise from not only the serrated blades but also the rectangular trailing edge blade was reduced from that produced by the baseline blade.

To investigate these results in more detail, one-third octave band spectra were calculated as shown in Fig. 4.16. The spectra were determined by taking energy average of one-minute spectra for each rotational speed range. The results indicate that low frequency mechanical noise was dominant in the range of 100~200Hz when the rotational speed was high. This low frequency noise was consistent regardless of the blade trailing edge.

Furthermore, the difference between the noise spectra of the baseline blade and the rectangular trailing edge blade may be explained by the noise reduction due to the decrease of trailing edge bluntness noise. The trailing edge bluntness noise was one of the dominant noise sources, although a previous study showed for a large wind turbine that the trailing edge bluntness noise is unimportant [63]. Trailing edge bluntness noise is generated provided that the

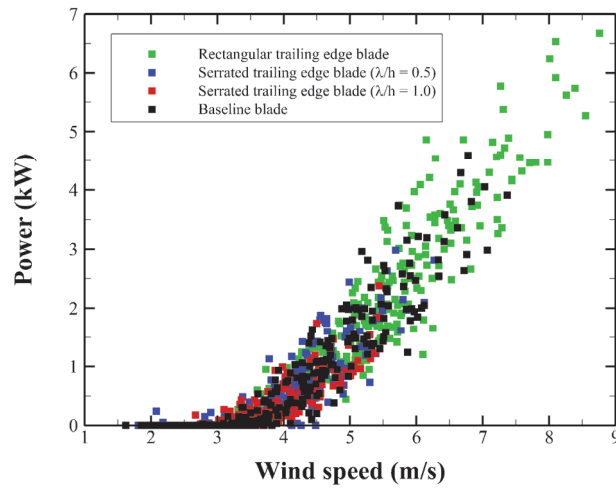


Fig. 4.14. Measured power for the baseline blade (black), the serrated blade of $\lambda/h = 0.5$ (blue), the serrated blade of $\lambda/h = 1.0$ (red), and the rectangular trailing edge blade (green)

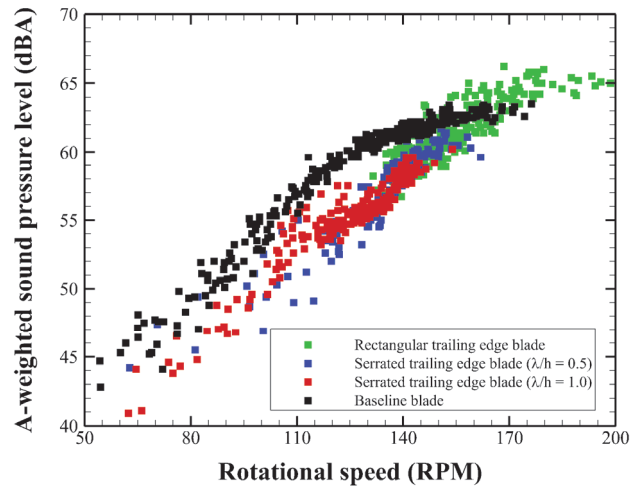


Fig. 4.15. Measured A-weighted sound pressure level for the baseline blade (black), the serrated blade of $\lambda/h = 0.5$ (blue), the serrated blade of $\lambda/h = 1.0$ (red), and the rectangular trailing edge blade (green)

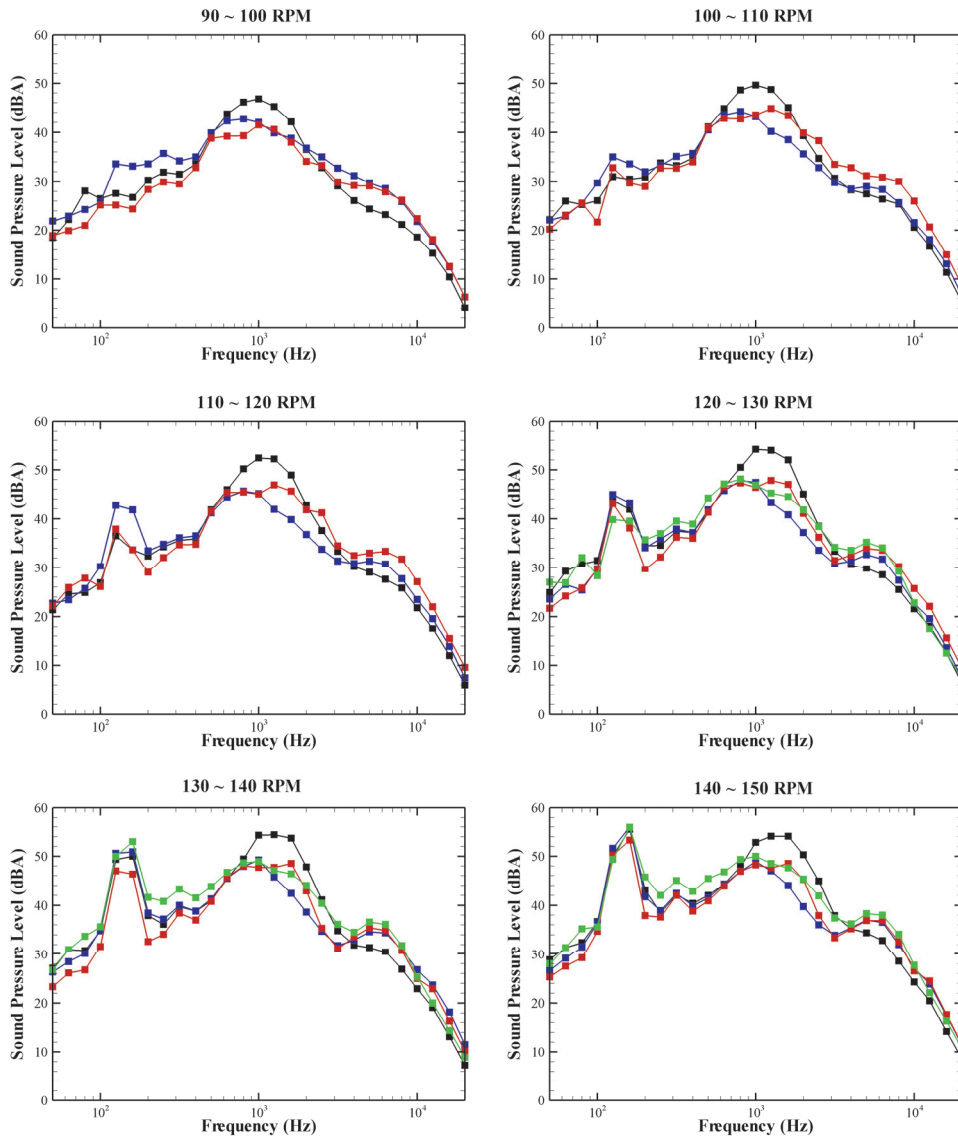


Fig. 4.16. 1/3 octave band spectra with respect to wind turbine rotational speed: the baseline blade (black), the serrated blades of $\lambda/h = 0.5$ (blue), $\lambda/h = 1.0$ (red), and the rectangular trailing edge blade (green)

height of the trailing edge is larger than about one-fifth of the boundary layer displacement thickness [63]. The trailing edge of the blade used in the experiment had a round shape and a diameter of about 4mm at the tip.

To compare the boundary layer displacement thickness and the trailing edge height for the blades, the boundary layer displacement thickness of the outboard region was predicted using the XFOIL code [31]. Table 4.1 presents the calculated boundary layer displacement thickness at various wind speeds. In Table 4.1, the peak frequency represents the predicted peak frequency for the trailing edge bluntness noise, and the minimum trailing edge height is the estimated minimum trailing edge height at which the trailing edge bluntness noise occurs. The results show that the ratios between the trailing edge thickness and the boundary layer displacement thickness were over 0.2 at all wind speeds; this led to the generation of the trailing edge bluntness noise.

Table 4.1. Normalized boundary layer displacement thickness, the ratio between the trailing edge height and boundary layer displacement thickness, peak frequency, and the minimum trailing edge height at wind speeds from 4m/s to 7m/s.

Wind speed (m/s)	δ^*/C	h_e/δ^*	Peak frequency (Hz)	h_{\min} (mm)
4	0.0113	1.41	1270	0.566
5	0.0116	1.38	1390	0.580
6	0.0121	1.32	1480	0.605
7	0.0125	1.28	1580	0.626

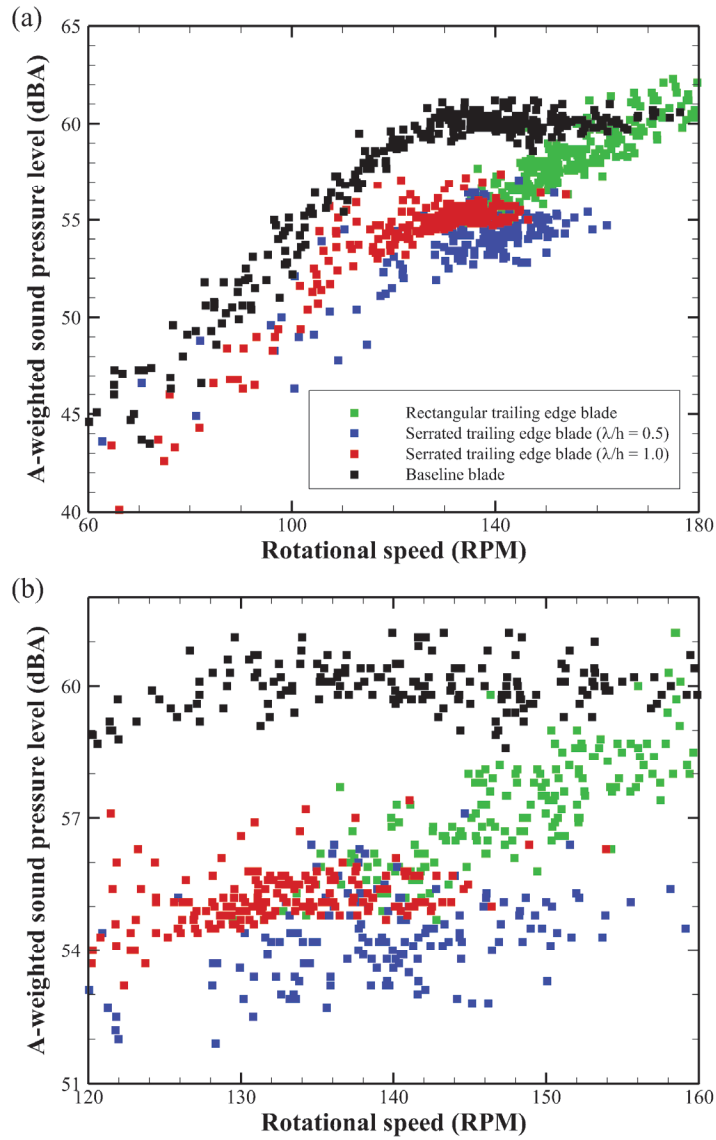


Fig. 4.17. (a) A-weighted sound pressure level of high-pass filtered sound and (b) zoom on overlap region: the baseline blade (black), the serrated blades of $\lambda/h = 0.5$ (blue), $\lambda/h = 1.0$ (red), and the rectangular trailing edge blade (green)

To remove the mechanical noise and evaluate the noise reduction effect, a high-pass filter was applied to the measured signals. The stop band of the high pass filter was 250Hz. Using the high-pass filtered signals, the A-weighted sound pressure level was again calculated in Fig. 4.17. Although the sound pressure level was not significantly reduced due to the serration in the case of the serrated blade with a ratio of 1.0, the serrated trailing edge with a ratio of 0.5 influenced on the trailing edge noise reduction. The overall sound pressure level of the serrated trailing edge blade was reduced by 1 ~ 3dB compared to the rectangular trailing edge blade. This reduction of the sound pressure level is expected to be due to the reduction of the trailing edge noise, which results from the trailing edge serrations.

Note also that, in practice, it is difficult to make blades with a sharp trailing edge because wind turbine blades are typically made of fiber-reinforced plastic. For a typical wind turbine blade, the trailing edge thickness is about 1mm to 3mm [1]. For large wind turbine blades, the boundary layer displacement thickness is much higher than this range of thickness. However, for small wind turbine blades, the trailing edge thickness should be less than 1mm to avoid trailing edge bluntness noise. Therefore, the results of this study also indicate that for a small wind turbine, trailing edge bluntness noise can easily occur unless the blades have very sharp trailing edges.

Chapter 5

Conclusions

The present study investigated the three topics related to aerodynamic broadband noise from wind turbines. First, a numerical method to predict the wind turbine aerodynamic noise is proposed using Amiet's trailing edge noise model with Rozenberg's wall-pressure spectral model for the first time. For the validation of the numerical method, noise measurement was also carried out for a 10kW wind turbine. From the comparisons of two-dimensional trailing edge noise and wind turbine noise between the predicted results and the experimental data, it was concluded that this numerical model not only gives a reliable prediction results, but also is suitable when fast computation is necessary such as for use in industrial applications. Accordingly, the prediction code developed based on XFOIL in this work could be used for industrial applications.

Moreover, time domain simulations for the wind turbine aerodynamic noise were performed to examine the main cause of the amplitude modulation of wind turbine noise, as well as to compare the acoustical characteristics depending on the observer locations. From the numerical simulations, it was found that low-frequency amplitude-modulated sounds can be heard even at long distances from a wind turbine; these sounds would be the thumping sound reported in the previous researches. Several calculation cases were also simulated to find the relative effect on the generation of the amplitude modulation of wind turbine noise. It was concluded that

convective amplification is found to be the main cause of the thumping sound rather than trailing edge noise directivity, strong wind shear, or turbulence ingestion.

Furthermore, to reduce the wind turbine aerodynamic noise, an optimization method was proposed to modify the airfoil shape and the blade planform of a 10kW wind turbine. From the verification of the optimized blade design with wind tunnel experiments, it was confirmed that the trailing edge noise from the wind turbine blades were reduced by up to 2.6dB due to the design optimization. In addition, wind turbine blades with serrated trailing edge were also examined for the noise reduction. A field experiment was carried out based on a 10kW wind turbine. The experimental results indicated that the overall sound pressure level was reduced by 1~3dB due to the serrated trailing edge. In conclusion, these methods will be useful for reducing the wind turbine aerodynamic noise.

References

- [1] S. Wagner, R. Bareiß, and G. Guidati, *Wind Turbine Noise*, Springer-Verlag, Berlin, 1996.
- [2] T. Brooks, D. Pope, and M. Marcolini, *Airfoil self-noise and prediction*, NASA Reference Publication 1218, NASA, 1989.
- [3] K. S. Brentner and F. Farassat, Modeling aerodynamically generated sound of helicopter rotors, *Progress in Aerospace Sciences* 39 (2003) 83-120.
- [4] J. E. Ffowcs Williams and D. L. Hawkings, Sound generation by turbulence and surfaces in arbitrary motion, *Philosophical Transactions of the Royal Society of London. Series A, Mathematical and Physical Sciences* 264 (1969) 321-342.
- [5] K. S. Brentner and F. Farassat, Analytical Comparison of the Acoustic Analogy and Kirchhoff Formulation for Moving Surfaces, *AIAA Journal* 36(8) (1998) 1379- 1386.
- [6] W. J. Zhu, N. Heilskov, W. Z. Shen, and J. N. Sørensen, Modeling of aerodynamically generated noise from wind turbines, *Journal of Solar Energy Engineering* 127 (2005) 517-528.
- [7] G.P. van den Berg, Effects of the wind profile at night on wind turbine sound, *Journal of Sound and Vibration* 277 (2004) 955–970.
- [8] G.P. van den Berg, The beat is getting stronger: the effect of atmospheric stability on low frequency modulated sound of wind turbines, *Journal of Low Frequency Noise, Vibration, and Active Control* 24 (2005) 1-24.

- [9] C. Di Napoli, Wind turbine noise assessment in a small and quiet community in Finland, *Noise Control Engineering Journal* 59(1) (2011) 30-37.
- [10] C. Larsson and O. Öhlund, Amplitude modulation of sound from wind turbines under various meteorological conditions, *The Journal of the Acoustical Society of America* 135(1) (2014) 67-73.
- [11] M. S. Howe, Aerodynamic noise of a serrated trailing edge, *Journal of Fluids and Structures* 5 (1991) 33-45.
- [12] M. S. Howe, Noise produced by a sawtooth trailing edge, *The Journal of the Acoustical Society of America* 90(1) (1991) 482-487.
- [13] Th. Lutz, A. Herrig, W. Würz, M. Kamruzzaman, and E. Krämer, Design and Wind-Tunnel Verification of Low-Noise Airfoils for Wind Turbines, AIAA 2006-3322, AIAA, 24th Applied Aerodynamics Conference, June 5-8, 2006, San Francisco, California, USA.
- [14] F. Bertagnolio, H. Aa. Madsen, and C. Bak, Trailing Edge Noise Model Validation and Application to Airfoil Optimization, *Journal of Solar Energy Engineering* 132 (2010) 031010.
- [15] M. Herr and W. Dobrzynski, Experimental Investigations in Low-Noise Trailing-Edge Design, *AIAA Journal* 43(6) (2005) 1167-1175.
- [16] S. Oerlemans, M. Fisher, T. Maeder, and K. Kögler, Reduction of Wind Turbine Noise Using Optimized Airfoils and Trailing-Edge Serrations, *AIAA Journal*, 47(6) (2009) 1470-1481.
- [17] B. Petitjean, R. Drobietz, and K. Kinzie, Wind turbine blade noise mitigation technologies, *Proceedings of WTN 2011*, April 12-14, 2011, Rome, Italy.

- [18] S. Lee, S. Lee, J. Ryi, and J-S Choi, Design optimization of wind turbine blades for reduction of airfoil self-noise, *Journal of Mechanical Science and Technology* 27(2) (2013) 413-420.
- [19] S. Lee and S. Lee, Serrated trailing edge blade design for reduction of wind turbine aerodynamic noise, *Journal of Wind Energy* 4(1) (2013) 53-59.
- [20] R. K. Amiet, Noise due to turbulent flow past a trailing edge, *Journal of Sound and Vibration* 47 (1976) 387-393.
- [21] R. K. Amiet, Effect of the incident surface pressure field on noise due to turbulent flow past a trailing edge, *Journal of Sound and Vibration* 57 (1978) 305-306.
- [22] Y. Rozenberg, G. Robert, and S. Moreau, Wall-Pressure Spectral Model Including the Adverse Pressure Gradient Effects, *AIAA Journal* 50(10) (2012) 2168-2179.
- [23] S. Lee and S. Lee, Numerical and experimental study of aerodynamic noise by a small wind turbine, *Renewable Energy* 65 (2014) 108-112.
- [24] S. Lee, S. Lee, and S. Lee, Numerical modeling of wind turbine aerodynamic noise in the time domain, *The Journal of the Acoustical Society of America* 133(2) (2013) EL94-EL100.
- [25] H. H. Hubbard, F. W. Grosveld, and K. P. Shepherd, Noise Characteristics of Large Wind Turbine Generators, *Noise Control Engineering Journal* 21(1) (1983) 21-29.
- [26] L. A. Viterna, The NASA LaRC Wind Turbine Sound Prediction Code, NASA CP 2185 (1981).
- [27] F. W. Grosveld, Prediction of Broadband Noise from Horizontal Axis Wind Turbines, *Journal of Propulsion and Power* 1(4) (1985) 292-299.

- [28] R. H. Schlinker and R. K. Amiet, Helicopter rotor trailing edge noise, NASA Contractor Report 3470, NASA, 1981.
- [29] M. V. Lowson, Theory and experiment for wind turbine noise. AIAA Paper 94-0119, AIAA, 32nd Aerospace sciences meeting and exhibit, January 10-13, 1994, Reno, Nevada, USA.
- [30] R. K. Amiet, Acoustic radiation from an airfoil in a turbulent stream, *Journal of Sound and Vibration* 41(4) (1975) 407-420.
- [31] <http://web.mit.edu/drela/Public/web/xfoil/> (Accessed 1 June 2014)
- [32] S. Oerlemans and J. G. Schepers, Prediction of wind turbine noise and validation against experiment, *International Journal of Aeroacoustics* 8 (2009) 555-584.
- [33] P. J. Moriarty, G. Guidati, and P. Migliore, Prediction of Turbulent Inflow and Trailing-Edge Noise for Wind Turbines, AIAA 2005-2881, AIAA, 11th AIAA/CEAS Aeroacoustics Conference, May 23-25, 2005, Monterey, California, USA.
- [34] S. Wagner, G. Guidati, J. Ostertag, Numerical simulation of the aerodynamics and aeroacoustics of horizontal axis wind turbines, *Proceedings of the ECCOMAS 98 conference*, 1998.
- [35] P. J. Moriarty, G. Guidati, P. Migliore, Recent Improvement of a Semi-Empirical Aeroacoustic Prediction Code for Wind Turbines, AIAA 2004-3041, AIAA, 10th AIAA/CEAS Aeroacoustics Conference, 2004, Manchester, UK.
- [36] O. Fleig, M. Iida, and C. Arakawa, Wind Turbine Blade Tip Flow and Noise Prediction by Large-eddy Simulation, *Journal of Solar Energy Engineering* 126 (2004) 1017-1024.

- [37] Q. Zhou and P. F. Joseph, Frequency-domain method for rotor self-noise prediction, *AIAA Journal* 44 (2006) 1197-1206.
- [38] V. P. Blandeau and P. F. Joseph, Validity of Amiet's Model for Propeller Trailing-Edge Noise, *AIAA Journal* 49(5) (2011) 1057-1066.
- [39] H. H. Hubbard, *Aeroacoustics of Flight Vehicles: Theory and Practice Volume 1: Noise Sources*, NASA Reference Publication 1258, Vol. 1, 1991
- [40] Y. Rozenberg, M. Roger, and S. Moreau, Rotating blade trailing-edge noise: Experimental validation of analytical model, *AIAA Journal* 48 (2010) 951-962.
- [41] D. M. Chase, Sound radiated by turbulent flow off a rigid half-plane as obtained from a wavevector spectrum of hydrodynamic pressure, *The Journal of the Acoustical Society of America* 52 (1972) 1011-1023.
- [42] K. L. Chandiramani, Diffraction of evanescent waves, with applications to aerodynamically scattered sound and radiation from un baffled plates, *The Journal of the Acoustical Society of America* 55 (1974) 19-29.
- [43] M. S. Howe, Trailing edge noise at low Mach numbers, *Journal of Sound and Vibration* 225 (1999) 211-238.
- [44] Y. N. Kim and A. R. George, Trailing-edge noise from hovering rotors, *AIAA Journal* 20 (1982) 1167-1174.
- [45] N. Curle, The Influence of Solid Boundaries upon Aerodynamic Sound, *Proceedings of the Royal Society of London. Series A, Mathematical and Physical Sciences*, 231(1187) (1955) 505-514.
- [46] G. M. Corcos, The structure of the turbulent pressure field in boundary-layer flows, *Journal of Fluid Mechanics* 18(3) (1964) 353-378.

- [47] M. S. Howe, *Acoustics of fluid-structure interactions*, Cambridge University Press, New York, 1998.
- [48] J. Counihan, Adiabatic atmospheric boundary layer: a reviewed and analysis of data from the period 1880-1972, *Atmospheric Environment* 9(10) (1975) 871-905.
- [49] M. Goody, Empirical Spectral Model of Surface Pressure Fluctuations, *AIAA Journal* 42(9) (2004) 1788-1794.
- [50] F. H. Clauser, Turbulent Boundary Layers in Adverse Pressure Gradients, *Journal of the Aeronautical Sciences* 21(2) (1954) 91-108.
- [51] F. R. Menter, Two-Equation Eddy-Viscosity Turbulence Models for Engineering Applications, *AIAA Journal* 32(8) (1994) 1598-1605.
- [52] N. Gregory and C. L. O'Reilly, *Low-Speed Aerodynamic Characteristics of NACA 0012 Aerofoil Section, including the Effects of Upper-Surface Roughness Simulating Hoar Frost*, R&M No. 3726, Ministry of Defence, 1970.
- [53] C. L. Ladson, A. S. Hill, and W. G. Johnson, Jr., Pressure distributions from high Reynolds number transonic tests of an NACA 0012 airfoil in the Langley 0.3-meter transonic cryogenic tunnel, *NASA Technical Memorandum 100526*, NASA, 1987.
- [54] J. V. Backer, *Boundary-Layer Transition on the N.A.C.A. 0012 and 23012 Airfoils in the 8-Foot High-Speed Wind Tunnel*, NACA Report, 1940.
- [55] T. F. Brooks and T. H. Hodgson, Trailing edge noise prediction from measured surface pressures, *Journal of Sound and Vibration* 78(1) (1981) 69-117.
- [56] International Electrotechnical Commission IEC 61400-11, *Wind turbine generator systems—Part 11: Acoustic noise measurement techniques*, 2002.

- [57] H. Kim, Nonlinear bound vortex correction method for unsteady aerodynamic loading and noise analysis of wind turbine rotor, Ph.D. dissertation, Seoul National University (2011).
- [58] E. Pedersen and K. Persson Waye, Perception and annoyance due to wind turbine noise—A dose-response relationship, *The Journal of the Acoustical Society of America* 116 (2004) 3460-3470.
- [59] C. Kantarelis and J. G. Walker, The identification and subjective effect of amplitude modulation in diesel engine exhaust noise, *Journal of Sound and Vibration* 120(2) (1988) 297-302.
- [60] J. S. Bradley, Annoyance caused by constant-amplitude and amplitude-modulated sounds containing rumble, *Noise Control Engineering Journal* 42(6) (1994) 203-208.
- [61] S. Lee, K. Kim, W. Choi, and S. Lee, Annoyance caused by amplitude modulation of wind turbine noise, *Noise Control Engineering Journal* 59 (2011) 38-46.
- [62] P. Dunbabin, An investigation of blade swish from wind turbines, *Proceedings of Internoise 96*, Liverpool, August 1996, 463-469.
- [63] S. Oerlemans, P. Sijtsma, and B. Méndez López, Location and quantification of noise sources on a wind turbine, *Journal of Sound and Vibration* 299 (2007) 869-883.
- [64] A. Laratro, M. Arjomandi, R. Kelso, and B. Cazzolato, A discussion of wind turbine interaction and stall contributions to wind farm noise, *Journal of Wind Engineering and Industrial Aerodynamics* 127 (2014) 1-10.
- [65] S. A. L. Glegg, S. M. Baxter, and A. G. Glendinning, The prediction of broadband noise from wind turbines, *Journal of Sound and Vibration* 118 (1987) 217-239.

- [66] F. Farassat and G. P. Succi, A review of propeller discrete frequency noise prediction technology with emphasis on two current methods for time domain calculations, *Journal of Sound and Vibration* 71 (1980) 399-419.
- [67] K. S. Brentner, Prediction of helicopter rotor discrete frequency noise—A computer program incorporating realistic blade motions and advanced acoustic formulation, NASA Technical Memorandum 87721, NASA, 1986.
- [68] R. W. Paterson and R. K. Amiet, Noise and Surface Pressure Response of an Airfoil to Incident Turbulence, *Journal of Aircraft* 14(8) (1977) 729-736.
- [69] J. Casper and F. Farassat, Broadband trailing edge noise predictions in the time domain, *Journal of Sound and Vibration* 271 (2004) 159-176.
- [70] J. Boersma, Computation of Fresnel integrals, *Mathematics of Computation* 14 (1960) 380.
- [71] R. K. Amiet, High frequency thin-airfoil theory for subsonic flow, *AIAA Journal*, 14(8) (1976) 1076-1082.
- [72] M. T. Landahl, *Unsteady transonic flow*, Cambridge University Press, New York, 1989.
- [73] J. Casper and F. Farassat, A new time domain formulation for broadband noise predictions, *International Journal of Aeroacoustics*, 1 (2002) 207–240.
- [74] J. J. Adamczyk, Passage of a Swept Airfoil through an Oblique Gust, *Journal of Aircraft* 11(5) (1974) 281-287.
- [75] M. S. Howe, Edge-source acoustic Green's function for an airfoil of arbitrary chord, with application to trailing-edge noise, *The Quarterly Journal of Mechanics and Applied Mathematics*, 54 (2001) 139-155.

- [76] R. K. Amiet, Correction of open jet wind tunnel measurements for shear layer refraction, AIAA Paper 75-532, AIAA 2nd Aero-Acoustics Conference, March 24-26, 1975, Hampton, Virginia, USA.
- [77] International Organization for Standardization ISO 9613-1, Acoustics—Attenuation of sound during propagation outdoors—Part 1: Calculation of the absorption of sound by the atmosphere, 1993.
- [78] Y. Seong, S. Lee, D-Y Gwak, Y. Cho, J. Hong, and S. Lee, An experimental study on annoyance scale for assessment of wind turbine noise, *Journal of Renewable and Sustainable Energy* 5 (2013) 052008.
- [79] H. H. Hubbard and K. P. Shepherd, Aeroacoustics of large wind turbines, *The Journal of the Acoustical Society of America* 89(6) (1991) 2495-2508.
- [80] H. Fastl and E Zwicker, *Psychoacoustics: Facts and Models*, Springer, Berlin, 2007.
- [81] R. M. Hicks and P. A. Henne, Wing design by numerical optimization, *Journal of Aircraft*, 15 (7) (1978) 407-412.
- [82] R. Tanese, Distributed genetic algorithms, *Proc. of the 3rd International Conference on Genetic Algorithms*, Fairfax, Virginia, USA (1989) 434-439.
- [83] S. Watanabe, T. Hiroyasu and M. Miki, Neighborhood cultivation genetic algorithm for multi-objective optimization problems, *Proc. of the Genetic and Evolutionary Computation Conference*, New York, NY, USA (2002) 458-465.

풍력터빈에서 발생하는 광대역 소음의 생성과 전파 및 저감에 대한 연구

서울대학교 대학원
기계항공공학부
이승훈

국문초록

본 연구는 풍력터빈에서 발생하는 공기역학적 광대역 소음에 대하여 조사한다. 해석적인 뒷전 소음 모델과 역압력 구배 유동에 적합한 벽-압력 스펙트럼 모델을 사용하여 풍력터빈 공력소음을 예측하는 수치기법을 제안한다. 블레이드 단면에서의 벽 압력 스펙트럼들을 구하기 위하여 Reynolds-averaged Navier-Stokes 시뮬레이션과 XFOIL 소프트웨어를 사용한다. 본 기법은 빠르고 신뢰성이 있는 기법이므로 산업계에서 활용하기 적합한 기법이다. 수치기법의 검증을 위하여 10kW 풍력터빈을 대상으로 소음 측정이 이루어졌으며, 이를 바탕으로 측정 데이터와 예측 결과를 비교한다. 최종적으로, 제안된 기법을 이용하여 3MW 풍력터빈에서 발생하는 공력소음을 다양한 풍속과 위치에서 예측한다.

또한, 본 연구에서는 수음자 위치에 따른 풍력터빈 소음의 음향학적인 특성을 비교하고 풍력터빈 소음의 진폭변조의 주 원인을 조사하기 위하여 풍력터빈 소음을

시간 영역에서 모델링 한다. 블레이드 표면의 비정상 압력을 결정하기 위하여 해석적인 뒷전 소음 모델과 난류 유입 소음 모델을 사용하고, 비정상 압력에 의하여 생성되는 원방 음압은 음향상사법을 이용하여 계산한다. 2차원 형상에 대한 소음 모델은 스트립 이론을 이용하여 회전하는 풍력터빈 블레이드에 적용한다. 수치해석 결과 풍력터빈의 운영조건과 대기조건이 동일하다 하더라도 풍력터빈으로부터 떨어진 수음자의 거리와 방향에 따라서 풍력터빈 소음의 음향학적인 특성은 매우 다를 수 있다는 것을 확인한다. 본 예측 결과를 바탕으로, 풍력터빈 소음의 진폭변조가 풍력터빈으로부터 멀리 떨어진 지역에서도 들리는 이유를 분석한다.

마지막으로, 10kW 풍력터빈을 대상으로 뒷전소음을 저감시키기 위하여 유전 알고리즘을 기반으로한 최적화 기법을 이용하여 풍력터빈 블레이드의 익형 단면과 플랜폼을 수정한다. 먼저 로터 블레이드의 한 단면에 대한 최적화된 블레이드 형상을 설계하고, 설계된 최적 익형을 바탕으로 최적 블레이드를 설계한다. 설계된 최적 형상을 검증하기 위하여 풍동 시험도 수행하였다. 추가로 톱니형 뒷전을 가진 풍력터빈 블레이드가 소음 저감에 미치는 영향도 조사한다. 이를 위하여 10kW 풍력터빈을 대상으로 현장 시험을 수행한다.

주요어: 풍력터빈 소음, 광대역 소음, 소음 저감, 뒷전 소음, 난류 유입 소음,

설계 최적화, 소음 측정

학번: 2009-30903